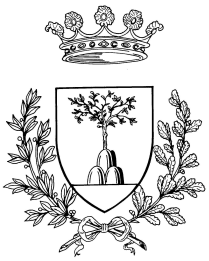

University of Ferrara

Physics and Earth Science Department

Master Degree in Physics

Development of a synchrotron radiation beam monitor for the Integrable Optics Test Accelerator

SUPERVISOR

Prof. Eleonora LUPPI

STUDENT

Andrea SCARPELLI

CO-SUPERVISOR

Prof. Giulio STANCARI

Year 2015-2016

Acknowledgements

I am deeply indebted to supervisor Eleonora Luppi and to my co-supervisors Giulio Stancari, who gave me the unique opportunity to spend the summer at Fermilab working on the research project described in this thesis and who deeply revised my work methodically scrubbing all the errors away and giving me precious advices.

A special thank to all the IOTA group, in particular to A. Romanov, A. Valishev, J. Ruan, C. Edstrom, J. Santucci, K. Carlson, D. Crawford, M. McGee and all the other scientists or technicians who always found out the time for addressing my dull questions.

Sincere thanks to all those who help me to make it in the "New World" and in particular to my American flatmates, who gave me the chance to spend a great summer full of smart conversations and good food.

I also thank the "Italian Corner", Ilaria, Lucia and Francesco, who shared with me the fluster of writing a thesis and whose intolerance to my pointless concerns gave me the strength to not give up.

I am grateful to my special friend, Ale, who daily supported me and who I felt close to me even if I was 10,000 km far away.

My deepest gratitude is still reserved to my old and my new family, who many times encouraged me flying far from home: my successes and my happiness are not only mine, but also theirs.

Sommario

L'ottica non lineare applicata alla dinamica degli acceleratori potrebbe mitigare le instabilità dovute alle forze interne tra particelle, ma esperimenti di questo tipo non sono mai stati condotti. L'Integrabile Optics Test Accelerator (IOTA) è un anello di accumulazione per elettroni e protoni in costruzione a Fermilab, sviluppato per testare l'effetto di elementi non lineari sulla dinamica delle particelle; in aggiunta saranno condotti anche esperimenti sul raffreddamento stocastico nella banda ottica (*optical stochastic cooling*) e sulla funzione d'onda del singolo elettrone. Tali esperimenti richiedono un preciso controllo sui parametri del fascio, raggiungibile grazie a precisi e veloci sistemi di misura. Questa tesi descrive alcune delle fasi per la realizzazione di un rivelatore per IOTA basato sulla radiazione di sincrotrone e in grado di misurare intensità, posizione e sezione d'urto del fascio. Lo studio del processo di formazione delle immagini all'interno del rivelatore è stato condotto mediante una simulazione Monte Carlo. Gli effetti della diffrazione e della profondità di campo sono stati calcolati per alcuni valori tipici della sezione d'urto e danno un contributo del 20%. È stato realizzato e testato un prototipo realistico, avente una lente da 400 mm e una magnificazione di 0.837. La risoluzione del prototipo è stata misurata per diverse aperture e lunghezze d'onda. Per implementare sul dispositivo un sistema automatico di controllo dell'immagine sono stati inclusi su uno specchio e sul sensore video alcuni posizionatori a circuito aperto, controllabili a distanza. Due algoritmi, uno per la centratura automatica dell'immagine e il secondo per la messa a fuoco, sono stati implementati.

Abstract

Nonlinear integrable optics applied to beam dynamics may mitigate multi-particle instabilities, but proof-of-principle experiments have never been carried out. The Integrable Optics Test Accelerator (IOTA) is an electron and proton storage ring currently being built at Fermilab, which addresses tests of nonlinear lattice elements in a real machine in addition to experiments on optical stochastic cooling and on the single-electron wave function. These experiments require an outstanding control over the lattice parameters, achievable with fast and precise beam monitoring systems. This work describes the steps for designing and building a beam monitor for IOTA based on synchrotron radiation, able to measure intensity, position and transverse cross-section of a beam. A study of the imaging formation in the monitor has been done using a Monte Carlo simulation. Diffraction and depth of field are calculated for some reference values of the beam cross-section, showing a 20% contribution at the optimal aperture. A realistic layout of the monitor has been proposed and a table-top prototype, with a 400-mm focal lens and magnification of 0.837, has been built. The image formation in the prototype is investigated and the resolution measured for different apertures and wavelengths. In view of automatic image adjustment systems, the prototype includes remotely controlled open-loop positioners to move a mirror and a camera sensor. Algorithms for automatic image centring and focusing have been proposed and implemented.

Table of contents

List of figures

List of tables

Introduction

This thesis focuses on the development of beam monitors for accelerator science and for particle physics. The experimental work was conducted during a ten-week internship at Fermilab in the summer of 2016, supported by the program on Physics of Accelerators and Related Technology for International students (PARTI).

After the Particle Physics Project Priorisation Panel (P5) in 2014 and the guidelines of the High Energy Physics Advisory Panel (HEPAP) [1], Fermilab has developed a twenty year research program that emphasises neutrinos and rare processes, including the LBNF/DUNE, g-2 and mu2e experiments [2] [3] [4]. Fundamental for their success are high quality multi-MW proton beams, which cannot be provided in the current state-of-art accelerators. A remarkable part of Fermilab research activities is oriented toward an upgrade of the existing facilities (Figure 1) and the design of new cost-effective multi MW proton beams.

The Proton Improvement Plan-II (PIP-II) [5] is one of the solutions proposed for addressing the demand of high intensities. It is a proton superconducting radio frequency (SFR) linac currently underway, which has been developed to provide 1.2 MW of proton beam power at the start of operations of the LBNF/DUNE experiment. SRF is a promising technology for beam quality and flexibility. Research on it is very active and mostly oriented toward costs reduction.

In parallel, the required beam intensities in the typically less expensive synchrotron rings could be achieved reducing particle losses due to collective and incoherent beam instabilities. Experimental study of novel techniques for instabilities control are now one of the highest priorities at the FAST/IOTA[1] facility [6] [7] [8].

The Fermilab Accelerator Science and Technology (FAST) facility was formed as a research centre for beam physics and for the development of new technologies for the next generation of particle accelerators. Currently FAST includes a SRF linac coupled with a photoinjector and a small storage ring for proton and electrons, IOTA, currently under construction (Figure 2).

[1] formerly ASTA/IOTA

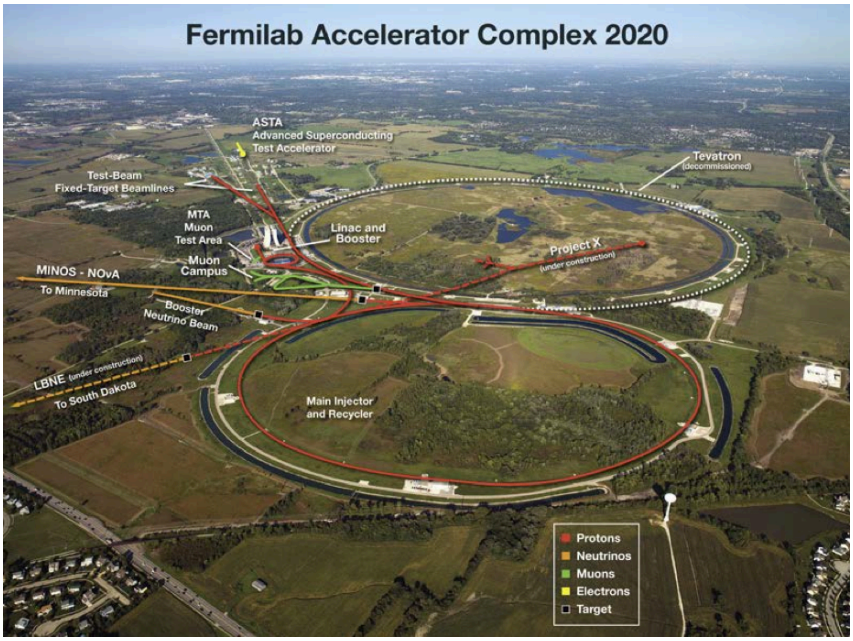

Fig. 1 The Fermilab accelerator complex by the end of this decade. [6].

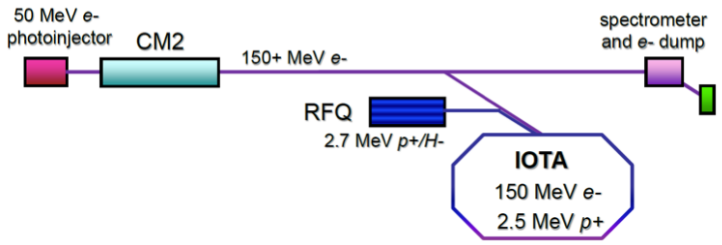

Fig. 2 Layout of the FAST/IOTA facility . [8].

The Integrable Optics Test Accelerator (IOTA) purposes involve the study of nonlinear systems, of beams with strong space charge, and of optical stochastic cooling. The controlled interplay between nonlinear focusing forces and self fields may have a significant impact on the achievable beam intensities, which are currently limited by instabilities and by losses. In view of the outstanding precision control over the beam parameters demanded by IOTA , it is necessary put several efforts in designing opportune beam monitors and beam diagnosis tools. Among many solutions, a monitor based on synchrotron radiation is a non destructive, fast, and cost effective technique for measuring the intensity, position and transverse cross section of the beam.

This thesis describes the development of a beam monitor for IOTA based on synchrotron radiation. First of all it is important take a glimpse on the main IOTA experiments, acknowledging their specificities and their requirements. A description of the classical beam

dynamics and of the new principle under test in IOTA is made in Chapter 1. Then, a formal introduction on synchrotron radiation is given in Chapter 2, with a particular focus on the description of its angular distribution. Chapter 3 is devoted to the analysis of imaging formation in the peculiar case of a synchrotron radiation source. The two main sources of systematic uncertainties, diffraction and depth of field effect, are extensively studied in the case of IOTA with realistic numerical simulations. The experiments, the design of IOTA and the features of the radiation poses some constraints for the design of the beam monitor. The choices made are in Chapter 4 as well as the development of a tabletop prototype based on a realistic layout. This prototype is tested using a LED as light source for proving the image formation model outlined in Chapter 3 and for finding out more possible systematics effects caused, for instance, by some lens aberrations. The flexibility of the IOTA ring impose an high versatility for the beam monitor, hence an image centring and an autofocusing system are designed and tested. For the latter, new upgrading solutions are also investigated. All these results are discussed in Chapter 5.

Chapter 1

Beam dynamics in IOTA

In this chapter, we introduce the principles of nonlinear integrable beam dynamics and the ring, IOTA, specifically designed for testing it. In particular, we focus on the instrumental resolution required for measuring some key parameters, such as position, intensity and cross section of the beam.

Section 1.1 gives an overview on the mathematical formalism of the linear accelerators dynamics, developed in 1958 by E.D. Courant and H. S. Snyder in 1958 [9] and highlights the many instabilities, which may drive the particles motion far from the linear regime. In the second section, we describe the role of nonlinear integrable dynamics in mitigating these instabilities and we work out solutions for the nonlinear equation of motion which yield a realistic design of a nonlinear accelerator. Section 1.3 introduces the experiments proposed on IOTA for testing nonlinear insertions on a real machine, and describes the setup and and the most relevant features of the beam diagnosis instruments.

1.1 Linear transverse dynamics

1.1.1 Definitions

In order to understand the motivation for the non linear experiments, an overview on the beam linear transverse dynamics is here given. An electron storage ring consists of a lattice of deflecting bending magnets (dipoles) and focusing quadrupole magnets as well as a radio frequency (RF) cavity for accelerating the beam. The dipoles determine a closed equilibrium orbit, called reference orbit, for a particle having the nominal values of energy, initial position and angle. The motion of a charged particle moving through the accelerator is defined in a coordinate system centred on the reference trajectory. The coordinate s is the arc length measured along the trajectory and the coordinates x, y, s make up a right-handed coordinate

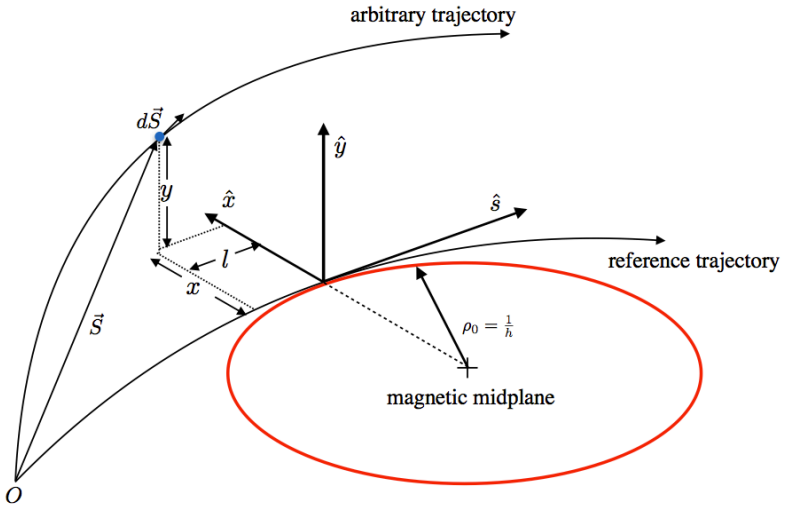

Fig. 1.1 An arbitrary particle trajectory shown in relation to the reference trajectory. [10]

system. It is common in accelerator physics to define the particle's phase space using the geometrical coordinates $\boldsymbol{X}$ as in [10]:

$$\boldsymbol{X}(s) = \begin{pmatrix} x \\ x' \\ y \\ y' \\ l \\ \delta \end{pmatrix},$$

where x, y, l are the horizontal, vertical and longitudinal displacement from the reference trajectory (Figure 1.1); $\delta = \Delta p/p$ is the relative momentum deviation from the nominal momentum. The primed coordinates $x' = dx/ds$ and $y' = dy/ds$ are the angles (horizontal and vertical) with respect to the reference trajectory. We assume very small deviations from the nominal values of radius ρ and energy E and we use the paraxial approximation with

$$\frac{x}{\rho} \ll 1, \quad x' \ll 1, \quad \frac{y}{\rho} \ll 1, \quad y' \ll 1, \quad \frac{\Delta E}{E} \ll 1.$$

The main effect of dipoles and quadrupoles is a force that is proportional to the displacement from the reference orbit. Therefore, the effect on the beam of any linear (dipole or quadrupole) lattice magnet may be expressed with a 6x6 transport matrix. The relation between the coordinates up and downstream of a given lattice element (or a set of elements)

is

$$\boldsymbol{X}(s) = \boldsymbol{R}\boldsymbol{X}(0),$$

where $\boldsymbol{R}$ is the product of all the transport matrices between 0 and s.

1.1.2 Betatron oscillations

The quadrupole magnets in a lattice deflect particles with a deviation in position back towards the reference trajectory, with a force proportional to the particle displacement. Quadrupoles are able to focus only in one direction; along the second direction the beam is defocused (the particles see the deflecting force in opposite directions to the reference trajectory). By convention, horizontally focusing and defocusing quadrupoles are respectively called "F-quads" and "D-quads". A lattice with a single quadrupole cannot keep a beam stable, hence a periodic structure is needed. The simplest periodic lattice is called FODO and it is made up of a focusing quad, a drifting section, a defocusing quad and a second drifting section. The FODO scheme is repeated for many revolutions and this causes transverse oscillations about the reference trajectory called betatron oscillation. In general, the equation describing the motion of a charged particle in a linear accelerator is an homogeneous differential equation known as Hill's Equation [10] [11]:

$$x''(s) + K_x^2(s)x(s) = 0, \quad \text{with } K_x^2(s) = \left[\frac{1}{\rho^2} + \frac{e}{p}\frac{\partial \boldsymbol{B}_x(s)}{\partial y}\right], \tag{1.1}$$

where $\boldsymbol{B}_x$ is the horizontal component of the quadrupole magnetic field, e and p are respectively the charge and the momentum of the particle, and ρ is the bending radius of the dipoles. In the following, we are using the horizontal coordinates, but they may be replaced with the vertical ones. The Hill's equation may be interpreted as an harmonic oscillator with a restoring force which depends on the position along the accelerator.

Hill's equation has been extensively studied in mathematics. The solution has the form [10]:

$$x(s) = \sqrt{\boldsymbol{J}_x \beta_x(s)}\cos\mu_x, \tag{1.2a}$$

$$x'(s) = -\sqrt{\frac{\boldsymbol{J}_x}{\beta_x(s)}}[\sin\mu_x + \alpha(s)\cos\mu_x]. \tag{1.2b}$$

$\boldsymbol{J}_x$ is an invariant of motion (also called single-particle emittance), $\beta_x(s)$ is called beta function and describes how the amplitude of the particle oscillation varies through the beam trajectory, while $\mu_x(s)$ is the phase function, describing the change of phase along s. Along

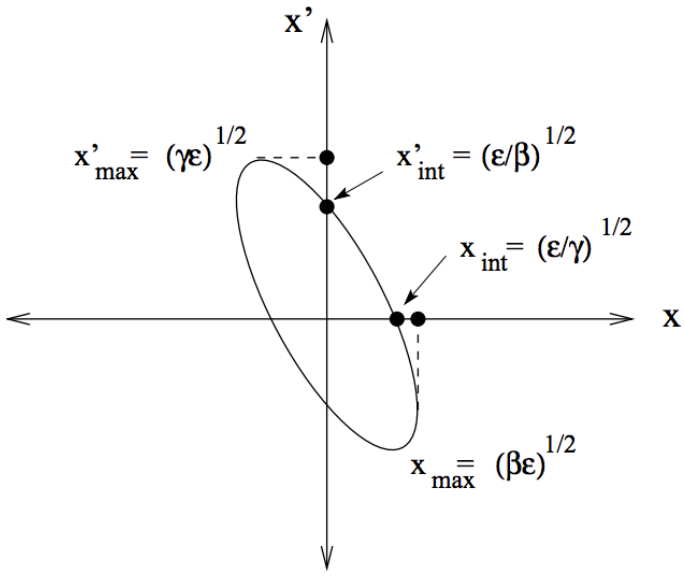

Fig. 1.2 The phase space ellipse for a single particle at a given position in the storage ring. In the figure ϵ indicates the invariant of motion J_x.

a given arc $[s_1; s_2]$ the beta and the phase functions are related as follows:

$$\mu_x(s) = \int_{s_1}^{s_2} \frac{ds}{\beta_x(s)}. \tag{1.3}$$

Equations 1.2 can be combined to yield:

$$J_x = \gamma_x(s)x(s)^2 + 2\alpha_x(s)x(s)x'(s) + \beta_x(s)x'^2(s), \tag{1.4}$$

where α and β are defined as:

$$\alpha_x(s) = -\frac{1}{2}\beta'_x(s) \quad \text{and} \quad \gamma_x(s) = \frac{1+\alpha_x^2(s)}{\beta_x(s)}.$$

α, β, γ are called Twiss (or Courant-Snyder) parameters and they depends only on the magnetic structure of the machine. Equation 1.4 describes an ellipse in the plane (x, x') (Figure 1.2). The shape and the orientation of the ellipse depends on the Twiss parameters and its changes along the machine, but the area πJ_x remains a constant.

So far we limited ourselves to the dynamics of a single particle. However, a beam is composed of many particles with different phases and amplitudes, describing ellipses with different areas, but with the same orientation and aspect ratio at any given location. Therefore, the beam as a whole covers a phase space distribution $\Psi(x, x')$ of the same form of

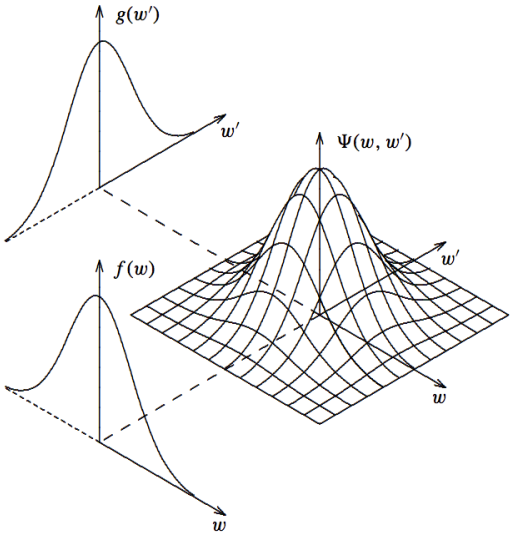

Fig. 1.3 The phase space distribution and its projection upon the two directions of a beam. w and w' correspond to x and x'. [12]

the single particle ellipse, but obviously with a different area $\pi\epsilon_x$. ϵ_x is often called beam emittance and it is defined as the average of the invariant of motion for each particle:

$$\epsilon_x = \langle J_x \rangle.$$

An example of phase space distribution is shown in Figure 1.3. It cannot be observed directly, but we can measure the its projection $f(x)$ and $g(x')$ on the plane of position or angle,

$$f(x) = \int \Psi(x, x')dx', \quad g(x') = \int \Psi(x, x')dx.$$

The average position and angles are then

$$\langle x \rangle = \frac{\int x f(x)dx}{\int f(x)dx} \quad \text{and} \quad \langle x' \rangle = \frac{\int x' g(x')dx'}{\int g(x')dx'},$$

while the variance in position and angle are:

$$\langle x^2 \rangle = \frac{\int x^2 f(x)dx}{\int f(x)dx} \quad \text{and} \quad \langle x'^2 \rangle = \frac{\int x'^2 g(x')dx'}{\int g(x')dx'}.$$

The rms (root mean square) size of both position and angle may be defined as usual:

$$\sigma_x = \sqrt{\langle x^2 \rangle} \quad \text{and} \quad \sigma_{x'} = \sqrt{\langle x'^2 \rangle}.$$

For a beam, equation 1.4 is modified into:

$$\epsilon_x = \gamma_x(s)\sigma_x^2 + 2\alpha_x(s)\langle x(s)\rangle\langle x'(s)\rangle + \beta_x(s)\sigma_{x'}^2, \tag{1.5}$$

and from this one can find two important relations between the Twiss parameters and the rms size of the distribution:

$$\sigma_x(s) = \sqrt{\epsilon_x \beta_x(s)} \tag{1.6a}$$

$$\sigma_{x'}(s) = \sqrt{\epsilon_x \gamma_x(s)} \tag{1.6b}$$

In a storage ring, dispersion in the beam is generated in each dipole. This happens because each particle deviates from the design momentum, hence it is bended differently. The dispersion function $D_x(s)$ describes the horizontal deviation acquired by the particle due to its momentum offset. In presence of dispersion, equations 1.6 are extended, according to [10], as:

$$\sigma_x(s) = \sqrt{\epsilon_x \beta_x(s) + (D_x(s)\delta)^2} \tag{1.7a}$$

$$\sigma_{x'}(s) = \sqrt{\epsilon_x \gamma_x(s) + (D'_x(s)\delta)^2} \tag{1.7b}$$

For off-momentum particles, the ellipse is no longer centred in the origin of the phase space, but it gains an offset in both direction given by $D_x(s)\delta$ and $D'_x(s)\delta$.

Beam emittance will not change unless the beam is acted upon a non conservative force. This is a consequence of the Liouiville's theorem, which states the conservation of the phase space density along any trajectory in the phase space for Hamiltonian systems. Figure 1.4 is a well representation of the above concept: the beta function changes through the magnetic lattice and so does the shape of the beam ellipse, but the area remains constant. The emittance cannot be reduces without using cooling systems [1]. There are also many undesirable causes of emittance dilution, such as phase-space mismatch during injection and extraction of the beam, intrabeam scattering, etc.

[1] The name cooling came in analogy to the definition of temperature in a gas. Cooling means increasing the phase space density of the beam. Cooling systems are external forces removing energy from the beam and reducing its dispersion of position and angle. The most common cooling techniques are electron cooling and stochastic cooling [13]. As we will see later, also synchrotron radiation provides a natural cooling to particle beams.

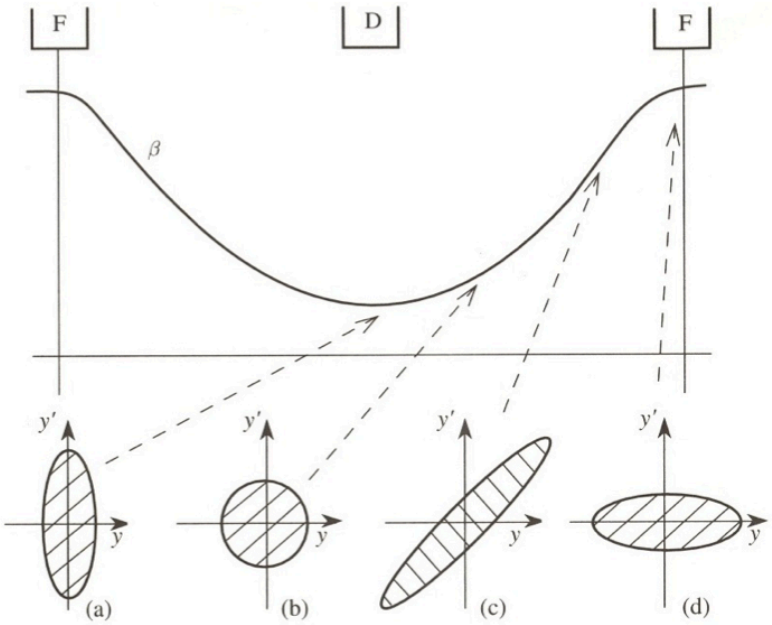

Fig. 1.4 Vertical phase space transformation through a FODO lattice. Emittance is constant, while the shape of the phase space distribution changes in shape and orientation.[11]

1.1.3 Machine working point (tune) and imperfections

Equation 1.3 defines the phase advance for a machine section. The phase advance on the whole circumference is called tune, ν and it is defined in [11] as the number of oscillation in a circumference:

$$\nu_x = \frac{1}{2\pi} \oint \frac{ds}{\beta_x(s)}. \tag{1.8}$$

Tune is one of the most important beam parameter, because certain tune values cause unbounded oscillations in the beam. If a particle has an integer tune, this means it has the same transverse position every time it passes in a given point. Any perturbation from an ideal field at that location will push the particle the same way on every pass, leading to an uncontrolled growth from the closed orbit and to particle losses. Same way an half integer tune allows resonant driving forces on the beam triggered by the quadrupoles field error, third-integer tune cause sextupole resonances, and so on. Operational tune values of an accelerator must be chosen in order to avoid resonances. This mean avoiding tune values $\nu = k/n$, where k is an integer and n is the order of the resonance. The strength of the resonances depends on the magnetic imperfections of the ring. Considering both planes, resonances occurs when the sum of both tunes is an integer: $a\nu_x + b\nu_y = P$, where a, b and

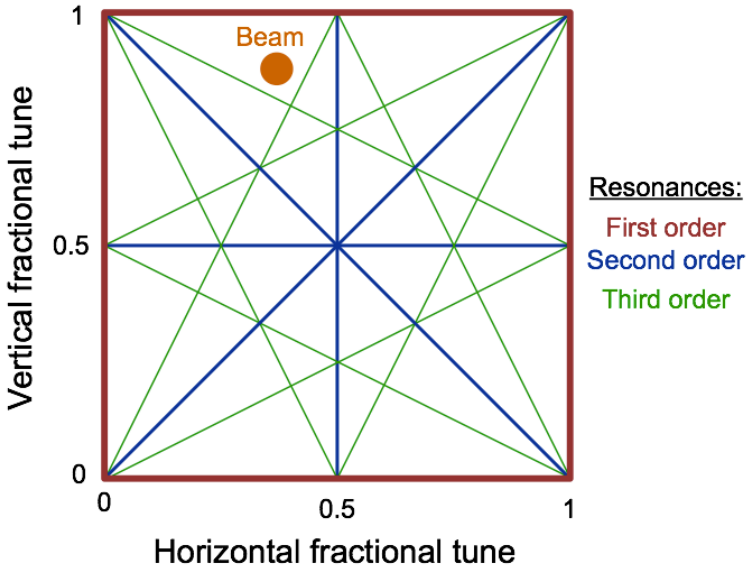

Fig. 1.5 Example of a tune diagram. Solid lines are examples of resonance lines . The orange dot represent the machine working point. [11]

P are integers and $a + b$ is the order of the resonance. A diagram such as Figure 1.5 helps the physicists to choose a proper operational tune that does not cross the the resonant lines.

In a beam composed of many particles there is a non negligible momentum dispersion, therefore each particle has a different magnetic rigidity and it is bended on a different orbit by the dipoles, generating a position dispersion. This effect is called chromaticity.

Because of chromatic and nonlinear effects, all the particles in a beam have different tune values, so the orange area on the diagram in Figure 1.5 is more a distribution instead of a dot. Tune spread is one of the most thorny parameters of an accelerator and it is the main limit to high luminosity machines.

In addition to tuning resonances, in a lattice there are more sources of instabilities. A beam is made up of millions of charged particles, exerting mutual defocusing force due to their Coulomb repulsion. This is called space-charges force and its responsible for many distortions on the beam dynamics such as energy exchanges and shifts of the betatron frequencies. In the same way also beam-beam interactions produce dynamical instabilities.

Lattice instabilities such as tuning resonances and space-charge forces hinder the large dynamical aperture required in high intensity accelerators. The dynamical aperture identifies the area of the phase space where the motion is stable. Any stable motion in the phase space is described by closed trajectories, hence the dynamical aperture is as large as the largest possible closed trajectory. For a perfect linear machines, the phase space contains

only stable orbits, therefore the dynamical aperture is limited by the diameter of the beam pipe. However, the presence of non linearities causes an uncontrolled growth of the particle oscillations amplitude and the trajectories in the phase space are distorted to open curves. The dynamical aperture is then reduced to the area within the largest closed trajectory, which is smaller than the dynamical aperture of the linear case.

1.2 Nonlinear dynamics

1.2.1 Sources and consequences of nonlinear elements in standard lattices

Mainstream lattices are designed to be linear, that means the amplitude of the oscillations depends on the fist power of the transverse position. Dipoles and quadrupoles are linear lattice elements. This linearity ideally links a particle in an accelerator to an harmonic oscillation. However, space-charge as well as imperfections in magnetic fields are nonlinear effects and they make up intrinsic sources of instabilities, which yields resonances. Motion becomes unstable at large amplitudes and this reduces the dynamical aperture of the beam.

Despite that, nonlinear effects, in addition to a large tune spread can also have advantages: they can mitigate collective effects in space-charge dominated beams and improve the stability against periodic perturbations. Some non linear elements are already used in conventional lattices for correcting chromaticity (sextupoles) and for generating tune spread and enhancing Landau damping[2] (octupoles). However, we must stress on the fact that these nonlinear insertions do not drive the particle on a stable motion, but they simply compensate the instabilities and the particle losses yielded by space-charge effects, imperfections, etc...

1.2.2 Nonlinear integrable dynamics

The particle motion generated by the nonlinearities we met so far (sextupoles, octupoles, space-charge forces, etc...) is said non-integrable, because it is not stable over many revolutions around the machine. Let us now introduce a new class of nonlinear motions, which are called integrable. According to Liouville-Arnold theorem, a system is integrable, when it has as many constants of motions as degree of freedom. If a motion is integrable, then it is bounded and stable. This general definition of integrability may be exploited for for designing a nonlinear lattice. A nonlinear integrable lattice does not simply compensate for

[2]Landau damping is a stabilisation effect on the centroid of a set of driven oscillators with a wide range of oscillation frequencies.

the instabilities, but it drives the particles on closed trajectories in the phase space as an ideal linear lattice does.

The first attempts of a nonlinear integrable lattice came in the late '60s with the pioneering work of E. McMillan [14]. He found out a one-dimensional solution in the case of thin lens kick in the form of a rational polynomial, combined with a lattice with given phase advance. Recently, Danilov and Nagaitsev succeed in extending the studies of McMillan to a transverse motion with two invariants and proposed a solution which can be implemented with special nonlinear lenses [15]. Two concepts exists for nonlinear lenses. The first is a static nonlinear magnetic field, while the second is based upon an electron lens generating a non linear kick with an electron distribution of given shape.

A nonlinear integrable solution using a special magnet is widely discussed in a paper by Danilov and Nagaitsev [15]. The study of nonlinear solutions is often approached adding perturbative potential to the Hamiltonian of the stable system and discussing integrability. For a practical realisation using magnetic fields, the potential must be also solution of the Laplace equation. A non linear time dependent potential V is added to the Hamiltonian for a regular linear lattice:

$$H(x, y, p_x, p_y, s) = \frac{p_x^2 + p_y^2}{2} + \frac{K_x(s)x^2 + K_y(s)y^2}{2} + V(x, y, s), \tag{1.9}$$

where x, y are the transverse position, p_x and p_y the transverse momenta and $K_x(s)$ and $K_y(s)$ are the focusing gradients of the quadrupoles from equation 1.1. The time dependence of the Hamiltonian is contained within the parameter s. In condition of an axially symmetric lattice ($K_x(s) = K_y(s)$), the Hamiltonian becomes:

$$H(x, y, p_x, p_y, s) = \frac{p_x^2 + p_y^2}{2} + K(s)\left(\frac{x^2 + y^2}{2}\right) + V(x, y, s). \tag{1.10}$$

A normalisation using the beta function allows moving all the time dependance on the potential. Ref. [15] shows a solution using elliptical coordinates, leading to an exactly integrable system, which is also solution for the Laplace equation. Danilov and Nagaitsev identified a possible implementation of such a lattice. It consists of two parts:

- a drift space with equal horizontal and vertical beta function;
- an arc (so called T-insert), with overall focusing strength k in each plane, containing quadrupoles and dipoles which has the transfer matrix as a thin axially symmetric lens.

The nonlinear elements are accommodate in the drifting space.

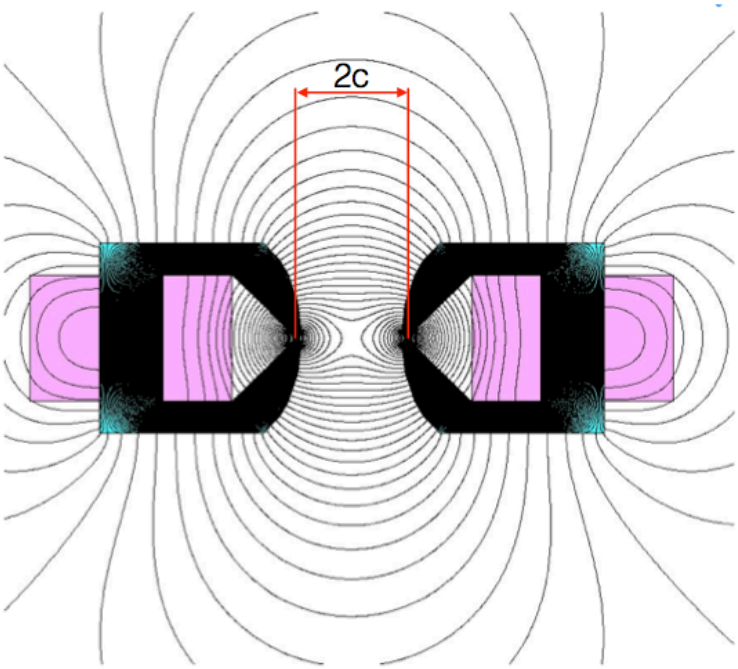

Fig. 1.6 Field lines for the non linear magnet. [17]

A nonlinear magnet may be shaped for providing a potential V according to Danilov and Nagaitsev solutions in Section 1.2.2 and its field lines are displayed in Figure 1.6. The potential is defined by two parameters: the strength t and the geometric parameter c, which represents the element aperture. The former must vary as $1/\beta$ and the latter as $\sqrt{\beta}$. Since it is not practical to manufacture a magnet with complex varying aperture, it is possible to approximate the continuously varying potential with a number of thin magnets of constant aperture. Demonstration of stable nonlinear motion with large tune spread requires the largest possible strength parameter t and vertical oscillation amplitudes larger than c. Numerical simulations [16] tested the motion stability and showed that c must be comparable to the expected beam size in the middle of the non linear section for a significant tune spread.

An electron lens employs the electromagnetic field generated by a magnetised low-energy electron beam interacting with an higher-energy particle beam over an extended length L [18]. The electron beam is produced in an electron gun solenoid by a thermionic cathode and then guided into the main machine, where it overlaps with the circulating beam. It is then extracted by a collector. The lenses can be used for linear and nonlinear forces depending on the electron current distribution $j(r)$, the electron beam radius a and the rms size σ of the circulating beam at the overlap region. The profile $j(r)$ can be controlled by shaping the cathode and the extraction electrodes.

The study of the integrability of this type of kicks was first performed by McMillan. Assuming a radial current distribution $j(r) = j_o a^4/(r^2 + a^2)^2$ is emitted by the electron gun with velocity β_e, while traversing the electron lens a beam with velocity β_z and magnetic rigidity ($B\rho$) will experience a kick [19]:

$$\theta(r) = 2\pi \frac{j_0 L(1 \pm \beta_e \beta_z)}{(B\rho)\beta_e \beta_z c^2} \frac{a^2 r}{r^2 + a^2} \left(\frac{1}{4\pi\epsilon_0} \right). \tag{1.11}$$

If the element is thin ($L \ll \beta$) and the phase advance is an odd multiple of $\pi/2$, for this kick there are two independent variables of motion in the transverse phase space.

1.3 The IOTA ring

1.3.1 Purpose and planned experiments

The nonlinear dynamics principles outlined above have been widely tested with simulations and now require proof-of-principle experiments. The main goal of the IOTA experiments is to demonstrate the possibility to implement nonlinear integrable systems in a realistic accelerator design. Among all, the most relevant experiments for this thesis include: tests of nonlinear magnets and electron lenses, test of the optical stochastic cooling (OSC) method and experiments for exploring the nature of the quantum wave function of a single electron.

The goal or the nonlinear integrable optics experiments is to achieve a large tune spread, of the order of 0.25 or more, while preserving the dynamic aperture and lifetime of the circulating beam. Experimentally, this will be observed recording the lifetime and turn by turn position of a low intensity and low emittance electron bunch, injected and kicked for different betatron amplitudes for different settings of the non linear elements. The tune spread and the dynamic range will be calculated by measuring the position and the intensity of the beam with the beam position monitors. Synchrotron-light monitors will add more informations on the beam transverse cross section and they will complete the previous measures.

Stochastic cooling was first developed by S. Van Der Meer in 1972 and is extensively explained in [13]. It is used for reducing the position dispersion of a distribution in phase space, by correcting the position of a sample of particle turn after turn. The position of the sample is measured by a pick up and the information is sent to a correction kicker. The number of particles in each sample is determined by the frequency bandwidth, which should be maximised because it sets the maximum possible cooling rate. The OSC [20] is a new cooling technique which might extend the present day limit of 8 GHz up to hundreds of THz. The idea behind the OSC experiment is very similar to the regular stochastic cooling,

except that it uses optical frequencies and undulators instead of electromagnetic pickups and kickers. For this kind of experiments it is important measuring the cooling rate through the beam transverse dimension changes with respect to the elapsed time.

Experiments for exploring the nature of the quantum wave function of a single electron have been proposed for IOTA [21] [22] [23]. The first is based on the observation of the time distribution of photons emitted by a single stored electron. The second arises from a puzzling behaviour of electrons in superfluid helium bubbles. Under certain condition an electron appear to be simultaneously trapped within two bubbles, and the only explanation put forward is in terms of "fractional electrons", called electrinos. Results obtained with super helium are firmly established [24]. Independent studies without helium are being considered. These experiments require the detection of the lowest beam intensities, which can be achieved with synchrotron-light monitors in counting mode.

1.3.2 Layout and beam parameters

The IOTA ring will be capable to operate with 50-150 MeV electrons or with 2.5 MeV protons. Its flexible lattice allows to accommodate multiple experiments with the same physical setup. The electron beam will be injected into IOTA from the superconducting RF test facility [6], while a proton injector is currently being studied. The electron injector determines the momentum spread, while the total circumference was determined by the dimensions of the experimental hall. Figure 1.7 displays the complete layout of the IOTA ring. Non linear experiments are responsible for the main constrains: in particular they requires a large diameter to fit large amplitude oscillations of the test beam and at least 2 meters long straight section to accommodate the non linear components. The lattice is designed to fulfil the axial symmetry condition required as solution for the non linear systems. OSC experiment only requires two 5 m long straight section and a two-fold mirror lattice symmetry. More elements present in the lattice are:

- 8 C-shaped dipoles, 4 of 30 degrees and 4 of 60 degrees, with a bending radius of 0.7 m and a bending magnetic field of 0.7 T;
- 39 water-cooled quadrupole with 71 mm bore and 0.2 m magnetic length;
- dual frequency RF cavity which can provide 1 kV at 30 MHz for electrons;
- 21 button-type electrostatic pick-up beam position monitors;
- 8 synchrotron radiation beam monitors, which are the subject of the thesis.

More lattice parameters are sorted in Table 1.1.

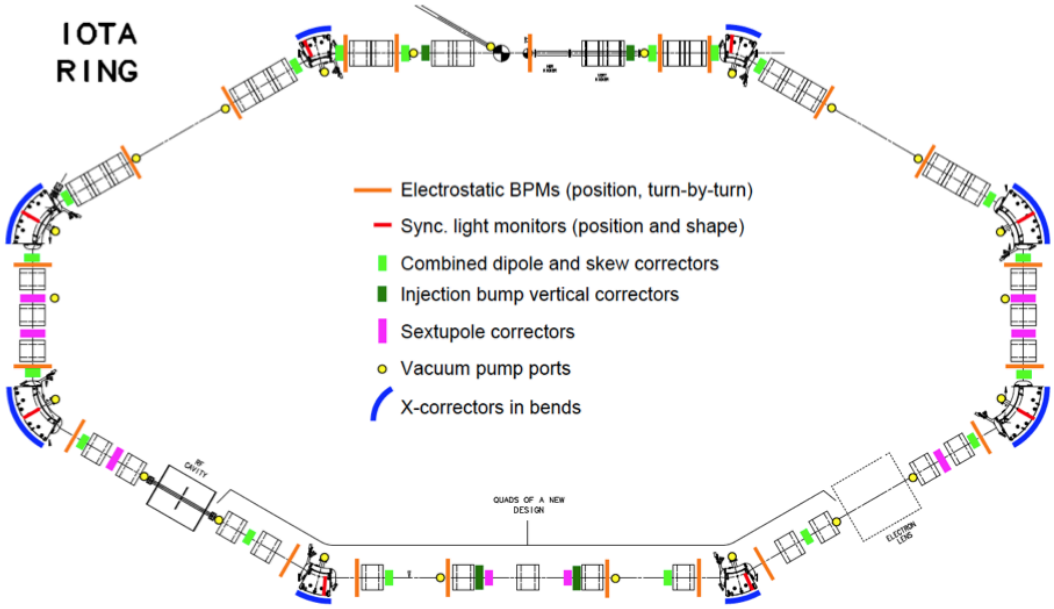

Fig. 1.7 Layout of IOTA storage ring [8].

Table 1.1 IOTA main lattice design parameters.

Parameter	Value
Circumference	40 m
Dipole bending radius	0.7 m
Dipole nominal magnetic field	0.7 T
Beam pipe diameter	50 mm
e max. nominal energy	150 MeV
Nominal e beam max. intensity	1×10^9
Transverse rms equilibrium emittance	0.1 μm
Max. beta function x, y	12, 5 m
Nominal bunch length	2 cm
Nominal momentum spread	1.4×10^{-4}
Typical beam size at bending magnet	≥ 70 μm

1.3.3 Diagnostics for machine commissioning

Machine setup for non linear experiments requires a precision lower than 1% for the beta function and around 0.001 for the betatron phase advance [10]. For this reasons, an outstanding quality of the dipole and quadrupole fields is required as well as a precise correction of the closed orbits. Detailed simulations have been carried out for studying how errors and imperfections in the lattice may influence the outcome of the experiments [25]. Beam position measurement systems must meet the desired precision. On IOTA, two different set of devices will be used: electrostatic pickups and synchrotron radiation beam monitors.

Electrostatic pickups are a noninvasive technique for measuring the beam position. The idea is to measure the charge induced by the electromagnetic field of the particle on an insulated metal plate. In general four pick-up plates are installed crosswise at the beam pipe wall and the difference signals of opposite plates yield the beam centre of mass for both transverse planes. In IOTA, resolution on the beam position must be 1 μm for the closed orbit correction and 100 μm for turn by turn measurements.

Informations on the transverse profile of the beam will come in a nondestructive way from synchrotron radiation beam monitors. IOTA will mount 8 of these monitors, one for each dipole. Synchrotron light will be extracted by a special window, mounted tangentially to the beam trajectory in the vacuum chamber. These monitors will provide a measure of the beam cross section in 8 different position along the ring. The transverse size is related to the lattice parameters through equation 1.7a. Emittance is naturally limited on electron rings by radiation damping (see Section 2.4) and the values of β and D in each position may be worked out by simulations of the beta function and the dispersion function along the beam such as in in Figure 1.8. In the 8 positions of the beam monitors, the expected beam cross section will range from 50 μm to 650 μm for nonlinear experiments and from 20 μm to 150 μm for the OSC experiment. Resolution must be smaller than the expected beam size. Optical diffraction, depth of field and aberrations are the main limits to a good resolution. The investigation of these effects is one of the main issues of this thesis and it is widely detailed in the next chapters.

Synchrotron-light monitors will be very useful for the preliminary correction of the lattice parameters during the earlier stages of the IOTA commissioning, and for continuous monitoring during the non linear experiments. In addition, they may provide a sensible estimation of the low number of electrons circulating in the ring for the electron experiment.

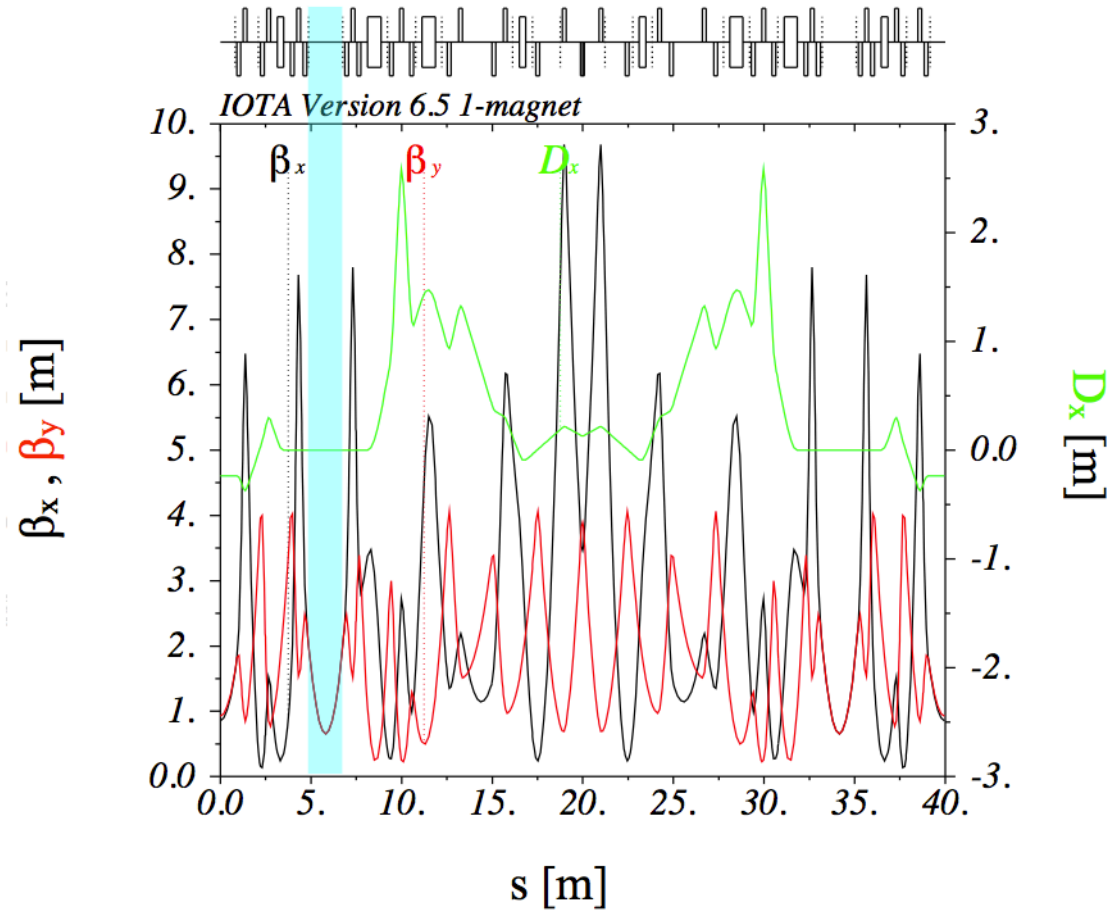

Fig. 1.8 Transverse beta function and dispersion function along the IOTA lattice for nonlinear magnet experiment.

Chapter 2

Properties of synchrotron radiation

The radiation emitted by a relativistic particle moving on a circular orbit is called synchrotron radiation. The need for a description of this phenomenon arose only in recent times, after the commissioning of the first powerful betatrons in 1944. Ivanenko and Pomeranchuk were the first to point out some limitations to the maximum energy in a betatron due to the emission of electromagnetic radiation [26]. In 1947, Frank Elder and others observed for the first time a visible radiation in the 70 MeV synchrotron at General Electric [27]. Since then, this radiation is known as synchrotron radiation. Schwinger made the first detailed description of this phenomenon in 1949 [28].

This radiation is the main limit to the maximal energy of the electron/positron synchrotrons and storage rings, because as the particle energy is driven higher and higher, more and more rf-power must be spent not only to accelerate, but also to overcome the energy losses due to synchrotron radiation.

Despite this issues, synchrotron radiation has interesting properties and it is widely used for many applications. First of all it is a bright and high collimated source of light. The frequency spectrum is wide and a large part of the total power is radiated in the X-ray region. Synchrotron light has major application in various disciplines such as condensed matter physics, material science, biology and medicine. Almost 70 facilities around the world are devoted in producing synchrotron light [29].

Synchrotron radiation is a nondestructive method for measuring some important beam properties such as the transverse sizes as well as the bunch length[1] [30]. For this, it is a standard beam diagnostics technique currently used on many electron rings and in some

[1] While the measure of the transverse size is easily done using TV cameras, CCDs, CMOS or other similar technologies, the measurement of short bunch lengths requires more sophisticated technologies such as fast oscilloscopes, PMTs, or streak cameras with picoseconds time resolution.

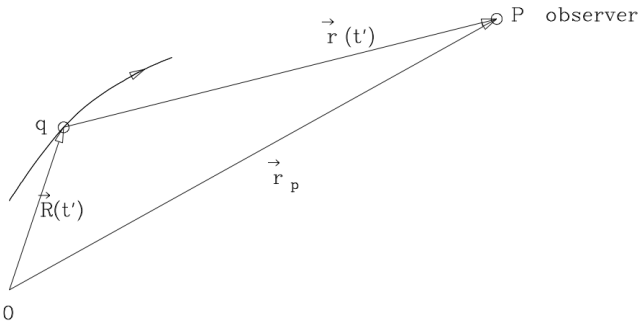

Fig. 2.1 Moving charge geometry [12]

high energy proton rings. The Fermilab Tevatron collider was equipped with such a device [31] and also the Large Hadron Collider has its synchrotron radiation diagnosis tool [32].

This chapter is a brief treatment of synchrotron radiation properties and its effects in an electron ring. In the first section the mathematical treatment will be described, which leads to an estimation of the fields and the power emitted by an accelerated particle on a circular trajectory. Then the peculiar characteristics of synchrotron radiation will be discussed, in particular the polarisation modes for the electric field, the power and the photons distribution. Formal treatment of this subject can be found in many accelerator physics books such as [33], [34], in some specialised manuals [12] and in the proceedings of specialised schools [35] [36].

2.1 Power radiated from an accelerated charge

2.1.1 Electric and magnetic fields of a moving charge

Power radiated by a moving charge can be found using a classical treatment and this subject is matter of many articles and textbooks; this section is based on the approach outlined in [37] and [12].

The finite light speed causes a delay between the time a particle emits a field and the time a given observer, P, receives this field. If a charge q is moving on the trajectory $\boldsymbol{R}(t')$ and at time t' it emits a radiation, this is later seen in P at the moment t (Figure 2.1). These two instants are related by:

$$t = t' + \frac{|\boldsymbol{r}(t')|}{c}.$$

If we consider two very short time intervals, the time interval between two emissions is related to the time interval between two observations by the important following relation:

$$dt = (1 - \boldsymbol{n} \cdot \boldsymbol{\beta})dt', \tag{2.1}$$

where $\boldsymbol{n}$ is the direction of the observer and β the speed of the charge divided by the speed of light. The validity of equation 2.1 can be checked assuming a particle heading towards the observer and emitting a signal at two different times. For an observer in the laboratory reference frame the time elapsed between the two signal is shorter than the time in the particle reference frame. In fact, after the first signal was emitted, the charge moves closer to the observer, thus the second signal takes less time from the emission point to the observer.

Keeping in mind the foregoing discussion, the solutions of the Maxwell's equations in vacuum and the Lorentz gauge can be found in the form of scalar and vector potentials evaluated at the emission time [37]:

$$\phi(\boldsymbol{r}, t) = \frac{1}{4\pi\epsilon_0} \int \int \frac{\rho(\boldsymbol{r}', t')}{|\boldsymbol{r}(t')|} \delta \left(t' + \frac{|\boldsymbol{r}(t')|}{c} - t \right) \, d^3r' \, dt',$$

$$\boldsymbol{A}(\boldsymbol{r}, t) = \frac{\mu_0}{4\pi} \int \int \frac{\boldsymbol{J}(\boldsymbol{r}', t')}{|\boldsymbol{r}(t')|} \delta \left(t' + \frac{|\boldsymbol{r}(t')|}{c} - t \right) \, d^3r' \, dt',$$

where the delta function provides the retarded behaviour.

Finding the magnetic and the electric fields from ϕ and $\boldsymbol{A}$ requires the evaluation of the previous integrals and the use of the definition of the potentials:

$$\boldsymbol{E} = -\frac{\partial \boldsymbol{A}}{\partial t} - \nabla\phi,$$

$$\boldsymbol{B} = \nabla \times \boldsymbol{A}.$$

This process is not straight forward and it will be not reported here, but the detailed solution for it can be found in [37]. The electric and magnetic fields are:

$$\boldsymbol{E}(\boldsymbol{r}, t) = \frac{q}{4\pi\epsilon_0} \left(\frac{(1 - \beta^2)(\boldsymbol{n} - \boldsymbol{\beta})}{r^2(1 - \boldsymbol{n} \cdot \boldsymbol{\beta})} + \frac{\boldsymbol{n} \times [(\boldsymbol{n} - \boldsymbol{\beta}) \times \dot{\boldsymbol{\beta}}]}{cr(1 - \boldsymbol{n} \cdot \boldsymbol{\beta})^3} \right), \tag{2.2a}$$

$$\boldsymbol{B}(\boldsymbol{r}, t) = \frac{1}{c} (\boldsymbol{n} \times \boldsymbol{E}). \tag{2.2b}$$

Equation (2.2a) has two terms: a velocity field, which is independent of the acceleration, and an acceleration field, which depends linearly on $\dot{\boldsymbol{\beta}}$. In the reference frame of the particle, the

velocity field reduces to the well-known Coulomb field. It is basically a static field and it scales as r^{-2} and so it does not contribute to the radiation, whereas the acceleration field is typically a radiation field and it falls off as r^{-1}.

From now on the velocity field will be neglected for simplicity. This convenient approximation is used in [12]. However, it is important to note that the acceleration field alone is not a solution of Maxwell's equations.

2.1.2 The classical Larmor formula and relativistic corrections

The power emitted is given by the flux of the Pointing vector ($\boldsymbol{S}$) through a spherical surface:

$$P = \int \boldsymbol{S}(\boldsymbol{r}, t') \cdot \boldsymbol{n}\, r^2 d\Omega; \tag{2.3}$$

$\boldsymbol{S}$ can be expressed in terms of the electric field [12]:

$$\boldsymbol{S}(\boldsymbol{r}, t') = \epsilon_0 c |\boldsymbol{E}(\boldsymbol{r}, t)|^2 \boldsymbol{n}. \tag{2.4}$$

Equation 2.3 represents the energy flowing through the surface per unit of t, which is different to the actual power emitted by the charge at t'. This because the two time interval are not equal, as we described before. Substituting equations 2.2a and 2.4 into equation 2.3, one obtains angular dependence of the emitted power:

$$\frac{dP}{d\Omega} = \left(\frac{q}{4\pi\epsilon_0 c}\right)^2 \epsilon_0 c \, \frac{\{\boldsymbol{n} \times [(\boldsymbol{n} - \boldsymbol{\beta}) \times \dot{\boldsymbol{\beta}}]\}^2}{(1 - \boldsymbol{n} \cdot \boldsymbol{\beta})^5}. \tag{2.5}$$

In the particle reference frame, with Θ as the angle between the acceleration and the observation point, equation 2.5 can be written:

$$\frac{dP}{d\Omega} = \left(\epsilon_0 c \frac{q}{4\pi\epsilon_0 c}\right)^2 \dot{\boldsymbol{\beta}}^2 \, \sin^2\Theta,$$

and integrating over the solid angle the total instantaneous power is then obtained the well-known Larmor's formula:

$$P = \frac{2}{3}\frac{e^2}{4\pi\epsilon_0 c^3}\left(\frac{d\boldsymbol{v}}{dt}\right)^2 = \frac{2}{3}\frac{e^2}{m^2 c^3}\left(\frac{d\boldsymbol{p}}{dt}\right)^2. \tag{2.6}$$

Equation 2.6 is the exact radiation pattern of the radiation in the particle reference frame. We may also consider this pattern as the radiation patter of a non-relativistic particle like that from a linear antenna.

As was pointed out by Schwinger [28], Larmor formula can be generalised by arguments about covariance under Lorentz transformations to yield a result which is valid for arbitrary velocities of the charge. Radiated energy and time transform in the same way under Lorentz transformation, whereas the radiated power must be an invariant. The general formula is a Lorentz invariant which reduces to equation 2.6 in the limit of $\beta \to 0$. The generalisation can be found from this observation:

$$\frac{dp_\mu}{d\tau}\frac{dp^\mu}{d\tau} = \left(\frac{d\boldsymbol{p}}{d\tau}\right)^2 - \frac{1}{c^2}\left(\frac{dE}{d\tau}\right)^2 = \left(\frac{d\boldsymbol{p}}{d\tau}\right)^2 - \beta^2\left(\frac{dp}{d\tau}\right)^2,$$

where $d\tau = dt/\gamma$ is the proper time. The general case of the Larmor formula is then:

$$P = \frac{2}{3}\frac{e^2}{4\pi\epsilon_0 m^2 c^3}\left[\left(\frac{d\boldsymbol{p}}{d\tau}\right)^2 - \beta^2\left(\frac{dp}{d\tau}\right)^2\right],$$

which can be better expressed in terms of β and $\dot{\boldsymbol{\beta}}$ substituting $E = \gamma mc^2$ and $\boldsymbol{p} = \gamma m\boldsymbol{v}$:

$$P = \frac{2}{3}\frac{e^2}{4\pi\epsilon_0 c}\gamma^6\left[(\dot{\boldsymbol{\beta}})^2 - (\boldsymbol{\beta}\times\dot{\boldsymbol{\beta}})^2\right] \tag{2.7}$$

The two limiting cases of equation 2.7 are realised in linear and in in the circular acceleration. In the former, the the second term of equation 2.7 vanishes, thus:

$$P = \frac{2}{3}\frac{e^2}{4\pi\epsilon_0 c}\gamma^6\left(\frac{dv}{dt}\right)^2 = \frac{2}{3}\frac{e^2}{4\pi\epsilon_0 m^2 c^3}\gamma^6\left(\frac{dE}{dx}\right)^2.$$

In this case the radiation emitted will be negligible, unless the gain in energy is of the order of $\approx 10^{14}$ MeV/m. Linear accelerators have usually a gain in energy of few tens of MeV per meters, thus the radiation losses are completely negligible.

In the second case equation 2.7 becomes,

$$P_0 = \frac{2}{3}\frac{e^2}{4\pi\epsilon_0 m^2 c^3}\gamma^2\left(\frac{dp}{dt}\right)^2, \tag{2.8}$$

this formula can be rewritten in a more convenient way as function of β, γ and the bending radius ρ:

$$P_0 = \frac{2r_e mc^3\beta^4\gamma^4}{3\rho^2}, \tag{2.9}$$

where r_e (in the case the particle beam is made of electron) is the classical electron radius. For a given energy, the dependence on m^{-4} through the Lorentz factor makes the power radi-

ated highly significative in the case of light particle such as electrons or positrons. Equation 2.9 can be expressed in more practical units as follows:

$$P_0(\text{GeV/s}) = \frac{cC_\gamma}{2\pi}\frac{E^4}{\rho^2},$$

with C_γ is a constant defined (in the case of electrons or positrons) as [33]:

$$C_\gamma = \frac{4\pi}{3}\frac{r_e}{(mc^2)^3} = 8.8575 \times 10^{-5}\ \text{m GeV}^{-3}.$$

The energy loss in one turn can be evaluated multiplying equation 2.9 by the revolution period $T = 2\pi\rho/c$:

$$U = \frac{4\pi r_e mc^2 \gamma^4}{3\rho}, \tag{2.10}$$

The foregoing equations are also valid in the case of discontinuous bending dipoles. In this case, the real energy losses per turn are found from the actual revolution period of the machine.

2.2 Synchrotron radiation

The radiation emitted by a particle moving on a circumference with radius ρ is called synchrotron radiation. As is pointed out in [12], some approximations are made in treating this subject. First, the radiation is assumed to be emitted by a long magnet with constant magnetic field. Second, the radiation is observed at a relatively large distance from the source. Third, the particle is assumed to be relativistic. All these approximation are satisfied for most of synchrotron radiation sources. Correction from quantum effects can be neglected as long as the energy of the emitted photons is lower than the energy of the charged particles; this happens for energies around 10^6 GeV [34].

2.2.1 Spectral properties

We can give an intuitive estimation of the synchrotron radiation frequency spectrum considering the duration of the pulse. As one can see in Figure 2.2, the radiation received in a particular direction corresponds only to a small arc of the particle trajectory of length $2\rho\gamma^{-1}$. The time duration of the pulse is the time difference between the time the electron takes to

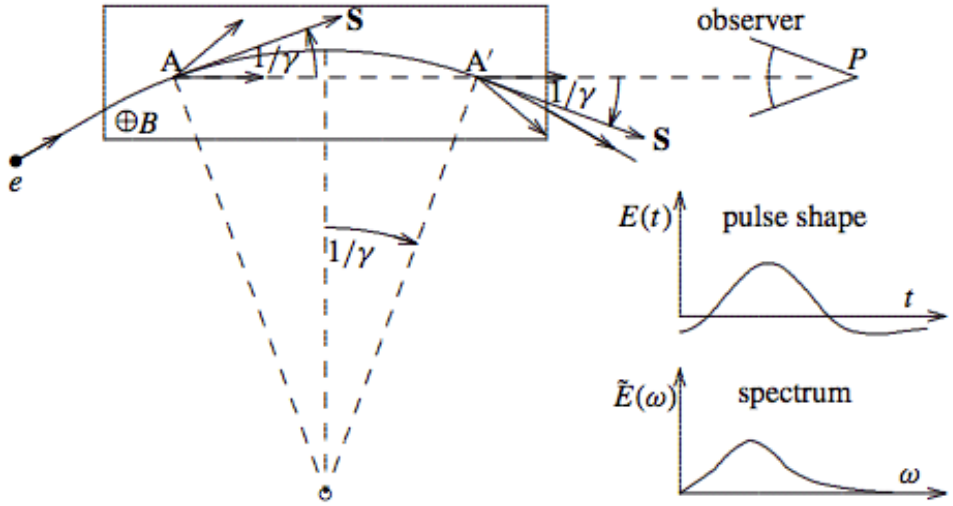

Fig. 2.2 Arc trajectory contribution to the frequency spectrum. [12].

travel around the arc t_e and the time the photon takes to travel straight from A to A', t_γ. So:

$$\Delta t = t_e - t_\gamma = \frac{2\rho}{\gamma\beta c} - \frac{2\sin\frac{1}{\gamma}}{c}, \quad \text{for } \gamma \gg 1 \;\; \Delta t \approx \frac{4\rho}{3\gamma^3 c}$$

The short time interval implies a large wide band of frequencies; the critical frequency characterise the upper end of the spectrum and is defined as

$$\omega_c = \Delta t^{-1} \approx \frac{3\gamma^3 c}{4\rho}.$$

In terms of revolution frequency $\omega_{rev} \approx \rho c^{-1}$ we have $\omega_c/\omega_{rev} \approx \gamma^3$; thus, the frequency spectrum extends at very much higher frequencies than the revolution frequency.

2.2.2 Electric field in the frequency domain

Because of the short time pulse, the emitted frequency spectrum is wide. In a classical approach this spectrum is continuous. It was shown [12] that for relativistic velocities the spectrum from a single electron pass does not differ from that originated by a periodic motion. It is more convenient to express the electric field in the frequency domain. The Fourier transform of the electric field is:

$$E(\omega) = \int_{-\infty}^{\infty} \boldsymbol{E}(t)\, e^{-i\omega t} dt.$$

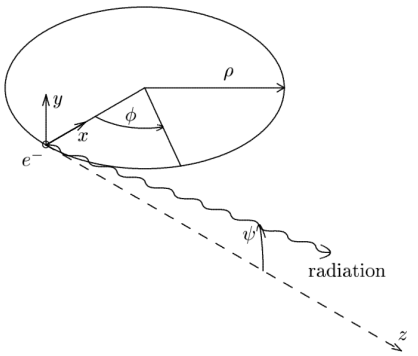

Fig. 2.3 Geometry used to describe the synchrotron radiation angular distribution. [35].

It can be expressed as function of the emission time t':

$$E(\omega) = \int_{-\infty}^{\infty} \boldsymbol{E}(t)\, e^{-i\omega(t'+r(t')/c)}(1 - \boldsymbol{n}\cdot\boldsymbol{\beta})dt'.$$

By substituting (2.2a) and integrating by parts, one finds:

$$E(\omega) = \frac{i\omega e}{4\pi\sqrt{2\pi}\epsilon_0 cr} \int_{-\infty}^{\infty} [\boldsymbol{n}\times(\boldsymbol{n}\times\boldsymbol{\beta})]\, e^{-i\omega(t'+r(t')/c)dt'}$$

Assuming the geometry in Figure 2.3, after some algebra the electric field can be rewritten in a more convenient way [12]:

$$E_x(\omega) = \frac{-\sqrt{3}e\gamma}{4\pi\sqrt{2\pi}\epsilon_0 cr} \left\{ \left(\frac{\omega}{2\omega_c}\right) (1+\gamma^2\psi^2)\, K_{2/3}\left[\left(\frac{\omega}{2\omega_c}\right)(1+\gamma^2\psi^2)^{3/2}\right]\right\}, \quad (2.11a)$$

$$E_y(\omega) = \frac{i\sqrt{3}e\gamma}{4\pi\sqrt{2\pi}\epsilon_0 cr} \left\{ \left(\frac{\omega}{2\omega_c}\right) \gamma\psi(1+\gamma^2\psi^2)^{1/2}\, K_{1/3}\left[\left(\frac{\omega}{2\omega_c}\right)(1+\gamma^2\psi^2)^{3/2}\right]\right\}, \quad (2.11b)$$

where K_n are modified Bessel functions of n-th order.

The quantity ω_c used in equation 2.11 is not the same as the one defined in Section 2.2.1, but they differ of a factor 2 [2]

$$\omega_c = \frac{3\gamma^3 c}{2\rho}.$$

[2]Some ambiguities exists in literature concerning the definition of these two values: some authors ([33], [34]) use the same name for both, while [12] distinguish the former, calling it *typical frequency*. However, in both cases ω_c has the physical meaning of a *cut-off* frequency for the spectrum. To remove every ambiguities, from now *cut-off* is defined according to Section 2.2.2.

From the equations 2.11, some characteristics of synchrotron radiation field are now clear. The radiation has two polarisation modes, a vertical mode (or π-mode) and a horizontal mode (or σ-mode), shifted of $\pi/2$, thus the emitted radiation is circularly polarised on the xy plane. Both modes depend only on the vertical angle ψ and for $\psi = 0$ the π-mode is null and the σ-mode has its maximum value. The π-mode is antisymmetric with respect to ψ, while the σ-mode is symmetric.

2.2.3 Power in the frequency domain

Equation 2.5 expresses the relation between the angular power density and the electric field. The same relation can be expressed in frequency domain:

$$\frac{d^2P}{d\Omega d\omega} = \frac{2r^2|E(\omega)|^2}{2\pi\mu_0\rho}, \tag{2.12}$$

where $|E(\omega)|^2$ is the quadratic sum of the two components of equation 2.11. The total emitted power is the sum of the power emitted in the vertical and the horizontal directions:

$$\frac{d^2P}{d\Omega d\omega} = \frac{e^2\gamma^2}{9\pi\epsilon_0\rho}\,[F_\sigma(\omega,\psi) + F_\pi(\omega,\psi)].$$

$F_\sigma(\omega,\psi)$ and $F_\pi(\omega,\psi)$ are two functions containing the square of the term in braces of equation 2.11. We can rewrite the equation including the total power P_0 emitted by the particle; so the angular spectral power density becomes:

$$\frac{d^2P}{d\Omega d\omega} = \frac{P_0\gamma}{\omega_c}\,[F_\sigma(\omega,\psi) + F_\pi(\omega,\psi)]. \tag{2.13}$$

The distributions $F_\sigma(\omega,\psi)$ and $F_\pi(\omega,\psi)$ are shown in Figure 2.4. The power radiated is higher and more collimated for frequencies close to the critical frequency. The intensities of the two polarisation at given frequency are very different. It can be proved [12] that the σ-mode radiates seven times more energy than the π mode.

For many applications one is only interested in the spectral power density of the radiation. Thus, equation 2.13 is integrated over the solid angle and gives:

$$\frac{dP}{d\omega} = \frac{P_0}{\omega_c} S\left(\frac{\omega}{\omega_c}\right), \tag{2.14}$$

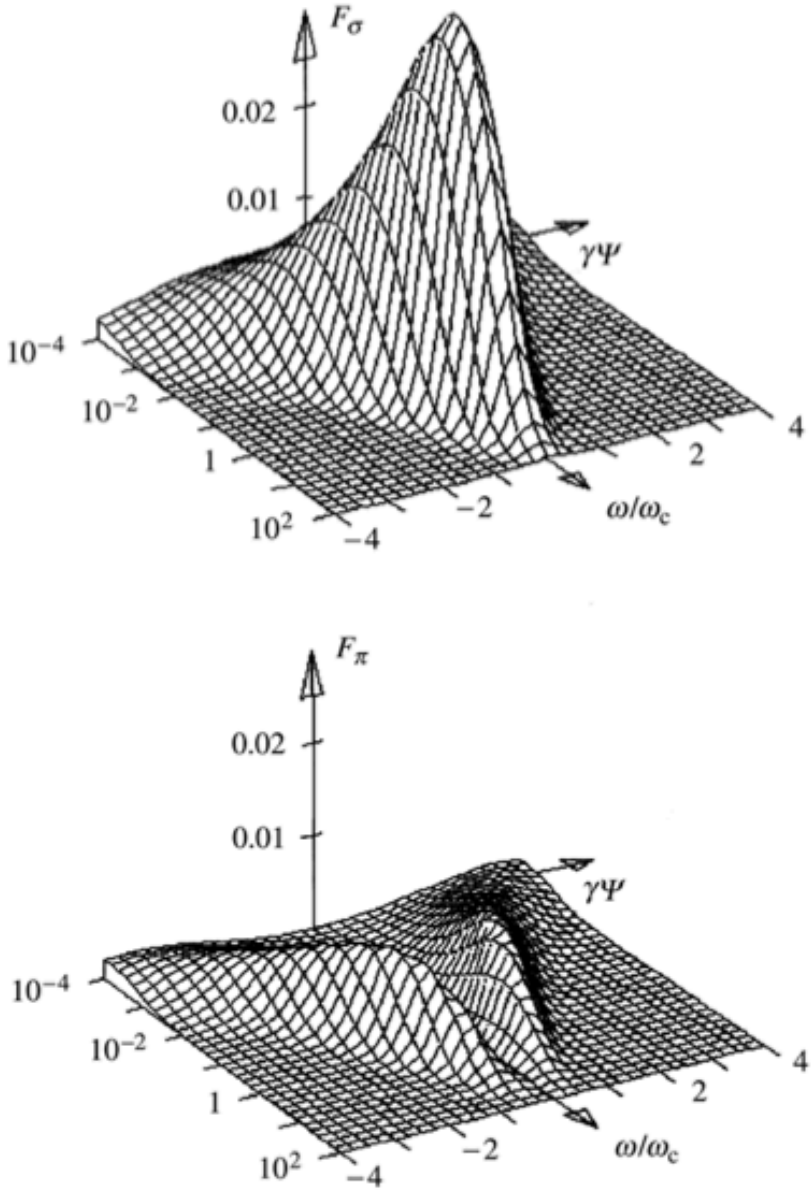

Fig. 2.4 Spectral angular power density for the two polarisation modes: $F_\sigma(\omega,\psi)$ and $F_\pi(\omega,\psi)$. [36].

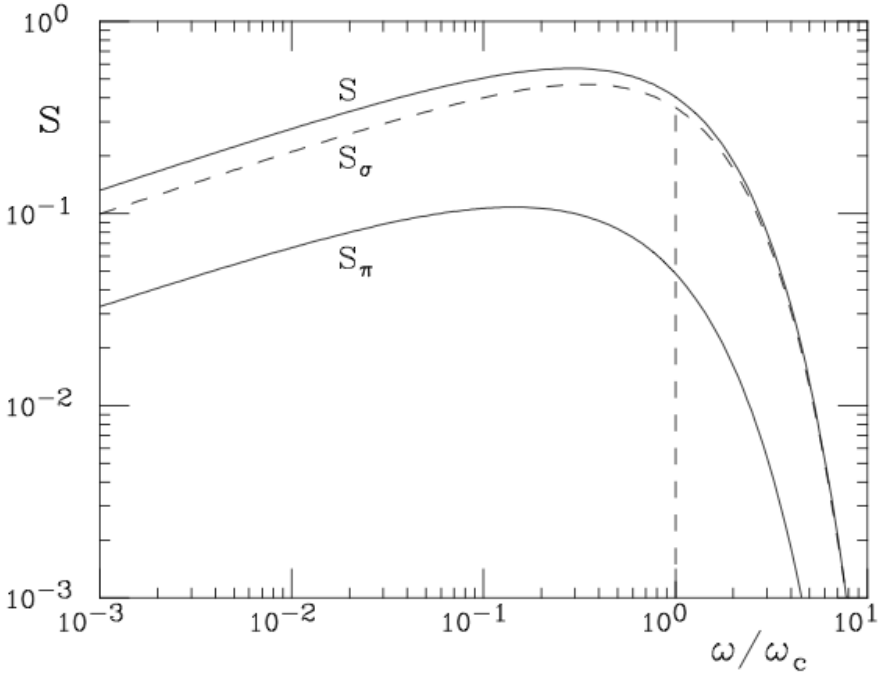

Fig. 2.5 Normalised spectra $S\left(\frac{\omega}{\omega_c}\right)$. [36].

where $S\left(\frac{\omega}{\omega_c}\right)$ is the normalised spectral density (Figure 2.5):

$$S\left(\frac{\omega}{\omega_c}\right) = \frac{9\sqrt{3}\omega}{8\pi\omega_c}\int_{\omega/\omega_c}^{\infty} K_{5/3}(z)dz. \tag{2.15}$$

The critical frequency splits the spectrum into two regions of the same area, hence half of the power is radiated below the critical frequency and the other half above it [12].

2.2.4 Photon distribution

So far we have considered the radiation only from a classical point of view. The spectrum in Figure 2.5 may be interpreted as a photon distribution. The photon are emitted in quanta of energy $\epsilon = \hbar\omega$. It is possible to interpret spectra in terms of the ratio $u = \omega/\omega_c = \epsilon/\epsilon_c$, where ϵ_c is the critical energy. From equation 2.15, the normalised emitted intensity over the interval du is given by $S(u)du$. Let $n(u)du$ be the number of photons emitted in certain energy, then the following equality holds:

$$un(u)du = S(u)du.$$

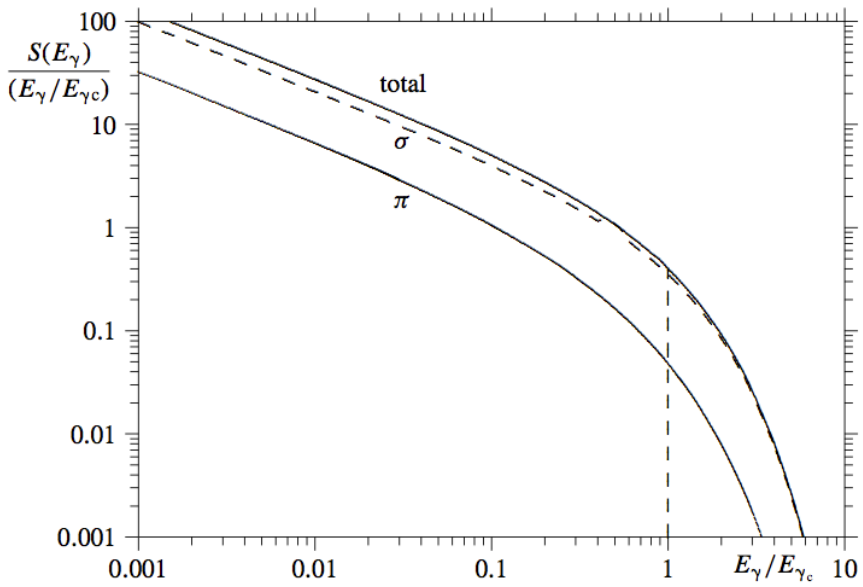

Fig. 2.6 Normalised photon spectra $S(u)/u$. [36].

So, the normalised photon spectra is $n(u) = S(u)/u$, which gives the normalised density of photons (Figure 2.6). From the previous relation the total number of photon emitted is:

$$N = \frac{P_0}{\epsilon_c}\int_0^\infty \frac{S(u)}{u}du = \frac{15\sqrt{3}}{8}\frac{P_0}{\epsilon_c}. \tag{2.16}$$

The average energy is:

$$\langle\epsilon\rangle = \frac{1}{N}\int_0^\infty \epsilon n(\epsilon)d\epsilon \approx 0.31\epsilon_c,$$

and the variance:

$$\langle\epsilon^2\rangle = \frac{1}{N}\int_0^\infty \epsilon^2 n(\epsilon)d\epsilon = \frac{11}{27}\epsilon_c^2.$$

2.2.5 Angular distribution

The angular distribution can be obtained from equation 2.13 for a fixed frequency ω. In Figure 2.7, one can see how the distribution changes for the two polarisation modes (and their sum) for different frequencies. As expected, the vertical mode is null in the origin, while the horizontal mode is decreasing with increasing the angle. One can see the typical width γ, argumented in Section 2.2.1 as a good approximation of the distribution width close to the critical frequency. The farther the frequency is from the critical frequency, the wider

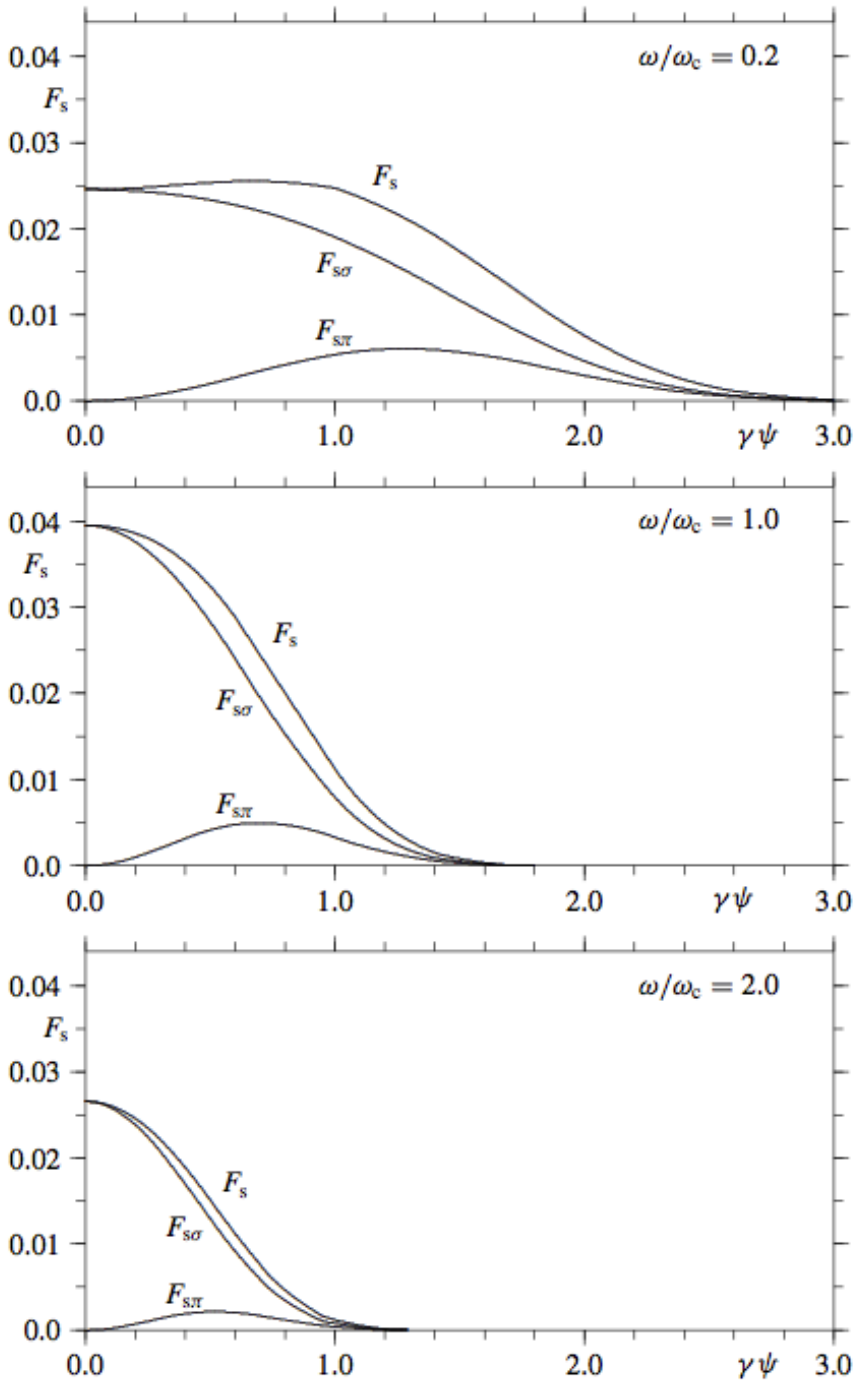

Fig. 2.7 Angular distribution for the two polarisation modes and their sum at different ω. Only the distribution for positive angles is shown, however the distribution is symmetric. [12].

the spectrum is. It is interesting to note that each frequency has its own natural opening angle.

The rms of the distribution is a good estimation for the opening angle of the radiation. For the π-mode, the averaged squared of the product between the angle and the Lorentz factor is:

$$\langle \gamma^2 \psi^2 \rangle_\pi = \frac{\int_0^\infty \gamma^2 \psi^2 F_\pi(\omega, \psi) d\psi}{\int_0^\infty F_\pi(\omega, \psi) d\psi}; \tag{2.17}$$

something similar can be written also for the second mode. The variance of the opening angle for the total distribution can be obtained as the weighted sum of the two components:

$$\langle \gamma^2 \psi^2 \rangle = \frac{S_\pi \langle \gamma^2 \psi^2 \rangle_\pi + S_\sigma \langle \gamma^2 \psi^2 \rangle_\sigma}{S_\pi + S_\sigma}.$$

Sometimes equation 2.17 is better expressed for $\omega \ll \omega_c$. Details of this approximation will not be discussed here, but they are widely described in [12]. This yields the following rms angles:

$$\psi_{\sigma-rms} = 0.4097 \left(\frac{\lambda}{\rho}\right)^{1/3}, \tag{2.18a}$$

$$\psi_{\pi-rms} = 0.5497 \left(\frac{\lambda}{\rho}\right)^{1/3}, \tag{2.18b}$$

$$\psi_{rms} = 0.4488 \left(\frac{\lambda}{\rho}\right)^{1/3}. \tag{2.18c}$$

These rms angles are independent of the Lorentz factor and they depend only on the wavelength and the curvature radius. This approximation is useful in many practical applications and in particular for beam diagnostics, for which visible light is often used. This is in agreement with a larger critical frequecny

2.3 Short magnet approximation and edge effect

In the previous sections we assumed the radiation emitted from an electron traversing a long magnet with constant magnetic field. In the context of synchrotron radiation, a magnet is defined long when the arc of the electron trajectory, which is seen by an observer, is smaller than the magnet length. This is equivalent to saying that the deflection angle is $\gg 1/\gamma$. Coïsson first pointed to the effect of a short magnet on the radiation distribution [38].

The main difference with the long magnet case arises for the pulse length. In this case the natural aperture of the radiation cone does not determine the observed arc length. Let us

consider a short magnet with length $L \ll \rho/\gamma$. A similar approach to Section 2.2.1 yields to a pulse duration (assuming a relativistic particle):

$$\Delta t = \frac{2\rho}{\beta c} \arcsin\left(\frac{L}{2\rho}\right) - \frac{L}{c} \approx \frac{L}{\beta c}(1-\beta) \approx \frac{L}{2c\gamma^2}.$$

Therefore the critical frequency is:

$$\omega_c \approx \frac{2c\gamma^2}{L},$$

which is greater than the usual long magnet critical frequency. Short magnets in principle can be designed to give an arbitrary spectrum.

The theoretical description in [38] starts from equation 2.2a and follows the same steps of Section 2.2. Using the results given in [38] we can summarise the main differences with the regular case.

All the radiation is concentrated in an angle smaller than $1/\gamma$, and this is fairly in agreement with the critical frequency bigger than in the regular case. The radiation field has two polarisations and it is linearly polarised. However this can change for some magnetic fields [38].

The power per solid angle is:

$$\frac{dP}{d\Omega} = C^2\gamma^6 f^2(\psi,\phi) \int B^2(z)dz, \tag{2.19}$$

where $C = 5.5 \times 10^{-8}$ cm$^{3/2}$s$^{-1/2}$, $B(z)$ the magnetic field along the particle trajectory, and $f(\psi,\phi)$ an angular distribution function similar to $F(\psi,\omega)$ (in this case ψ and ϕ are respectively the vertical and horizontal angle between the tangent to the trajectory and the observation direction). The integral of 2.19 gives the total energy emitted:

$$W = \frac{\pi C^2}{6c}\gamma^6 \int B^2(z)dz.$$

The spectrum is obtained from the Fourier transform of equation 2.19. The result, according to [38] is:

$$\frac{dP}{d\omega} = \frac{1}{4}C^2\gamma^2 \int_0^{2\pi} d\phi \int_0^{\infty} \psi d\psi f^2(1-\gamma^2\psi^2)^2 B^2\left(\frac{1+\gamma^2\psi^2}{2\gamma^2}\nu\right).$$

The edge effect is the radiation emitted when a charge particle is entering (or leaving) a region with a constant magnetic field whit fall-off distance, L smaller than ρ/γ [39]. Cal-

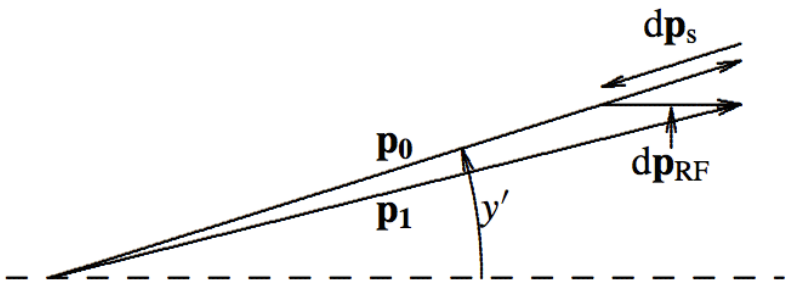

Fig. 2.8 Damping of betatron oscillations due to photon emission combined with rf acceleration. [12]

culation for this case will be the same as the short magnet (within some approximations [38]).

2.4 Transverse beam dynamics including synchrotron radiation

2.4.1 Radiation damping

The presence of synchrotron radiation alters the equation of motion found in Section 1.1. The particle, as a system, is subject to a dissipative force, which cause energy losses, hence the constant of motion in equation 1.5 is no longer constant. One may say synchrotron radiation is responsible for a damping of oscillations. The electron radiates energy in the direction of motion reducing the momentum components in all directions. When the electron passes through the RF cavity, only the longitudinal component for the momentum is restored (Figure 2.8). Therefore, turn after turn, the transverse phase space is reduced and the emittance decreases.

We will study only the radiation damping of the vertical oscillations. This is a more straightforward case than the horizontal damping, because the electron storage rings are often designed with negligible vertical dispersion. The extension of this simple model to the horizontal and longitudinal case is tackled in [40]. During the emission neither the position y nor the angle y' are changed,while the total momentum p_0 is reduced to $p_1 = p_0 - \delta p$. The RF cavity restores only the longitudinal momentum by a quantity p_{RF}, hence the angle is reduced by

$$y' = \frac{p_y}{p_L + p_{RF}} \approx \frac{p_y}{p_L}\left(1 - \frac{p_{RF}}{p_L}\right) = y'\left(1 - \frac{p_{RF}}{p_L}\right).$$

If the energy restored in the cavities is equal to the energy losses we have

$$\delta p = -p_{RF} = U_0/E, \quad \text{hence} \quad y' = y' \left(1 - \frac{U_0}{E}\right).$$

U_0 is the total energy loss per turn from equation 2.10 and E the nominal energy of the particle.

After one turn, the emittance of 1.5 is then reduced of

$$\delta\epsilon_y = -2\frac{U_0}{E}(\alpha_y y y' + \beta_y y'^2).$$

Averaging the previous relation over many turns (as shown in [40]), yields

$$\delta\epsilon_y = -2\epsilon_y \frac{U_0}{E},$$

and for the time interval dt:

$$\frac{d\epsilon_y}{dt} = -\epsilon_y \frac{U_0}{2ET_{rev}},$$

where T_{rev} is the revolution time of the particle. Hence,

$$\epsilon_y(t) = \epsilon_y(0)e^{-t/\tau_y},$$

where the vertical radiation damping time τ_y is:

$$\tau_y = \frac{2ET_{rev}}{U_0}.$$

2.4.2 Quantum fluctuations

Radiation emission is a quantum process whereby photons are emitted with discrete energies. If the emission process was smooth, the emittance of the beam would be damped to zero. However, the quantum effects hinder the damping process introducing noise into the dynamics of the beam. The beam reaches an equilibrium emittance when the radiation damping balances the quantum fluctuations. The natural emittance is [40]:

$$\epsilon_0 = C\frac{\gamma^2 I_5}{j_x I_2}, \tag{2.20}$$

where $C = 3.832 \times 10^{-13}$, j_x is the horizontal partition number [40] and I_5 and I_2 are known as synchrotron integral and they are defined respectively

$$I_2 = \oint \frac{ds}{\rho^2} \quad \text{and} \quad I_5 = \oint \frac{\mathscr{H}_x(s)}{\rho^3} ds.$$

$\mathscr{H}_x$(s) is the dispersion invariant and it is defined in analogy to the emittance, but using the dispersion functions. It is constant in focusing and drifts, but it changes in bends:

$$\mathscr{H}_x(s) = \gamma_x D_x^2(s) + 2\alpha_x D_x(s) D_x'(s) + \beta_x D_x'^2(s).$$

Dispersion and it slope are critical parameters in the design of electron storage rings, as they determine the achievable equilibrium emittance.

Chapter 3

Imaging and characterisation of synchrotron radiation in IOTA

In Chapter 2, the main properties of the synchrotron radiation were exposed as well as some beam diagnostic techniques. In this chapter, we will focus on the imaging process which leads to a measurement of the beam cross section. Even though the study of the imaging process is essential for every beam monitor based on synchrotron radiation, the literature is scarce. Some hints are present in textbooks [12], and in journal articles [41]. The image of a beam cross section may be affected by systematic errors, which are different for different rings (examples are discussed in Refs. [42] [43]).

In this chapter, we discuss beam image formation in IOTA and we present a method for studying the systematic errors. The first section is a general description of the beam imaging and of some possible sources of errors. The second part characterises the expected properties of synchrotron radiation in IOTA and describe a simplified but realistic approach for obtaining beam images based on Monte Carlo simulations. In the last section, systematic errors on the expected beam images are discussed.

3.1 Imaging formation and optical resolution of the beam cross section

3.1.1 General considerations on diffraction

Diffraction theory is explained in many optics manuals [44]. In general, two limiting cases are considered: Fresnel diffraction and Fraunhofer diffraction.

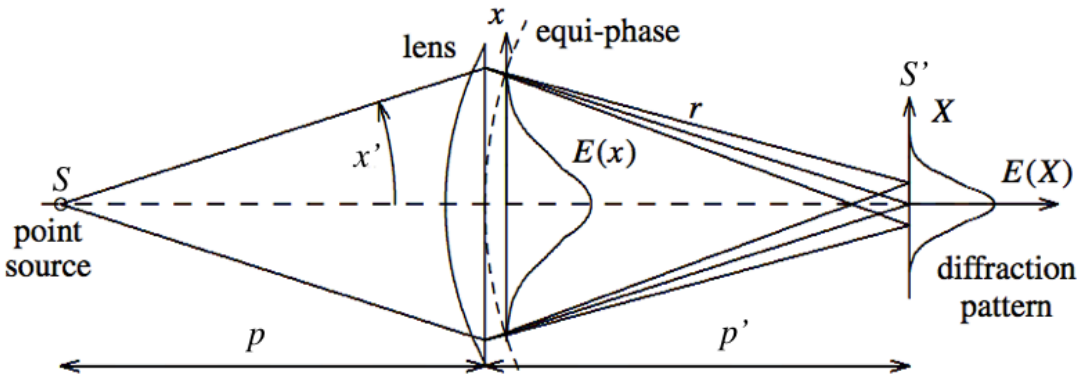

Fig. 3.1 Choice of coordinates: x refers to a position onto the lens plane, X to a position onto the image plane and x' to the radiation angle. The dashed line represent the equi-phase surface arising from the lens. (modified from [12])

For the following chapter we are assuming the geometry of Figure 3.1, where a point source S radiates a wavefront, which is transmitted through the lens in p and is projected onto a screen in the image plane at p'. Let $E(x, y)$ and $E(X, Y)$ be the radiation spatial distributions of the electric field respectively at the lens and at the screen. According to the Huygens-Fresnel principle [44] these two quantities are related through the integral:

$$E(X,Y) = -\frac{i}{\lambda r}\int_{-\infty}^{\infty}\int_{-\infty}^{\infty} E(x,y)e^{ikr}dxdy. \tag{3.1}$$

The quantity k is the wave number and r is the distance between the secondary wavefronts at the lens and a point on the image plane:

$$r^2 = (p'-z)^2 + (x-X)^2 + (y-Y)^2.$$

According to Fermat's principle [44], the optical path from the source to the image is constant. In terms of geometrical optics this explains why the lens deflects all the rays from S in S' . In terms of wave optics, the lens transforms the original wavefront into a spherical wavefront centred in S'. The following relation holds on the spherical equi-phase surface at the lens plane:

$$(p'-z)^2 = p'^2 - x^2 - y^2;$$

r now becomes:

$$r = \sqrt{p'^2 - 2(xX+yY) + X^2 + Y^2} \approx p'\left(1 - \frac{xX-yY}{p'^2} + \frac{X^2+Y^2}{p'^2}\right) + \dots$$

The considerations made so far are general. However, if the emission angle is small, terms on higher order in X/p' or Y/p' are neglected. This is a formulation of the Fraunhofer approximation [44]. For the synchrotron light this condition is often fulfilled. The integral is now:

$$E(X,Y) = -\frac{i}{\lambda p'}\int_{-\infty}^{\infty}\int_{-\infty}^{\infty} E(x,y)\exp\left[i(kp' - \frac{kxX}{p'} - \frac{kyY}{p'})\right]dxdy.$$

With the convenient change of variables $x = px'$ and $y = py'$ the image distribution can be related to the angular distribution at the source. Therefore, up to a phase, the integral becomes:

$$E(X,Y) = -i\frac{p}{p'\lambda}\int_{-\infty}^{\infty}\int_{-\infty}^{\infty} E(x',y')\exp\left[-i\frac{p}{p'}(kx'X + ky'Y)\right]dx'dy'. \tag{3.2}$$

Integral 3.2 is the Fourier transform of the emitted radiation from a point source and it is commonly known as the diffraction pattern for the point source or as Optical Transfer Function [45].

3.1.2 Diffraction of synchrotron radiation

We can apply the theory previously outlined to the case of synchrotron radiation. Equation 2.11a and 2.11b are evaluated in the integral 3.2 to find the horizontal and vertical electric field at the image plane. Solving integral 3.2 is not easy. Moreover, the distributions 2.11a and 2.11b depends of frequency. In the following consideration we assume all the results are obtained for a specific frequency. The diffraction patterns for the two polarisation components are then:

$$\begin{aligned} E_\sigma(X,Y) = iA_0\int_{-\infty}^{\infty}d\phi\int_{-\infty}^{\infty}\left(\frac{\omega}{2\omega_c}\right)(1+\gamma^2\psi^2) \\ \times K_{2/3}\left[\left(\frac{\omega}{2\omega_c}\right)(1+\gamma^2\psi^2)^{3/2}\right]\exp\left[-i\frac{p}{p'}(k\phi X + k\psi Y)\right]d\psi, \end{aligned} \tag{3.3}$$

$$\begin{aligned} E_\pi(X,Y) = A_0\int_{-\infty}^{\infty}d\phi\int_{-\infty}^{\infty}\left(\frac{\omega}{2\omega_c}\right)\gamma\psi(1+\gamma^2\psi^2)^{1/2} \\ \times K_{1/3}\left[\left(\frac{\omega}{2\omega_c}\right)(1+\gamma^2\psi^2)^{3/2}\right]\exp\left[-i\frac{p}{p'}(k\phi X + k\psi Y)\right]d\psi. \end{aligned} \tag{3.4}$$

A_0 is a constant factor. The first integral may be defined only within the angle given by the optical acceptance of the system: $\phi_c \approx 2D/p$, where D is the diameter of the lens. Using

parity arguments, integrals 3.3 and 3.4 become:

$$E_\sigma(X,Y) = iA_0 \frac{\sin(mkX\phi_c)}{mk\phi_c} \int_0^\infty \left(\frac{\omega}{2\omega_c}\right) (1+\gamma^2\psi^2) \times K_{2/3}\left[\left(\frac{\omega}{2\omega_c}\right)(1+\gamma^2\psi^2)^{3/2}\right] \cos(mk\psi Y) d\psi, \tag{3.5}$$

$$E_\pi(X,Y) = A_0 \frac{\sin(mkX\phi_c)}{mk\phi_c} \int_0^\infty \left(\frac{\omega}{2\omega_c}\right) \gamma\psi(1+\gamma^2\psi^2)^{1/2} \times K_{1/3}\left[\left(\frac{\omega}{2\omega_c}\right)(1+\gamma^2\psi^2)^{3/2}\right] \sin(mk\psi Y) d\psi, \tag{3.6}$$

where $m = p/p'$.

The intensity distribution of the diffraction pattern are $I_\sigma \propto E_\sigma^2$ and $I_\pi \propto E_\pi^2$. Obviously $I = I_\pi + I_\sigma$. The X dependence of I is then contained in a term behaving like the square of $\sin(x)/x$. This is similar to the diffraction pattern for a fully illuminated circular lens [44], hence the width of the distribution along this direction depends only on the optical acceptance of the system. In the Y direction, the diffraction pattern is the integral and does not depends on lens acceptance[1]. The rms size or the full width at half maximum (FWHM) of the distribution are both good estimations for the diffraction along Y.

3.1.3 Coherence of the emission from multiple particles

So far we have always described synchrotron radiation from one single particle. The case of radiation from an extended plane object such as a particle beam is slightly more complicated because of a spread in position and angle around the nominal values. The particles have also a spread in energy. The radiation frequency depends strongly on the electron energy, and the resulting image broaden because the approximation to a monochromatic source is not longer possible.

In the case of an extended particle distribution a temporal coherence between the radiation emitted by different particles must be taken into account. However, Ref. [12] points to the quantum nature of the photon emission smearing out any constructive interference among field contributions from different electrons. Therefore, the sum of the radiation fields produced by different electrons vanishes on average, and the total intensity is the sum of the individual intensities. Let P_0 be the total power emitted by one electron, then the total power

[1] This is true as long as the acceptance is bigger than the rms size of the distribution.

emitted by a distribution of N electrons is:

$$P \sum_{i=1}^{N} P_0 = N P_0$$

P can be also called incoherent power.

However, if the wavelength λ of the observed radiation is longer than the bunch length: $\lambda > \sigma_s$, all the electrons emit radiation with the same phase. At this wavelength the bunch behaves like a macro-particle with charge Ne, hence the fields emitted by each individual electrons are added [12] resulting in a coherent power:

$$P_{coh} = N P_{inch} = N^2 P_0.$$

The energy dispersion and the coherence effect may be neglected in many practical cases on long magnets [41], because the bandwidth of the radiation is much larger than the changes in frequency introduced with the energy dispersion, and because the condition of coherence is fulfilled only by a small part of the spectrum at very low frequencies.

3.1.4 Systematic errors from diffraction and depth of field

Imaging a single point on a screen in the image plane yields a halo around the expected position due to diffraction. Hence, the image of an extended spatial distribution is the superposition of all the halos generated by each single point. This stretches out the expected image. Let $\Theta(X, Y)$ be the geometrical distribution at the image plane of the object. The intensity distribution of the image may be written including the diffraction pattern as the convolution of Θ with the intensity distribution I of Section 3.1.2:

$$F(X, Y) = \int \int \Theta(X_1, Y_1) I(X_1 - X, Y_1 - Y) dX_1 dY_1. \tag{3.7}$$

As consequence of this the width of F is approximately:

$$\sigma_F^2 \approx \sigma_\Theta^2 + \sigma_I^2. \tag{3.8}$$

In the case of a beam with a size comparable to the diffraction pattern size, this effect may introduce an important distortion of its image cross section.

More systematic errors come from an effect known in photography as depth of field. Because synchrotron light is emitted tangentially, the optical system allows to see only a finite arc of the whole circumference. If the time resolution of the camera was comparable

Table 3.1 Synchrotron light quantities in IOTA relative to one electron.

Energy	(MeV)	150	100	70
Critical frequency ω_c	(s^{-1})	1.64×10^{16}	4.85×10^{15}	1.66×10^{15}
Energy loss/turn U_0	(eV)	63.98	12.64	3.03
Radiated power P_0	(eVs^{-1})	4.80×10^{8}	9.48×10^{7}	2.28×10^{7}
Emission angle $2/\gamma$	(mrad)	6.8	10.2	14.6
Emitted photons N_{tot}	(photons/turn)	19.30	12.87	9.01
Observed photons N_{bm}	(photons/rad/turn)	2.09×10^{-2}	2.09×10^{-2}	2.09×10^{-2}
Average photon energy $\langle \epsilon \rangle$	(eV)	3.31	0.98	0.34

to the revolution time of the beam, one would observe a moving dot of light, corresponding to the beam moving along the arc of trajectory, the optical system allows to see only a finite arc. However, the time resolution of conventional cameras is usually orders of magnitudes larger than the revolution time, hence, the resulting image is a superposition of different image of the beam moving along the arc. As one may expect, if the beam is far from the focal point, then the image will appear more blurred affecting the observed size. An estimation of this effect is not straightforward. In some articles (Refs. [42] [46]) an analytical attempt is made, but in general a numerical approach is preferred, as discussed in Section 3.3.

3.2 Characterisation of the synchrotron radiation in IOTA

Here we present analytical and numerical calculations of synchrotron light properties for the IOTA ring

3.2.1 Photon emission

With the procedure outlined in Sections 2.2.3 and 2.2.4 , we obtained the main properties of synchrotron radiation in IOTA for the three nominal energies 70, 100 and 150 MeV (Table 3.1). The integration in equation 2.15 was performed numerically. The camera can see only a small portion of the circumference, hence the total number of photon must be multiplied by the optical acceptance, which is approximated with the natural synchrotron light emission cone $1/\gamma$.

The diffraction pattern for a single electron has been calculated. The quantities used are listed in Table 3.2 and they are related to the physical dimension of the beam monitor discussed in Chapter 4. Integrals in equations 3.5 and 3.6 are evaluated numerically and the total intensity has been found as explained in Section 3.1.2. In Figures 3.2b and 3.2b it is

shown the horizontal and vertical intensity distributions, while the colour map image of the expected diffraction pattern from one electron is shown in Figure 3.2c. The spot size is of the order of 10 μm.

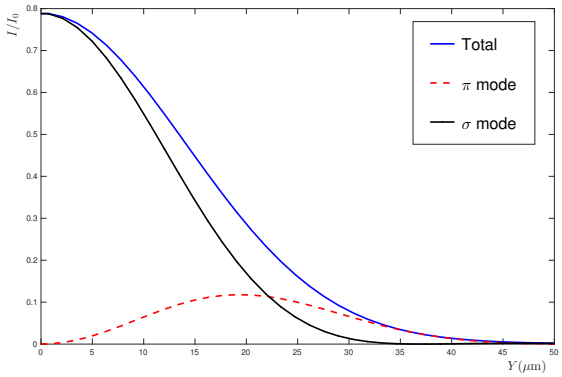

(a) Vertical.

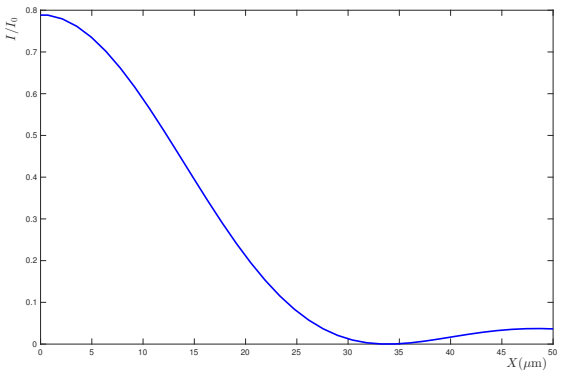

(b) Horizontal.

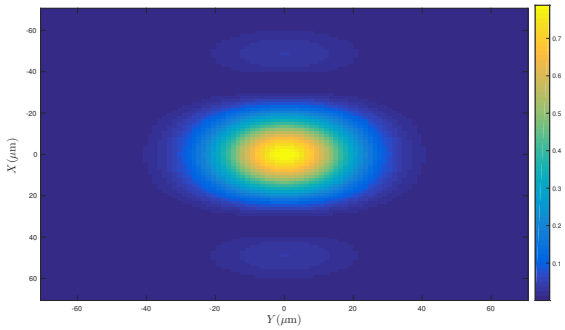

(c) Colour map.

Fig. 3.2 Normalised diffraction patterns for green light (530 nm) and critical angle $1/\gamma$.

For a polychromatic source, the diffraction pattern is the sum of all the monochromatic contributions. This obviously increases the total width of the intensity distribution. In addition, a polychromatic light introduces aberrations which may spoil the resolution of the image. For this reason, a monochromatic filter is often mounted between the emission point and the lens. Unfortunately, using of a filter reduces the expected number of photons seen by the monitor, thus it is important to select a proper wavelength.

The presence of a filter is envisage also in IOTA, hence its consequences on the number of photons were explored. The expected number of photons per electron on a beam monitor for different filters (blue, green and red) at 150 MeV were calculated from equation 2.16 integrated on an interval given by the frequency band of the filter ($\pm$20 nm in our case). The

Table 3.2 Realistic values chosen for the simulation of the beam image in IOTA. The variable optical aperture can be controlled with a diaphragm positioned near the focusing lens.

p (mm)	877.816
p' (mm)	734.857
f (mm)	400
Max. Aperture (mm)	36
Min. Aperture (mm)	6
ω (s^{-1})	3.557×10^{15}

Table 3.3 Comparison between the expected number of photons and the rms sizes of the angular distribution for blue (473 nm), green (530 nm) and red (685 nm) light at 150 MeV.

Wavelength (nm)	473	530	685
N (photons/turn)	1.97×10^{-4}	2.28×10^{-4}	3.13×10^{-4}
rms (mrad)	3.94	4.09	4.46

results are in Table 3.3, compared with the rms size of the respective intensity distribution from equation 2.18c[2].

A good compromise between number of photons and small emission cone is reached with green light, and this is the filter that was chosen for the IOTA system.

3.2.2 Energy dispersion and coherence

In Section 3.1.3, it was pointed out that energy dispersion and coherence are in general negligible. Nevertheless, we are interested to verify if this is true in the case of IOTA.

In IOTA, the relative energy dispersion $\Delta E/E$ of the electron beam is foreseen around 1.4×10^{-4}. The same dispersion can be expressed in terms of the Lorentz factor $\Delta\gamma/\gamma = \Delta E/E$, which yields a dispersion of the critical frequency $\Delta\omega_c/\omega_c = 3\Delta\gamma/\gamma \approx 5 \times 10^{-4}$. A small coherence region is present in every power spectra of synchrotron radiation. The position of this region depends on the bunch length. In IOTA, the largest expected bunch length is 20 mm, so the frequency limit for the coherence region is around 9.42×10^{10} Hz. This frequency is five orders of magnitude smaller than the frequency of visible light and six orders of magnitude smaller than the critical frequency. The use of a filter in the visible band will cut any possible coherence effect on the emitted power.

[2]In the case of visible light $\omega \ll \omega_c$, hence equation 2.18c can be safely used.

3.2.3 Monte Carlo simulation for realistic imaging of the beam

Some authors attempt a description of the depth-of-field effect discussed in Section 3.1.4 using a numerical approach. At the best of our knowledge, one of the most complete description was made by Andersson in Ref. [42] for the MAX-II storage ring in Germany. The article assumes that the light emitted from an arc slice having a Gaussian distribution both in the vertical and the horizontal direction. The contributions from different slices are then summed and convoluted with a function, which takes into account the light transmitted through the optical acceptance to the image plane.

For this study, we will use a Monte Carlo simulation to estimate the depth-of-field effect. A simulation has the advantage of using the real angular distribution instead of making assumptions on it, but it requires a longer processing time. The following results were obtained generating $N = 10^5$ events. This number was a reasonable compromise between processing time and accuracy.

At first two sets of N coordinates (x, x') and (y, y') are generated using the Monte Carlo. (x, x') and (y, y') can be interpreted as the coordinates in phase space for the photon beam radiated by an electron beam. The spatial coordinates x and y have the same Gaussian distribution of the electron beam. The angles y' have the distribution of the synchrotron light of equation 2.13 for the green light, while the x' have a constant distribution over the critical angle $1/\gamma$. Some assumptions are made on the original electron beam. First the energy of the electrons is supposed constant along the small arc considered, even after the photon emission. In this way, the same angular distribution may be used for all photons. Second, fluctuations in the emission of photons are not taken into account: the overall beam radiates the same number of photons in each slice of the arc. Third, x and y are assumed constant along the arc.

The photon beam is then projected onto the image plane using the transfer matrix formalism [44]. At first, the beam experiences a drift from its object plane to the lens,where is focused, and then it drifts again toward the image plane. During this process, the beam coordinates transforms according to:

$$\begin{pmatrix} X \\ X' \end{pmatrix} = M \begin{pmatrix} x \\ x' \end{pmatrix}, \tag{3.9}$$

where M is the transfer matrix given by:

$$M = \begin{pmatrix} 1 & p' \\ 0 & 1 \end{pmatrix} \begin{pmatrix} 1 & 0 \\ -\frac{1}{f} & 1 \end{pmatrix} \begin{pmatrix} 1 & p \\ 0 & 1 \end{pmatrix}. \tag{3.10}$$

The first and the last matrices are drifting matrices respectively from the lens to the image plain (p') and from the object plain to the lens (p), while the central matrix is the focusing matrix with focal length f. X and X' are respectively the coordinates and the angles of the photon beam on the image plane. The same formulas are valid for the vertical coordinates.

X and Y are calculated for 100 different positions along the arc and the contributions of every slice is summed. Within the assumption of a negligible beam transverse change, the horizontal photon distribution may be generated only once and then shifted by a proper offset for simulating motion along the arc. After the first drift, the vertical and horizontal position of the photon is compared with the optical acceptance and all the data outside the optical acceptance are removed.

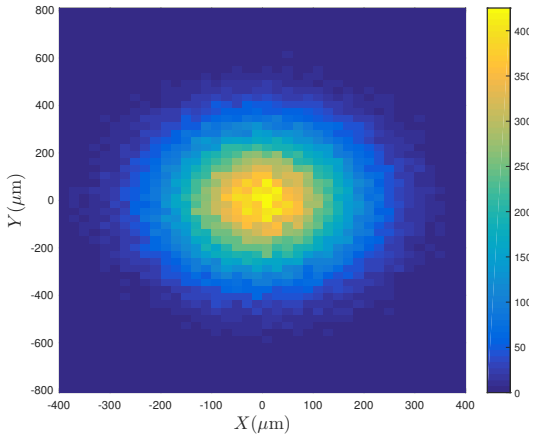

(a) Object plane

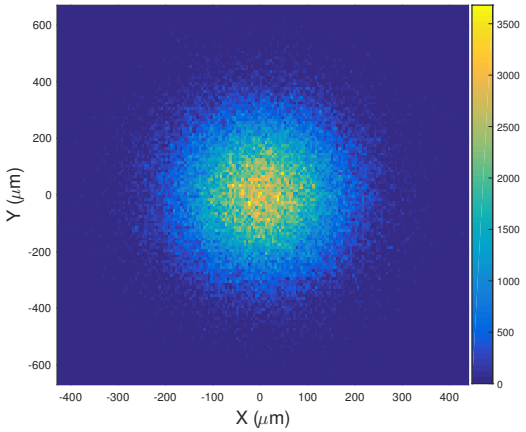

(b) Image plane at $D = 6$ mm.

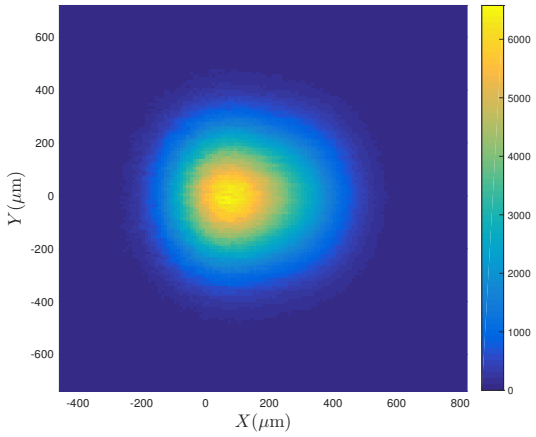

(c) Image plane at $D = 36$ mm.

Fig. 3.3 Colour maps showing the photon distribution generated from the Monte Carlo simulation for a beam with $\sigma_x = 120.72$ μm and $\sigma_y = 192.74$ μm.

The beam sizes used for the simulations are some of the expected beam sizes for the different integrable optics experiments in IOTA and all the other inputs are from Table 3.2. Figure 3.3 shows three realistic images of the expected beam circulating in IOTA at the first beam monitor (SRM-1) in the typical case of an experiment with one nonlinear lens ($\sigma_x = 120.72$ μm and $\sigma_y = 192.74$ μm). The colour map of the the photon beam distribution is plotted in three different conditions: the first two at the image plane for different optical acceptances, $D = 6$ mm (Figure 3.3b) and $D = 36$ mm (Figure 3.3c), while the latter at the object plane (Figure 3.3a). The consequences of the depth of field are clear in Figure 3.3c, where the egg-shaped distortion is due to the light collected over a large arc of the circumference, whereas Figure 3.3b does not.

3.3 Study of the systematic errors

As pointed out in Section 3.1.4, diffraction and depth of field are sources of systematic errors in the beam image cross section. The study here reported was made for a beam cross section $\sigma_x = 120.72$ μm and $\sigma_y = 192.74$ μm, however it can be extended to any cross section.

The error σ_f introduced by the depth of field was estimated as

$$\sigma_f = \Sigma_x - M\sigma_x.$$

Σ_x is the horizontal standard deviation of the simulated distribution, while $M = p'/p$ is the magnification coefficient of the system. As one may guess, σ_f is greater for wide optical acceptances.

The error introduced from diffraction has been estimated numerically from the distributions of Section 3.2.1. Even if the pattern is different from the typical pattern of a point source described by the Airy's theory [44], we used the Rayleigh criterion [44] for estimating the resolution σ_d. According to this, σ_d is the distance between the central peak of the distribution and the position of the first minimum. The effect of diffraction σ_d are larger for very small acceptance. This considerations are valid only for the horizontal direction since the vertical pattern shows no minima. The diffraction for this case is the FWHM of the distribution and does not depend on the acceptance[3].

σ_f and σ_d were both calculated for ten different optical acceptance: from the critical diameter $2p/\gamma = 6$ mm to a maximum of 36 mm, which is the largest possible aperture for our optical system. The two opposite trends of σ_d and σ_f suggests the existence of a special acceptance angle at which they are both minimal.

[3]This is obviously true only if the angle is bigger than the critical angle

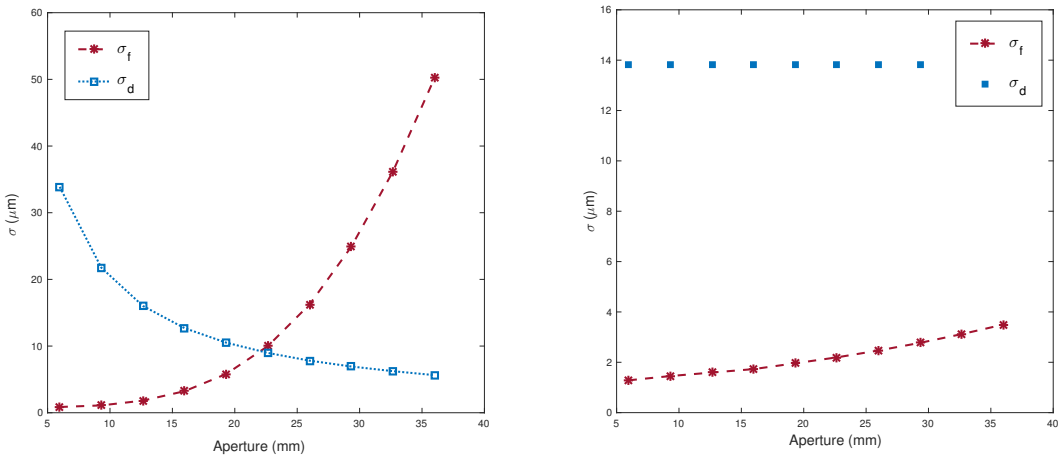

(a) Horizontal.

(b) Vertical .

Fig. 3.4 Depth of field (σ_f) and diffraction (σ_d) error contribution vs. the optical aperture.

Figure 3.4a shows σ_f and σ_d vs. the acceptance. In this case the optimum is not simply present, but it is realised when σ_f and σ_d are equal. At the optimum the total systematic error $\sigma_{tot} = \sigma_f + \sigma_d$ is around 20 μm. The horizontal systematic error is around 20% of the expected image cross section.

A different approach must be used in the case of the vertical distribution. In fact, the diffraction pattern is independent on the acceptance and $\sigma_d \approx$ FWHM/2.355 is equal to 13.8 μm, while the vertical σ_f is shown in Figure 3.4b. Imposing a circular geometry for our optical system, the vertical σ_f was calculated at the same acceptance of the horizontal case. This yields a vertical systematic error of 16 μm, less than 11% of the expected image vertical cross section.

For most experiments, the systematic errors due to depth of field in the arc and to diffraction can be kept under control. However, in some lattice configurations, these distortions can be comparable with the size of the beam. In these cases, it is necessary to modify the setup or to devise means to measure and correct these imperfections directly, for example by recording images of the same beam with different apertures. Two of the critical cases are sorted in Table 3.4.

Table 3.4 Systematic errors for the two smallest beam cross sections. They occur respectively for the experiment with the electron lens (EL) at SRM-2 and for the MacMillan lens (MM) experiment at SRM-1.

	EL SRM-2		MM SRM-1	
	Horizontal	Vertical	Horizontal	Vertical
Expected beam size σ_o (μm)	526	46.6	89.6	381.7
Expected image size σ_i (μm)	440	39.1	75.0	319.5
Selected aperture (mm)	26		20	
Depth of field error σ_f (μm)	7.8	4.7	10	3.0
Diffraction error σ_d (μm)	7.8	13.8	10	13.8

Chapter 4

Design and setup of the beam monitor

In this chapter, we will discuss the design and a possible setup of the synchrotron-light beam monitor for IOTA. Similar beam monitors do not have a standard setup, but are usually designed according to the machine constraints and to the required instrumental resolution. However, all these systems mount a lens and a camera for recoding the images. Moreover, are often included a diaphragm (or sometimes a slit), reducing collected the light and the span of the emission arc, mirrors for bending the light and monochromatic filter wheels for selecting the desired wavelength. Any arrangement of a synchrotron-light monitor for IOTA must include all these elements. In addition, motorised nano-positioners will be mounted on a mirror and under the camera for automatic adjustments of position and of focus of the image.

In the first section of this chapter, we propose an arrangement for the beam monitor with a realistic choice of dimensions, based on the IOTA design constraints and the expected beam sizes discussed in Chapter 1. Relying on these dimensions, a realistic table top prototype was build. We will continue our discussion, describing the instrumentation used for the prototype, including the camera and the nano-positioners. For the latter, a repeatability test has been performed in view of the implementation of automatic positioning and focusing systems. The last section of this chapter is devoted to the main software involved in the data acquisition and in the remote controls of the positioners. The software layout is rather complex and it has been designed to accommodate more beam monitors. A key part is the data analysis system, which processes the incoming information and determines how to move the positioners. The algorithms proposed for this part are described in Chapter 5. In this chapter, we will focus on how they interface with the rests of the software.

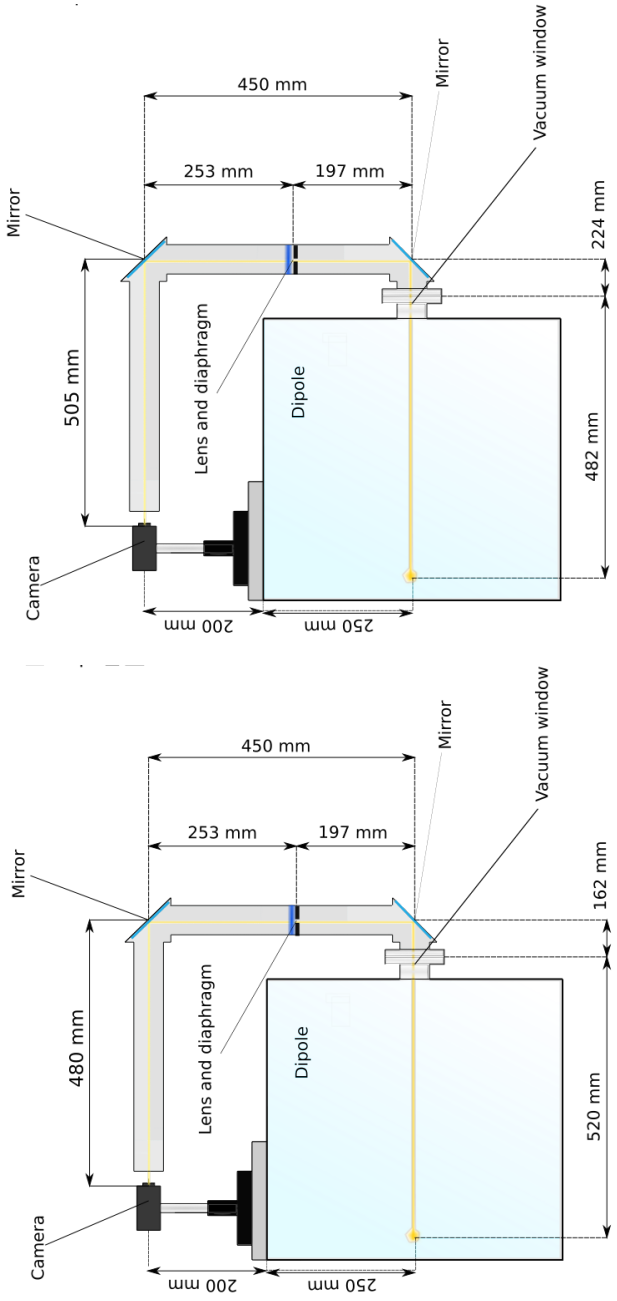

Fig. 4.1 Sketches of the beam monitor with actual sizes of the 30° and the 60° IOTA dipoles. The beam (not shown) at the emission point is tangent to the light emission direction.

4.1 Design

IOTA requires 8 beam monitors, one for each dipole, able to resolve about 1/10 of the expected beam size. The most natural choice is to attach the monitors to the dipoles. In this way, it is easier to arrange the 8 beam monitors along the ring. Therefore, a periscope-like layout is proposed, with two mirrors for transporting the light from the emission point inside the magnet to the top of it, where a camera collects the light (see the sketches of Figure 4.1). In this arrangement, two are the main constrains on the beam monitor dimensions: the size and shape of the magnets determine the minimal dimensions of the beam monitor arms, while the resolution of the beam size determines the position of the lens.

The minimum length of the arms is given by the sum of the distances between the light emission point and the vacuum window from which the light is collected and driven on the camera, and the height of the dipole. These dimensions are different in the 30° and in the 60° magnets and their values are displayed in Table 4.1. The complete blueprints of the dipole are shown in Appendix A.

The resolution affects the position of the lens in the beam monitor. The demanded resolution is about 1/10 of the expected beam size σ , which depends on the experiment configuration and on the position of each dipole We considered a reasonably small beam size around 70 μm. One limit to the resolution is the size of the camera pixels: setting 10 pixels/sigma, leads to a maximum pixel size of 7 μm. Since the pixel size of the camera sensor is 5.86 μm (see Section 4.2.2 for a description of the camera), we can set the the magnification coefficient of the system from the ratio between the two. The result is an overall magnification of 0.837. The position of the lens depends both on the magnification coefficient and on its focal length. By combining the thin lens equation:

$$\frac{1}{f} = \frac{1}{d_o} + \frac{1}{d_i},$$

where d_i is the image-lens distance and d_o the object-lens distance, and the magnification equation:

$$M = -\frac{d_i}{d_o},$$

Table 4.1 Relevant dipole sizes for the synchrotron-light monitor.

Magnet	30°	60°
Vacuum chamber (mm)	520	482
Height (mm)	250	250

Table 4.2 Possible sizes for different focal lengths.

f (mm)	l (mm)	d_o (mm)	d_i (mm)
100	403	219	184
200	806	438	367
300	1210	659	551
400	1613	878	734

we may find the position of the lens, d_o, as function of the focal length. Table 4.2 shows some possibilities, which have to be compared with the constrains of the dipole from Table 4.1. In particular, d_o must be larger than the length of the vacuum chamber, because the lens cannot be placed inside the dipole. Among the different possibilities meeting this requirement, a 400-mm focal length has been preferred, because in this configuration the arms of the monitor are large enough to include a diaphragm, two mirrors and a wavelength filter. An achromatic system with more lenses was not taken into account for simplicity, whereas we plan to use wavelength filters before the lens for reducing chromatic aberrations. The beam monitor arrangement with actual dimensions and the positions of the different components is shown in Figure 4.1.

4.2 Test setup

4.2.1 Overview

From the layouts of Figure 4.1, we built a table-top prototype (Figure 4.2) of the beam monitor, based on the dimensions of the 30˚ dipole. The prototype is used for testing the imaging formation process and for some tests of the automatic image adjustment software. It was build using standard optical equipment from Thorlab. The backbone is made up of standard stands and tubes with 50-mm of diameter, two UV enhanced aluminium mirrors are used for bending the light and a 400-mm convex lens is mounted after a 16-leaves manual diaphragm. A PointGrey BlackFly-PGE-23S6M-C camera is mounted on a movable stage and three Newport 8302 nano-postioners (or picomotors) are included: two on a mirror (for moving the image left and right) and one on the movable stage (for moving the camera back and forth to focus the image). The camera and the picomotors features are described in Sections 4.2.2 and 4.2.3.

The light is provided by a standard diode, emitting red, green and blue light (RGB LED), powered with 9 V DC and connected to a 300 kΩ resistor.

The targed that was used as a test image was different for different purposes:

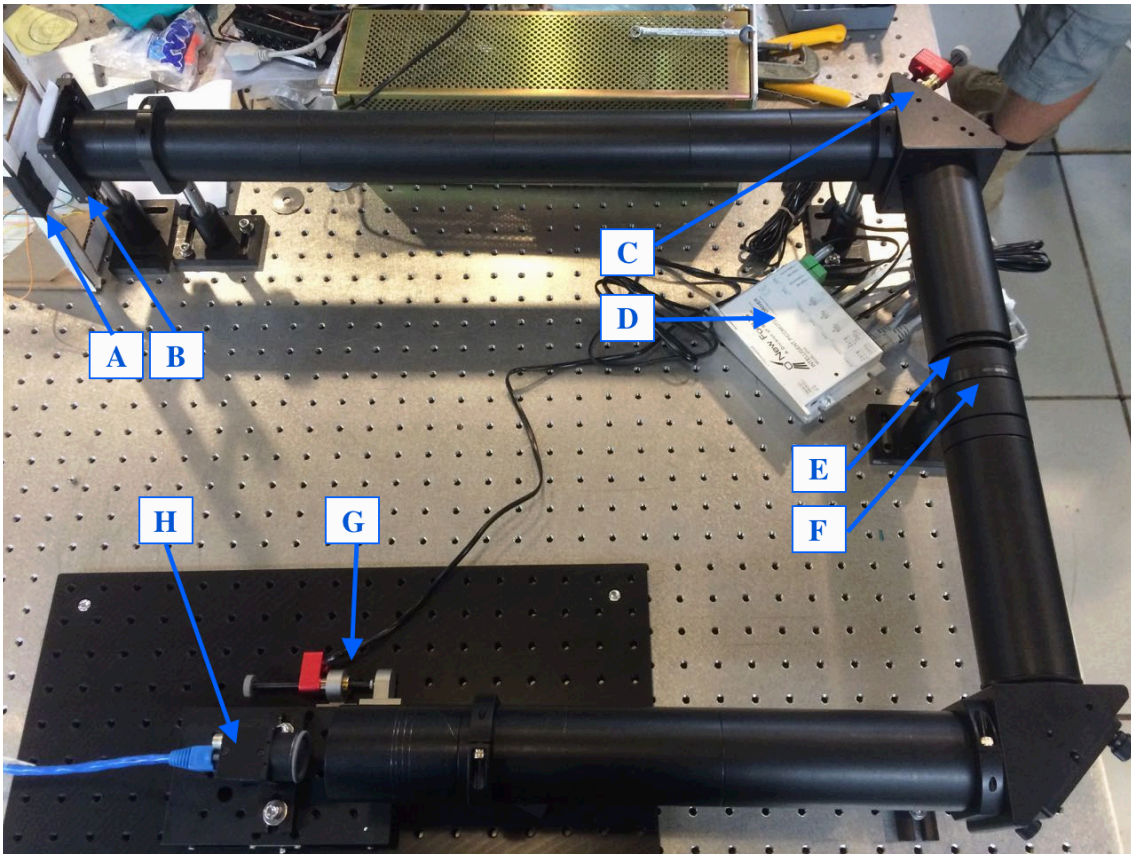

Fig. 4.2 Picture of the table-top prototype. A) LED. B) USAF target. C) Mirror picomotors. D) picomotors driver. E) 400-mm focal lens. F) 16-leaves Diaphragm (1.8-36 mm). G) picomotor and movable stage. H) BlackFly Camera.

- a simple black target with a small hole was used for the picomotor repeatability tests (see Section 4.2.3);
- USAF target (see [47] and Section 5.1.1) was used for the optical characterisation of the prototype, which will be discussed in Chapter 5;
- a Gaussian distribution printed in grayscale on a cardboard sheet for testing the auto-focus algorithm, described in Chapter 5.

4.2.2 Camera

The camera is the heart of the beam monitor based on synchrotron radiation. It must have a small sizes and a good pixel resolution. Other important features include: an high saturation level and a wide dynamic range to accurately reproduce the light intensity distribution

Fig. 4.3 The PointGrey BlackFly-PGE-23S6M-C. [48].

collected by the camera sensor. One other relevant parameter is the exposure time, which determines the amount of light collected by the camera over many turns. We desire in this case a customisable exposure time over a wide range of values for setting it according to the requirements of every experiment and the expected number of photons to avoid saturation. The frame grabbing speed affects the processing time of the automatic centring and focusing algorithms, however it is not one the most relevant parameters.

The camera chosen for the IOTA beam monitor is a PointGrey BlackFly-PGE-23S6M-C (Figure 4.3), which mounts a Sony IMX249 CMOS Image sensor [49]. The camera meets all the requirements outlined before: it has small sizes (29 mm x 30 mm x 29 mm), good resolution (23 MP), 5.86-μm pixel size and a reasonable price.The sensor has excellent saturation capacity (33723 electrons) and a good dynamic range (73.09 dB). The temporal noise is around 4.06 electrons. It has a customisable gain (from 0 to 29.996 dB) and exposure time (from 19 μs to 32 s). The maximum frame-grabbing speed is around 30 frames/s [50].

From the software point of view, the camera interfaces with a PC through GigE Vision, a commercial standard based on the Gigabit Ethernet communication protocol. One of the main advantages of this technology is the high speed transmission rate and the use of low cost standard Ethernet cables. The user can monitor and control the features of the camera through the FlyCapture Program or the FlyCapture Application Programming Interface (API). The FlyCapture program is a generic, easy-to-use image viewer. It allows to view a live video stream from the camera, to save individual images, to adjust the format and to set the camera properties. FlyCapture API allows the user to create custom application to control the camera. It supports different languages such as C, C++ and VB.NET [51]. For the tests in this thesis, both the programs were used: FlyCapture for the tests on the imaging systems reported at the beginning of Chapter 5, while the custom software *BPMServerHard*, used

for extracting informations from the picture (see Section 4.3.1), is based on the FlyCapture API.

The camera will be mounted on the top of the IOTA bending magnets. The stray magnetic field may in principle yield systematic errors and a loss of image quality. Therefore, the camera response was tested in a region with a uniform magnetic field from 60 to 80 G. The magnetic field was measured using an Hall probe. No differences on the image quality were observed in this range.

4.2.3 Picomotors

Positioners are useful on the beam monitor for automatic adjustments of the mirror and camera position in view of automatic focusing and image centring systems. The positioners chosen for the beam monitor are the Newport 8302 picomotor piezo open loop linear actuators (Figure 4.4). They have a minimal incremental motion of less than 30 nm and a maximum speed of 12 mm/min [48]. The positioners mounted on the mirror have a travel range of 25.4 mm, while the one on the movable camera stand has a travel range of 50.8 mm. The time the picomotor takes to perform the action is independent from the direction of rotation and it grows with the number of steps. The greatest number of steps possible is 50,000 steps and it takes around 28 s.

All the devices are connected through three 4-pin single channel output ports to a Newport 8742 Driver (Figure 4.5) which can run all of them asynchronously. The Driver is connected to the Fermilab Accelerator Control Network (ACNET) through an Ethernet port (see Section 4.3.4 for further informations).

The picomotor design relies on the principles of static and dynamic friction. Two jaws grasp an 80-pitch screw and a piezoelectric transducer slides the jaws in opposite directions. The slow action of the picomotor causes the screw to rotate (static friction), while the fast action causes no rotation. By sending pulses with fast rise time and slow fall time, the piezo

Fig. 4.4 The Newport 8302 picomotor piezo linear actuator with 25.4 mm travel range. [48].

Fig. 4.5 The Newport 8742 three port picomotor Driver. [48].

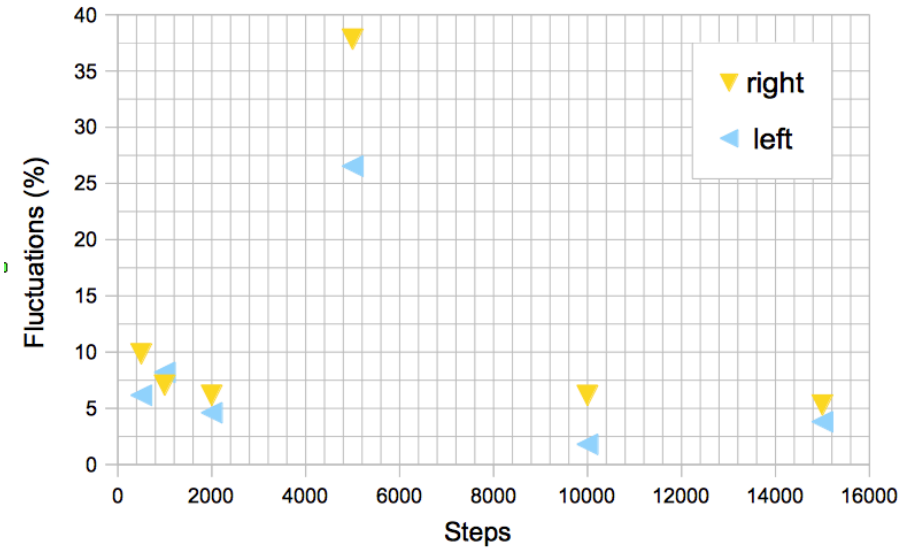

Fig. 4.6 Fluctuations of the path length as function of the number of steps. Right refers to a counter-clockwise movement.

will rotate the screw counter-clockwise. Similarly sending pulses with slow rise time and fast fall time rotates the screw clockwise. The Driver generates the 130 V pulses required to drive the piezo in the picomotor. This technology allows very precise position adjustment, but it does not produce identical steps for identical input impulse. In a closed loop configuration, this does not yield any issue because the devices are equipped with an internal encoder, which returns a feedback on the actual number of steps performed. However, the picomotors purchased for the IOTA synchrotron-light monitor are open loop devices, thus, in absence of any kind of indirect feedback, the actual distance travelled is unknown. However an open loop configuration is still satisfactory if the actual distance travelled will not be too different from the expected distance and if every movement is repeatable within small enough fluctuations. Open-loop picomotors may be used for beam monitoring only if they show a fair enough repeatability, hence a test was carried out.

4.2.4 Picomotor repeatability test

The picomotor is a friction mechanism, thus it does not produce identical steps for each input pulse. In addition, there is a significant variance in step size when starting the picomotor from a standstill or changing its direction. Other factors that affect the linear travel per pulse includes the direction of rotation, the load and the temperature. Repeatability of the

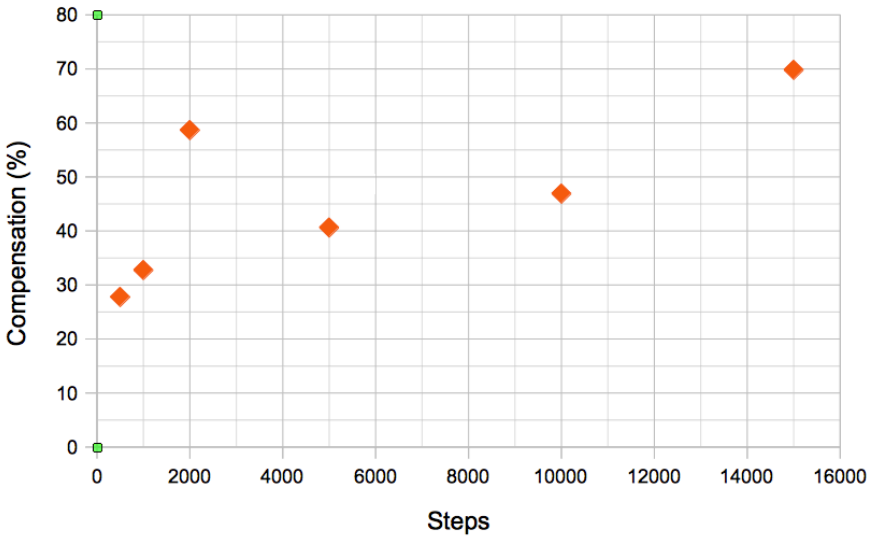

Fig. 4.7 Step compensation in percent that needs to be added in one direction to come back to the starting point.

picomotors was examined to find out whether these variations of the step size are significant or not.

The test was performed on one of the 25.4 mm picomotors on the mirror and for different numberss of steps. The movement of a light dot on the screen (target) was used for measuring the distance travelled by the picomotors. Each movement of the picomotor was detected by a proportional shift of the target on the screen. The position of the target relative to the centre of the screen was returned by the software *BPMServerHard* (see Section4.3.1). A counter-clockwise rotation of the picomotor shifted target to the right of the screen, and vice versa. Each shift was measured ten times All the shifts both on the right and on the left were measured ten times for each chosen number of steps. The fluctuations were then calculated as the standard deviation of these ten measurements. The plot in Figure 4.6 shows the observed fluctuations for both directions. In general fluctuations were around 10%; however for 5000 steps, they were 40%. No explanations to this singular behaviour was found. Figure 4.7 shows the difference between the average left and right shifts as function of the number of steps. These differences are not smaller than 30% and they randomly change with the number of steps. A more qualitative test was performed on the other two picomotors and the same results were found.

This problem affects the feasibility of the automatic adjustment softwares, in particular of the focusing system. At the end of Chapter 5 we present the consequences of this behaviour and the strategies implemented to deal with it. Even though solutions have been proposed

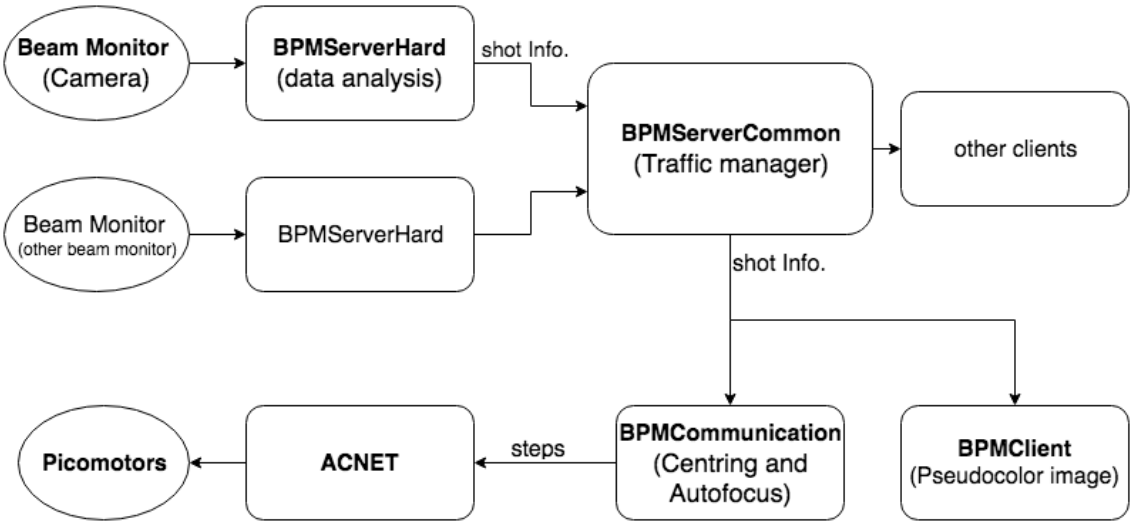

Fig. 4.8 Software layout for the IOTA synchrotron-light monitors.

to deal with non-repeatability, the use of this devices on the synchrotron-light monitor is discouraged.

4.3 Software

We describe now the main program used for the data taking and for image processing. Each beam monitor requires one or more piece of code for processing the incoming informations. In the case of IOTA, the program must be able to process the data from eight different cameras at the same time, to provide the user with the requested informations and to communicate to the remote accelerator network control system any adjustments necessary in the mirror and in the camera positions. In addition, they must cooperate with the others diagnostic tools in the ring. A sketch of the planned software layout can be found in Figure 4.8. The image taken from the camera are first processed by *BPMServerHard* and then transmitted to *BPMServerCommon*, which sorts the informations coming from the different beam monitors and interacts with all the client programs, such as *BPMCommunication*. Many of the software here described are upgrades of similar software conceived for the VEPP-2000 collider in Novosibirsk, Russia [52]. The new software designed for this thesis is *BPMCommunication*, which manages the incoming image informations from *BPMServerCommon* and transmits to the picomotors any necessary adjustment for image position and focus. The software described in this sections was used in a simplified configuration, useful in the case of only one beam monitor.

4.3.1 *BPMServerHard*

BPMServerHard is probably the most important software concerning the beam diagnostics with the synchrotron-light monitor. This software was developed in C++ starting from the FlyCapture API and it has a direct access to each camera and reads the pixel content of each frame. Then, it performs a first basic data analysis, fitting an elliptical beam profile to the data. Saturated pixels and the beam tails might introduce systematic errors, thus the program performs the fit excluding these two critical regions.The beam position x and y are then calculated as well as the horizontal and vertical beam sizes A and B, the amplitude and other useful data, such as the beam profile and a picture with level lines marked by pseudocolours. Client software can request any type of data, according to their purpose.

4.3.2 *BPMServerCommon*

BPMServerCommon handles all the communication between *BPMServerHard* and its client software. It establishes the connection and sends the requested data to their final destination. A minimal graphical interface displays some useful information such as the number of monitor connected and the frame grabbing speed. This software has been developed in Java.

The data processed by *BPMServerHard* and sorted by *BPMServerCommon* can be requested by client software. The two clients used in this thesis are *BPMClient* and *BPMCommunication*

4.3.3 *BPMClient* and *BPMCommunication*

BPMClient is a Java client software manly made up of a practical graphical interface which shows the beam image, displaying the pseudocolour picture from *BPMServerHard*. It returns also the x and y position, A and B, the total amplitude, the highest pixel value and the number of the pixels that have this value. The user can also customises the gain and the exposure and can save the picture in PNG format. It was used to see the image while *BPMServerHard* was running, because in this mode the standard FlyCapture Program of the camera could not be used.

BPMCommunication is the second Java client software which processes the data from *BPMServerCommon*. It has the purpose to analyse the position, transverse sizes and the amplitude of the beam image and to communicate to the picomotors the number of steps to travel for centring and focusing the image. The connection with the server is based upon the *Soket* approach [53]. As soon as the client-server communication is established, the client sends to the server a request for receiving data from the monitor selected by the user. After

that the server starts sending the shot information to the client to be processed. This can happen thanks to the *Server Listeners*, special Java classes which wait for server feedback before performing an action. The shot Information is sent from *BPMServerHard* to *BPMCommunication* through *BPMServerCommon*. The shot information is then read and analysed by the centring and focusing algorithms. Both algorithm ends by choosing a number of steps for the pico-motors. This information is sent to ACNET through a special Fermilab script (integrated into the software) which converts the Java instructions into ACNET commands. More detailed informations on *BPMCommunication*, including the focusing and centring algorithms, are at the end of Chapter 5. In Appendix B, the most relevant lines of codes are selected and commented.

4.3.4 ACNET

All the output information concerning the picomotors is processed by the Fermilab Accelerator Control Nerwork (ACNET). ACNET is the unified control system for the whole Fermilab site, controlling all the accelerators and technical equipment. General communication flows over Ethernet and uses a custom protocol. Each device must be inserted in the system as ACNET device and it is identified by a name composed of 8 characters. Such devices can have different properties including setting, read-back, analog alarms, digital control settings, etc. For the picomotors the most important are the setting properties. Once the IP Address associated to the Picomotots driver and each controller is registered as ACNET device, the communication of the commands can occur according to the SSDN. SSDN is a quad-word which tells the driver what to do once an ACNET device is set by an user or by a software. A set will be interpreted by the driver as a string command to the appropriate picomotor and translated into a proportional signal pulse. More information about ACNET can be found in [54].

Chapter 5

Results

This chapter describes the results of the experimental work done for this thesis, including the technical difficulties that we encountered. The performance of the prototype beam monitor highlighted the strengths and weaknesses of the design and the path for further work.

In the previous chapter, we described a realistic tabletop prototype based on a proposed layout of the synchrotron light monitor, and the software involved in the image taking and processing. In this chapter, we present the tests and characterisation of the beam monitor optics and the feasibility studies of two algorithms for automatic positioning and focusing of the image.

The first part of the chapter is an experimental investigation of the imaging process outlined in Section 3.1. The model previously described may be applied to this set-up after some opportune modifications. Details on the data taking are given in Section 5.1.1, while Section5.1.3 contains the analysis of the image acquired and the discussion of the results.

The second part of the chapter highlights the need for some automatic systems of image focusing and centring. If the focus of the optical system does not coincide with the point along the beam trajectory where synchrotron light is emitted, the final image will be blurred. In IOTA, changes in the beam orbit may arise, hence the arc seen by the monitor is not always the same. For this reason, a self-adjustment of the focal length and of the image position on the screen must be envisaged in order to keep the same image quality. In this thesis we explore the feasibility of a centring (Section 5.2) and of a focusing system (Section 5.3) and we analyse the results of the firstf tests. In view of the the poor repeatability of the picomotors described in Chapter 4, we propose a possible path towards improvements of these automatic procedures.

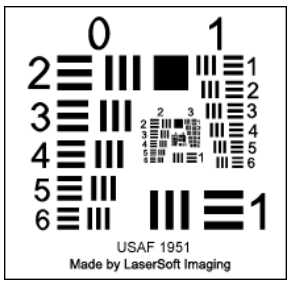

Fig. 5.1 Sketch of the SilverFast USAF 1951 Resolution Target used for the resolution measurements.

5.1 Characterisation of the beam monitor prototype

5.1.1 Resolution target

The accurate description of the prototype and of its setup can be found in Section 4.2. The target used for resolution measurement was the US Air Force target (Figure 5.1), a standard tool for measuring the resolving power of optical devices. Attributes of this target are reported in the Military Standards document [47]. The target consists of a pattern of groups and elements, which decrease in size towards the centre. An element is made up of two sets of three lines at right angles to each other. These lines are separated by spaces equal to the line width, and each line is five time longer than its width. A group consists of 6 elements. The length and the width of each element is mathematically related to the element and the group number according to:

$$\text{Length (mm)} = \frac{2.5}{x}, \tag{5.1}$$

$$\text{Width (mm)} = \frac{0.5}{x}, \tag{5.2}$$

where$x$ depends on the group and the element number of the line pattern observed:

$$x = 2^{\text{group + (element-1)/6}}.$$

Images of the USAF target were taken for the red, green, and blue light and for different diaphragm apertures. The camera settings were changed in every acquisition for keeping the same signal-to-noise ratio between images. Figure 5.2 is an example of one of the images taken as described above.

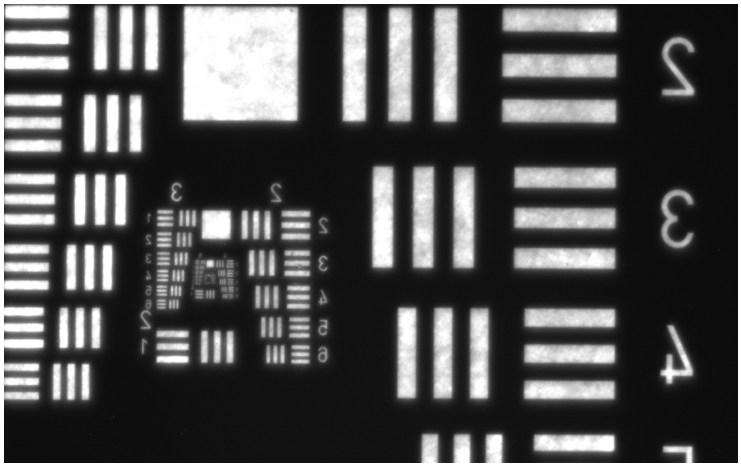

Fig. 5.2 Example of an image of the USAF target, taken with the setup of Section 4.2 with the green light and fully open diaphragm.

A different target was used in the tests of the softwares. The procedure for this case is further detailed in Sections 5.2 and 5.3.

5.1.2 Imaging theory for the prototype

The theory outlined in Section 3.1 was applied assuming a synchrotron light source. This assumption is not valid in the case of images taken using the test setup. Therefore, new assumptions have to be made before moving further in the data analysis.

The fist assumption concerns the light amplitude distribution. According to equation 3.1 and its approximation in the Fraunhofer regime (equation 3.2), the amplitude of the diffracted wavefront at the screen $E(X,Y)$ depends on the amplitude at the lens $E(x,y)$. In our experimental setup, the images are taken using an LED, which has a very different light distribution than the one of synchrotron light. This yields a different diffraction pattern at the image plane. The LED light is not strongly collimated, hence we may approximate it as a far, isotropic emitting source. Therefore, the wavefronts at the lens are plane waves and equation 3.2 is:

$$E(X,Y) = -i\frac{p}{p'\lambda}\int_{-\infty}^{\infty}\int_{-\infty}^{\infty} E(x',y')\exp\left[-i\frac{p}{p'}(kx'X + ky'Y)\right]dx'dy'. \tag{5.3}$$

Airy found a solution for this integral in the case of a circular lens. The intensity distribution of the light at the image plane $I(X, Y)$ is [44]:

$$I(q) = I_0 \left(\frac{2J_1(q)}{q} \right)^2, \text{with } q = \frac{\pi D X}{\lambda p'}. \tag{5.4}$$

D is the diameter of the lens, p' the distance from the lens to the observation point on the screen, J_1 is the first Bessel function and I_0 is the maximum intensity at the centre of the distribution. The same relation holds also for the vertical direction. $I(q)$ is also called Airy distribution. The diffraction σ_d, according to the Rayleigh criterion, is the distance between the maximum and the minimum of the Airy distribution; in this case [44]

$$\sigma_d = 1.22 \frac{\lambda p'}{D}, \tag{5.5}$$

In Section 3.1, we made a second assumption, which is no longer valid in this setup. We supposed a Gaussian spacial distribution of points, which was a reasonable description for the particle distribution of a beam circulating in IOTA. In this setup, the point distribution function is the pattern of USAF target. It is not straightforward to include the whole pattern within a single function. One strategy is to examine one by one the elements of each group. In this way, the point distribution, along the vertical profile, is simply made up of three boxcar functions with width and spacing both given by equation 5.2. The distribution along the longitudinal direction consists of one boxcar function with the same length as the element's length, but in practice its effect is negligible for the following discussion. The resulting distribution is, according to equation 3.8, a convolution between the Airy distribution and the three boxcar functions. Its numerical evaluation (for only one boxcar function) is displayed in Figure 5.3.

5.1.3 Data analysis

The goal of this analysis is to give a quantitative estimation of the resolution and an experimental confirmation of the model previously described. This study is also useful for highlighting aberrations coming from imperfections in the lens and other sources of systematic errors. One can have a rough idea of the resolution of the system by exploiting the properties of the USAF target: the spacing between the strips in each element becomes smaller as the element is closer to the centre of the target. Eventually, the spacing between the lines becomes so small that it is impossible to distinguish the pattern. The spacing at which this occurs estimate the resolution. From Figure 5.2 one may attempt this analysis by eye. However, this is not recommendable, because the human eye is strongly influenced by

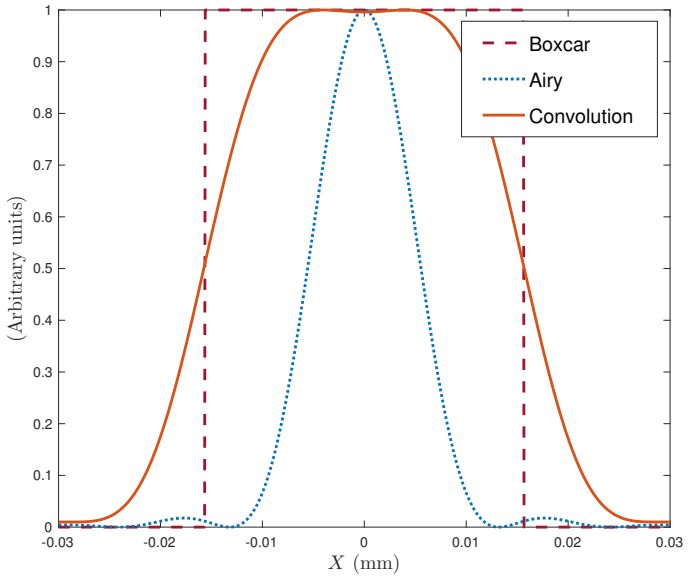

Fig. 5.3 Boxcar function, Airy's function and their convolution. The ratio between the boxcar function width and σ_d is of 0.4.

the presence of patterns and it might recognise some of them even if is they are not present or well defined.

The concept described above, applied in more quantitative fashion, is the basis of our estimate resolution. This investigation was carried out using a ROOT [55] script, which surveys all the elements of each group. The program at first converts the image into a greyscale: this means each pixel content is transformed into a number from 0 (total absence of light, black) to 1 (total presence of light, white). This interval is divided into 256 different intensities (or shadows) [1]. Figure 5.4a shows the 2D pixel intensity colour map for the first element of group 1. The script averages the pixel intensity in each row (excluding an interval of one width from each edge) and plots this value as function of the corresponding row number to get the pixel profile of the element, such as in Figure 5.4b. In Figure 5.4b, the difference between the peak heights are due to local fluctuations in the target illumination. Averaging the pixel contents helps to reduce these effects, but it does not eliminate them entirely.

A quick estimate for the σ_d for the green light with the maximal optical aperture (36 mm) yields to a lower limit for the resolution around 13 μm. The optics, and not camera pixel size, set the minimum possible resolution for this system. Approaching the centre, while the width of the lines of an element and the spacing between them become shorter, while

[1] Number 256 arises from the fact that each pixel is stored with 8 bits.

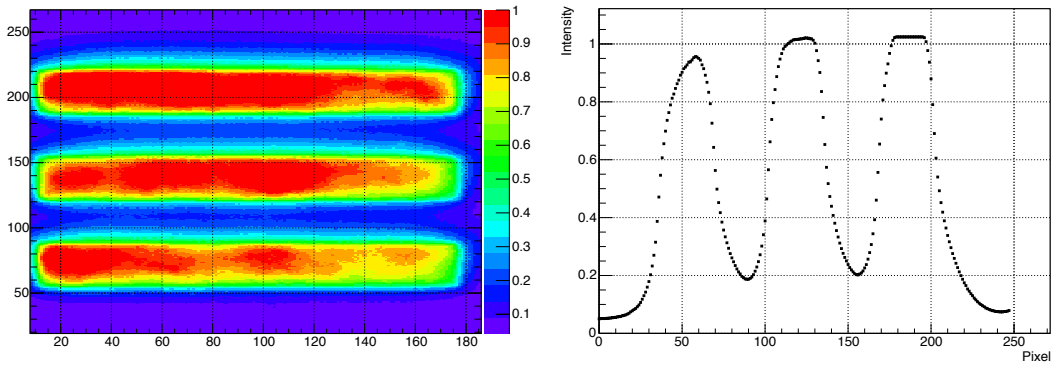

(a) Pixel contents colour map.

(b) Pixel profile.

Fig. 5.4 Pixel contents colour map and intensity profile for the first element of the first group with the green light.

the with of the Airy distribution does not change. The result of the convolution will be now a smoother function, more similar to the Airy distribution than to the boxcar function. As a result of this, we expect the three sharp peaks of Figure 5.4b to flatten out to an almost constant distribution as the spacing between the lines approaches the resolution limit. This will happen close to the first elements of group 5. According to this, we define the contrast K as

$$K = \frac{I_{max} - I_{min}}{I_{max}}, \tag{5.6}$$

with I_{max} and I_{min} respectively the peak and the valley intensities of the pixel profile function. K is close to 1 for well resolved peaks, while it approaches 0 in the resolution limit. We can use the Rayleigh criterion and quantify the limit value of K:

$$K = \frac{I_{max} - 0.81\ I_{max}}{I_{max}} \approx 0.2,$$

where the number 0.81 comes from the ratio between the intensity at the mid-point to that at the maxima for two combined Airy's distributions at the resolution limit [44].

For moving further in the data analysis of the resolution, it is necessary to define a proper fit function, reproducing the periodicity of the image and the position of peaks and valleys and then estimate K from it. The best model would be the physical diffraction pattern. However, a sum of three Gaussians with same spacing, σ and same amplitude may describe the system as well as the Airy's functions and it straightforward to implement in the program. Figure 5.5a and Figure 5.5b show the data fitted with the sum of three Gaussians for two elements, one far from the resolution limit and one close to it. There are systematic dif-

ferences between the model and the data, including the variable illumination of the target. However, the estimate of the contrast is quite accurate. K is worked out from the fitting curve, according to the definition in equation 5.6.

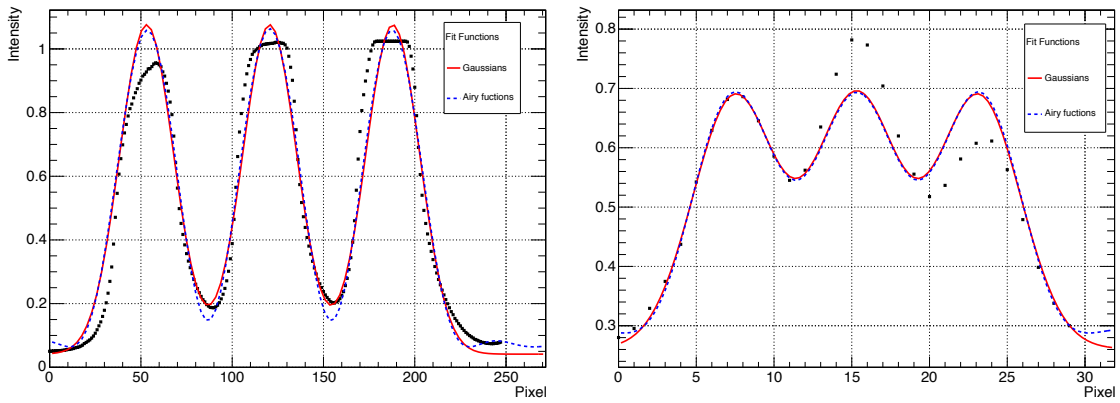

(a) Group 1, element 1, line width: 39 pixels . (b) Group 4, element 1, line width: 6 pixels.

Fig. 5.5 Pixel profile and the fit function for different elements of different group, illuminated with green light and using an aperture of $D = 36$ mm.

5.1.4 Results

The ROOT script can analyse automatically the five elements of each group, returning the contrast K. The dependence of the contrast on the spacing of the elements is displayed in Figure 5.6. The resolution limit can be defined as the region 3-4 pixels (or 18-24 μm), where the contrast becomes smaller than 0.2 and the slope of the curve flattens. The uncertainty on the diffraction limit σ_d is about 15%.

From the fitting function one may also look at the dependence of the Gaussians rms on the spacing (Figure 5.6). Also in this case, one can see a discontinuity around 3-4 pixels.

Knowing the resolution limit, we are interested to show whether the system is diffraction limited (equation 5.5) and if significant aberrations are present. At fist, we measured σ_d for different diaphragm diameters D. The diaphragm is mounted very close to the lens, hence reducing its diameter has the same effect on the system as a smaller lens. Figure 5.7 shows the resolution limit for different apertures, together with the curve of equation 5.5. Uncertainties on the diaphragm aperture come from the measurement with a caliper. The uncertainty on the resolution limit is about 15%. A fairly good agreement is found. The reason for the outlier at 36 mm is not understood.

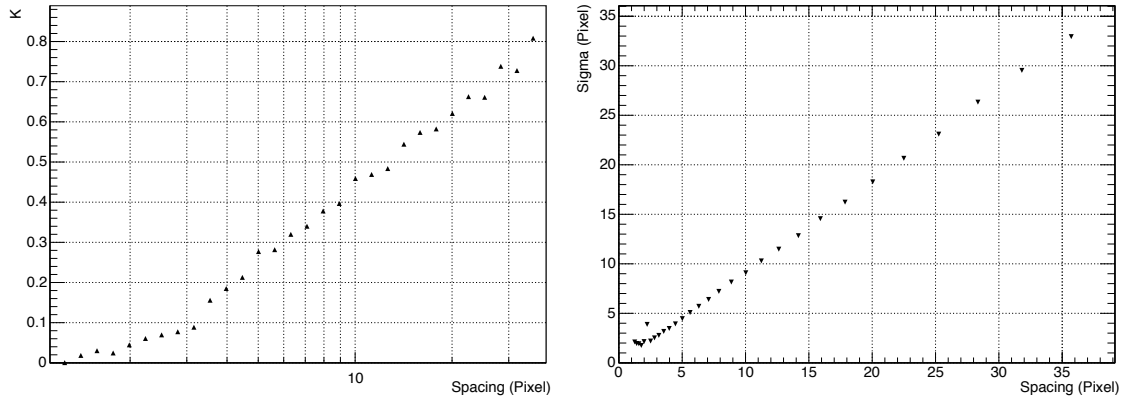

(a) Contrast vs. spacing in log. scale.

(b) Gaussian fit rms vs. line spacing.

Fig. 5.6 Two methods for finding out the resolution limit: plots the contrast curve to the line spacing (1 pixel = 5.86 μm). Elements above 0.2 are considered resolved, according to the Rayleigh criterion. shows the rms of the Gaussian fit to the line spacing. It follows a linear decreasing trend up to the resolution limit and then it becomes constant. Measurements obtained with green light and fully open diaphragm.

Equation 5.5 depends also on the wavelength as well as on the lens diameter. Thus, every optical system has a different resolving power for different colours. Figure 5.8 shows the contrast as function of the spacing for different LED colours. The three colours show a similar trend, but one would expect a better resolution for blue than for red (equation 5.5). This behaviour is not fully understood, but it may be affected by the intensity and homogeneity of the source and by pixel saturation in the camera. In Table 5.1, one may see the expected and measured resolution limits for the different colours.

Table 5.1 shows also the expected number of photons emitted by the LED at each wavelength. The number of photons emitted by the LED per unit of time was estimated as follows. The power consumed by the LED can be worked out from the nominal voltage V_n and current i for each colour. This number is then divided by the photon energy at the wavelength of interest, yielding:

$$N = \eta \frac{V_n i}{\hbar \omega}.$$

η is a factor, which express the overall LED efficiency. Typical efficiency values are around 0.3% and do not differ too much among different colours. At 10 mA, nominal voltages are 2 V for the red light and 3.2 V for the blue and the green light.

Table 5.1 Expected and measured resolution limits, photon fluxes and sensor quantum efficiency for different colours.

colour	σ_d (expected) (μm)	σ_d (measured) (μm)	photons flux ($\times 10^{16}/s$)	quantum efficiency (%)
Red	15.7	17	1.9	50
Green	13.1	23	2.5	62
Blue	11.7	26	2.3	72

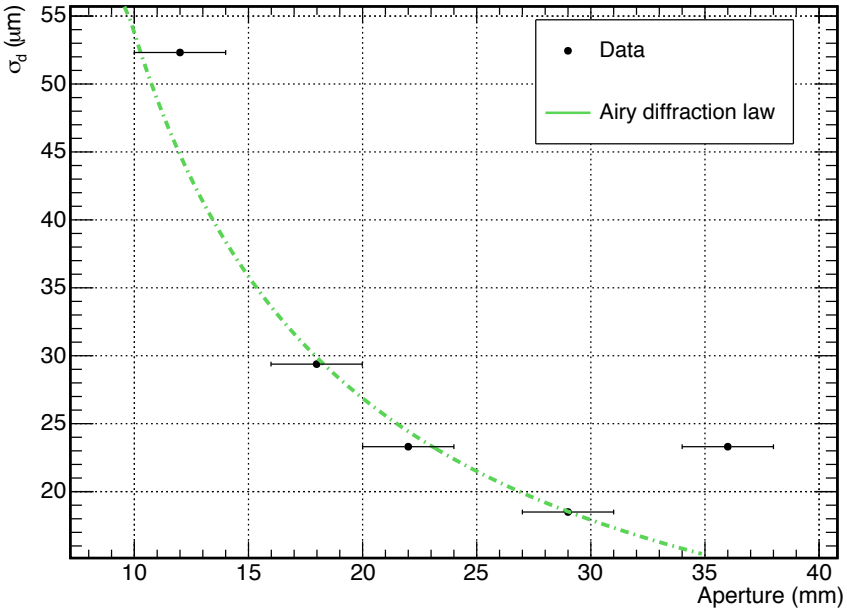

Fig. 5.7 Measured resolution vs. diaphragm aperture for green light. The green line is Airy's law (equation 5.5)

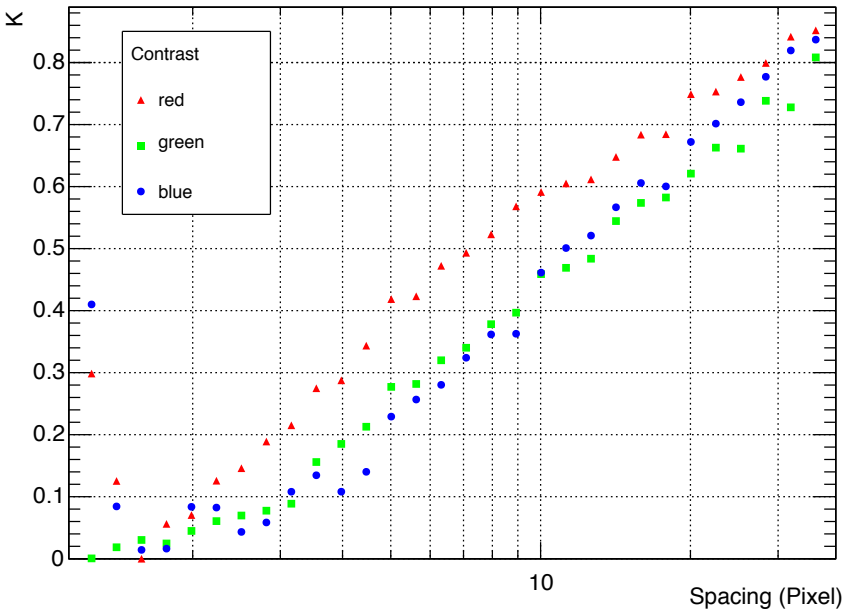

Fig. 5.8 Contrast factor K vs. spacing for the red, green, and blue LEDs.

5.2 The automatic centring software

This part is dedicated to the software used to adjust the image position and focus. These automatic corrections are necessary to keep the image quality constant in time and for different experiments, even if small fluctuations in the emission point of synchrotron-light occur.

Despite the poor repeatability of the picmomotors, writing a software that leads the image of the beam to the centre of the screen, does not present any issue. A camera feedback of the actual movement is always present, hence the software has continuous information on the real position of the beam in the image. The shot information is analysed by *BPMSoftwareHard* and then sent to *BPMCommunication*. This reads the x and y position with respect to a reference frame fixed on the centre of the screen. As the software is aware of the initial position of the beam, it notifies ACNET to move the picomotors of number of steps equal to $\pm 3000 \cdot x^2$ for both the horizontal and vertical positions[2]. The direction of the movement is determined by the sign of x or y: a negative sign is a right or up movement, while a positive is a left or down movement. After accomplishing this movement, the software reads the new positions and requests the new number of steps. The beam is centred when x and y are less

[2]These parameters are chosen to increase the speed of the procedure. The smallest number of steps is 1000.

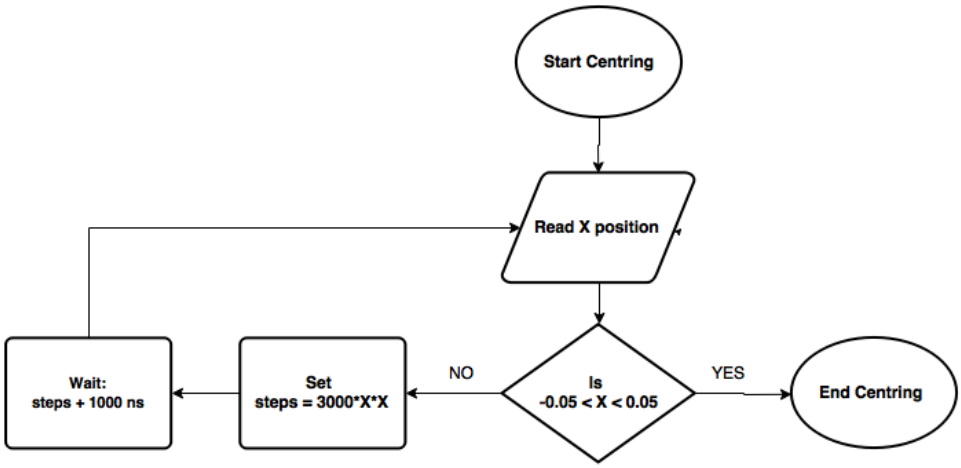

Fig. 5.9 Block diagram for the beam centring algorithm on the x direction. The same block diagram is valid also along the y direction.

than 0.5 mm. The block diagram is displayed in Figure 5.9 and commented lines can be found in Appendix B.

A test of this software was made using a small spot of light moving on a screen as in the picomotor repeatability experiment. The program could reliably move the spot of light from one edge of the screen to the center in about one minute.

5.3 Automatic focusing

5.3.1 Common autofocusing techniques

Automatised focusing systems are widely present on many cameras and cell-phones, and several algorithms find application on many fields. Most of them have been optimised for being fast and solid, but they often rely on the knowledge of the absolute position of the image plane.

We saw that the picomotors repeatability does not hinder a centring program. However, it may limit the possible strategies for implementing an automatic adjustment of focus.

One of the most common autofocusing techniques is called Contrast detection and it works with an open loop configuration [56]. This method is based on the idea of moving a lens (or a camera in our case) until the intensity or its gradient reaches a maximum, meaning that moving the lens forward or backward would decrease the intensity in a pixel or the gradient in a small neighbourhood. This local maximum is the position of best focus. However, this maximum-seeking method is strongly dependent on the fluctuations of the quantity to maximise.

5.3.2 Behaviour of a Gaussian distribution around the focal point

A maximum (or minimum) seeking method similar to contrast detection may be optimised for applications in IOTA. Using the default outputs from *BPMServerHard*, quantities which can be optimised are the two transverse sizes and the amplitude of the distribution. Before implementing any algorithm, we want to study how these quantities change as the camera is moved away from the focal point.

In Chapter 4, *BPMServerHard* interpolates the pixel contents with a 2-dimensional Gaussian function. For simulating the expected image of a beam in IOTA, a Gaussian shape was printed on cardboard screen and illuminated with green light. A survey on how the image of the Gaussian target changes along the travel range of the movable stage was made at 40 position, in intervals of 50,000 steps (about 1.5 mm) distant form each other. At each position a set of ten measures was taken as well as a picture of the target. In Figure 5.10 one may see two pictures of the target in different positions along the focusing curve: far from the focus (5.10b) and close to it (5.10a).

Using the data gathered with the survey, the focusing curve was built plotting the vertical size, the horizontal size or the amplitude vs. the image number (examples in Figure 5.11). Close to the focal point, we expect a minimum for the sizes and a maximum for the amplitude. For the amplitude (Figure 5.11b) we can recognise a peak close to the focal point. On the contrary, the focal curves of the transverse sizes are not as smooth as expected and they are subject of many fluctuations close to the focal point (Figure 5.11a). This behaviour is due to imperfections in the target. As one may notice, Figure 5.10a is sharpener than Figure 5.10b and details on the paper texture are well recognisable. This alters the fit of *BPMServerHard*, which assumes a Gaussian distribution.

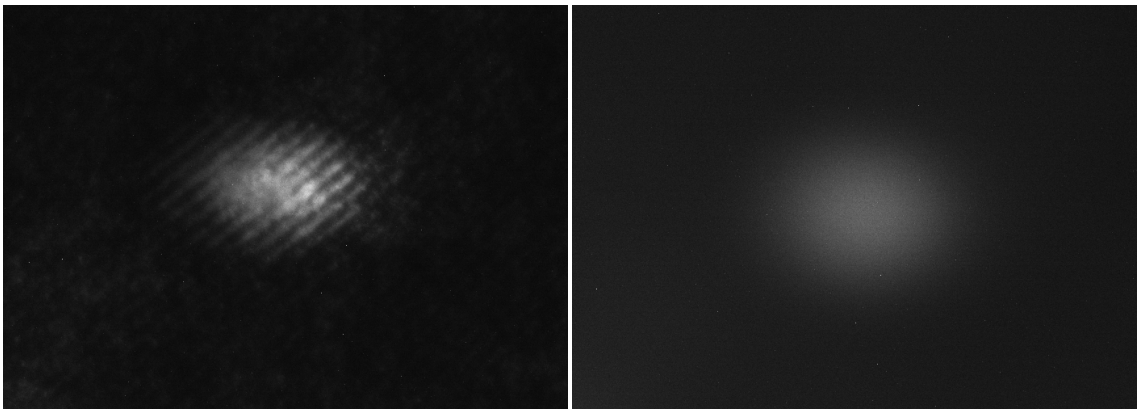

(a) In focus. (b) Out of focus.

Fig. 5.10 Image of the Gaussian target close and far from the focal point.

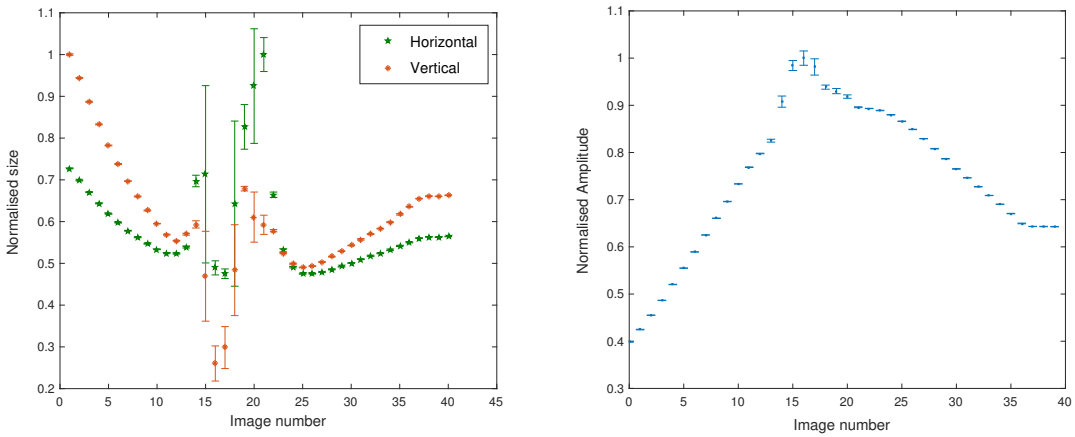

(a) Cross sections. (b) Amplitude.

Fig. 5.11 Curve of focus of the cross section and of the amplitude. The error bars are the standard deviation of the ten values.

5.3.3 The autofocusing software

A system of focus self-adjustment can be implemented using a maximum-seeking algorithm for a quantity which shows a sharp maximum close to the focal point. After the study of the curve of focus in Section 5.3.3, the amplitude has been identified as the best quantity for a maximum-seek algorithm.

This algorithm has been implemented within the software *BPMCommuniation*. The logic is highlighted in the block diagram of Figure 5.12 and more detailed explanations of the lines of code are in Appendix B. At the beginning, the program reads the mean of a set of ten amplitudes from *BPMServerHard*, and then it calculates again the mean of ten amplitude measures in a new position 50,000 steps further. The old and the new values are compared: if their difference is lower than 0 the camera is on the right of the focus, and vice-versa. Once the program is aware of the position of the camera, the picomotor is set for advancing towards the focus of 50,000 steps. After that, new values of the amplitude are read and compared with the previous ones. As long as the sign of the difference between the new and the old measures is the same, the movement of 50,000 steps is performed in the same direction. When the sign difference is found opposite, the number of steps is reduced by 10,000 and the direction is reversed. The software stops when the number of steps is equal to 0.

Some test were made in the same condition and with the same target used for building the curves of focus. This method succeeded in focusing the image within an error lower than 10 mm (out of a surveyed arm of 100 mm) from the expected focal point. This result can be

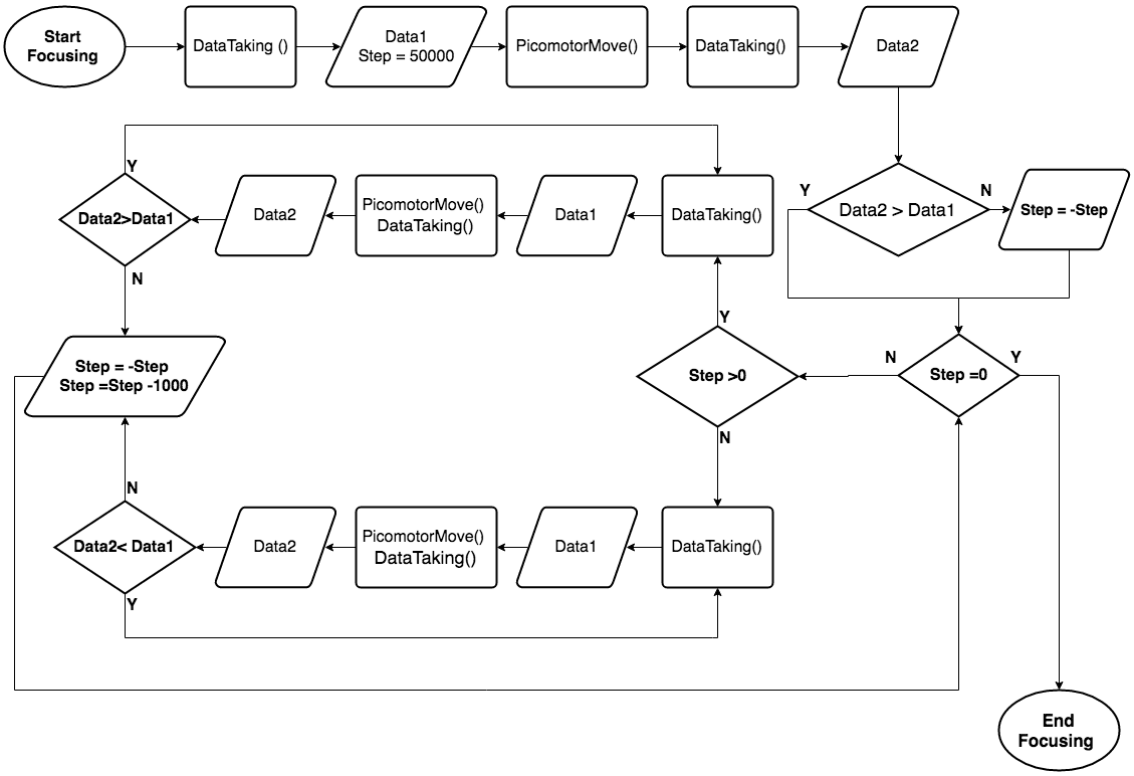

Fig. 5.12 Block diagram for the beam focusing algorithm. *DataTaking()* and *Movepicomotors()* are both subroutines; the former takes a set of ten data point and calculates their average, while the latter moves the picomotors by a selected number of steps and puts the program on hold until the movement is performed.

interpreted only as a proof of feasibility for an automatic focusing software in an open loop configuration for a Gaussian like distribution. However, the focusing curve is valid only for stable conditions of illumination, gain and shutter speed. Moreover, the autofocusing works only for movements of many steps, because fluctuation becomes unimportant at large shifts. The latter aspect strongly limits the precision of the algorithm in finding the focal point. For this reason, in the following section we propose more robust quantities which behave smoothly around the focus and which may be more safely maximised than the amplitude.

5.3.4 Robust automatic focusing strategies

Fluctuations in the objective function are an issue for optimisation algorithms. An autofocusing system requires smoothly varying quantities to maximise or minimise. Reducing fluctuations allows one to take smaller steps and to improve the precision of the algorithm. Here, we investigate methods that use all the information contained in each image and that are more robust and model independent.

The variance of the pixel intensity could be a suitable quantity for a maximum-seek algorithm. Well focused images show more intensity levels, hence the variance is larger. On the other hand, in poorly focused images, the pixels tends to have the same intensity level, thus reducing the variance. Figure 5.13a displays the curve of focus of the variance for a set of 31 test images.

A second method treats the image as a 2-dimensional probability distribution and defines the information content (or negative entropy) according to Shannon's information entropy [57]. (This approach is different from a commonly used one, which considers the information entropy of the intensity histogram). If there are n pixels and I_i is the i-th pixel intensity, the probabilities are defined as $p_i = I_i / \sum I_i$. The maximum information entropy is $S_{max} = \log_2 n$, corresponding to a constant distribution. The normalised information content is defined as the negative of the normalised information entropy:

$$S = \frac{1}{S_{max}} \sum_{i=1}^{n} p_i \log_2 p_i.$$

Images with low information content have many pixels with values close to the average level. Images with high contrast and details have high information content. As an example, the variation of the information content (a negative quantity) around the focus for the 31 test images is shown in Figure 5.13b

A third method considers the autocorrelation function of the pixel intensity profile of the image. The autocorrelation [58] function is common in signal analysis for detecting non-

randomness in data. It is the correlation of a function with itself after a given shift (or time lag). In the case of image analysis, the signal is given by the concatenated rows or columns of the image intensities. The autocorrelation is larger for a smooth, defocused image, while it is smaller for sharp patterns with many different intensity levels. The autocorrelation is greater for a random noise, while is smaller for periodic patterns. The changes around the focus of an autocorrelation function averaged over many time lags are shown in Figure 5.13c.

All the images of 5.13 displays a clear peak (or a valley) at the image 16, a result which is consistent with a visual comparison between all test images. All the three methods succeed in finding the focus. Although further tests are needed, these methods are more robust, in the sense that they do not depend on the shape of the image and that the figure of merit for optimisation exhibits small fluctuations. For this set of images, the autocorrelation gives the sharpest minimum.

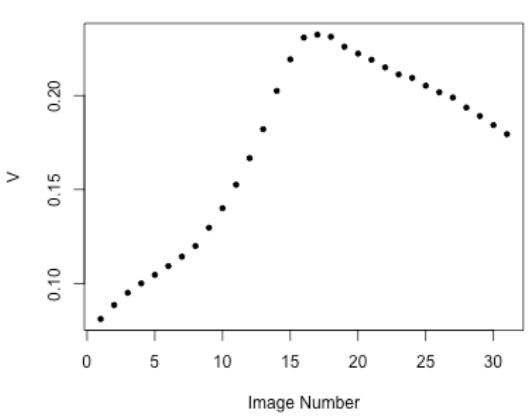

(a) Normalised Variance.

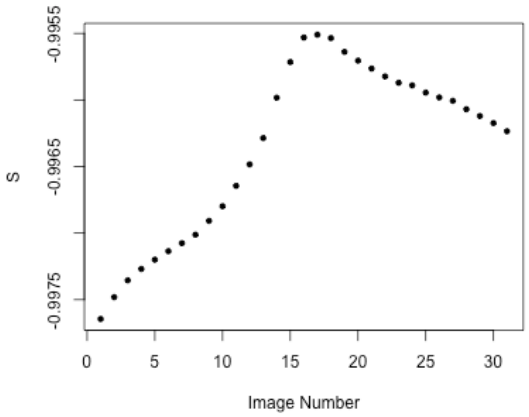

(b) Normalised information content.

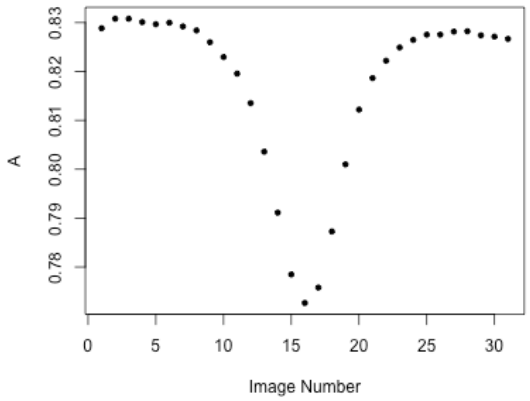

(c) Autocorrelation.

Fig. 5.13 Focusing curve for variance, information content, and autocorrelation vs. image number. These images covered a span of 50 mm around the focus plane.

Conclusions

The main scope of this thesis was the study and the development of a beam monitor based on synchrotron radiation for the Fermilab Integrable Optics Test Accelerator. Such beam monitors measure intensity and position of the beam in a way that is complementary to beam position monitors based upon electromagnetic pickups. The synchrotron-light monitors are also the main devices responsible for measuring the transverse cross section of the beam (which, in a linear lattice, is directly related to the amplitude or beta function). A precise knowledge of the beam position, size and intensity, and their evolution over time, is essential for the nonlinear integrable optics experiments, for the demonstration of optical stochastic cooling, and for experiments with a very low number of stored electrons in the machine.

Resolution is the key parameter of the synchrotron light beam monitor and it depends on the imaging formation process and on the presence of aberrations due to imperfection in the optics. Significant part of this work aimed at estimating the resolution of the beam monitors. We carried out a theoretical estimates of the resolution and we identified the main contributions: diffraction and depth of field. Using a simulation, we were able to find out an optimal optical acceptance which maximises the resolution. The study of the resolution and the presence of aberrations was carried out also from an experimental point of view in a prototype of the beam monitor based on a realistic layout. The dimensions of the prototype were chosen to meet all the constrains, such as vacuum chamber length, height of the dipole, magnification coefficient, and position of the lens, etc...

The prototype was used also to test two image self-adjustment systems, which are fundamental in IOTA for keeping a good image quality among the experiments, when position fluctuations of the synchrotron light emission point are expected to occur.

The main accomplishments of this work are listed below.

- The theoretical imaging formation analysis was performed on typical beam sizes that are larger than the diffraction limit. An estimation of the systematic error from diffraction and depth of field was given for different optical acceptances and an optimal aperture at which the two contributions are minimal was found. This analysis was at first performed on a standard IOTA beam size $\sigma \gg \sigma_d$ and then repeated for some critical

beam transverse dimensions $\sigma \geq \sigma_d$. Systematics are in general a 20% contribution to the total beam cross sections. Further studies for special cases with very small beam sizes will be needed.

- A realistic layout of a beam monitor and its dimensions were proposed based on the design of the dipoles and the requirements of the experiments. A table top prototype was built with with a 400 mm focal lens and a magnification of 0.873. The prototype includes two mirrors and a movable stage with a camera sensor. In view of a remote self-adjustment of the image, three picomotors were mounted: two of them on a mirror, and a third on the stage. Software for processing the camera readout and for remote control the picomotors was implemented.

- In view of the use of picomotors for image centring and focusing adjustments, a repeatability test was carried out. The results highlighted poor repeatability. Mitigation strategies were suggested, but their inclusion in the final design is discouraged.

- The image formation in the prototype was investigated using an LED and the resolution was measured according to the Rayleigh criterium for different acceptances and wavelengths (blue, green, red). The result is in agreement with the expected dependence on aperture. The wavelength dependence could not be verified due to systematics.

- Algorithms for automatic image centring and focusing were proposed and implemented. Using a Gaussian image, we tested the centring algorithm and we proved the feasibility of the automatic focus based on an amplitude maximisation algorithm. Fluctuations of the maximum amplitude may be an issue. The possibility of maximising robust quantities, such as variance, entropy and autocorrelation of the image, was put forward, and implemented on a set of images.

This thesis provided important inputs for the final design of the IOTA synchrotron-light beam monitors. In addition, it contains a theoretical overview of synchrotron-light detection in accelerators, including the effects of depth of field on the emission arc, which are seldom described systematically in the literature.

A deep understanding of this kind of detector will help to enable a new class of experiments in nonlinear beam dynamics, on optical stochastic cooling, and on the quantum behaviour of single electrons in a storage ring.

Appendix A

Blueprints of the dipoles

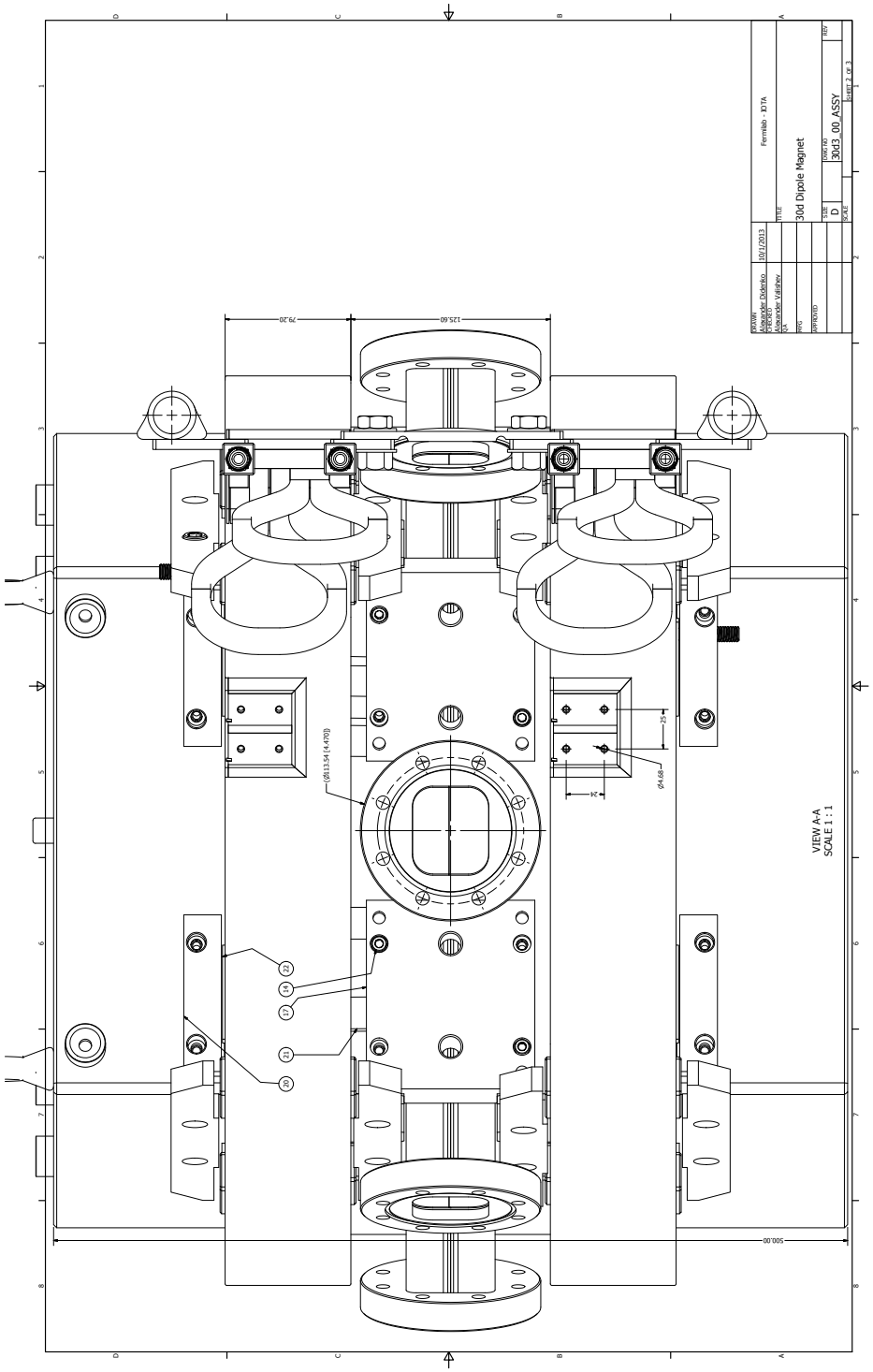

Fig. A.1 30° dipole front view.

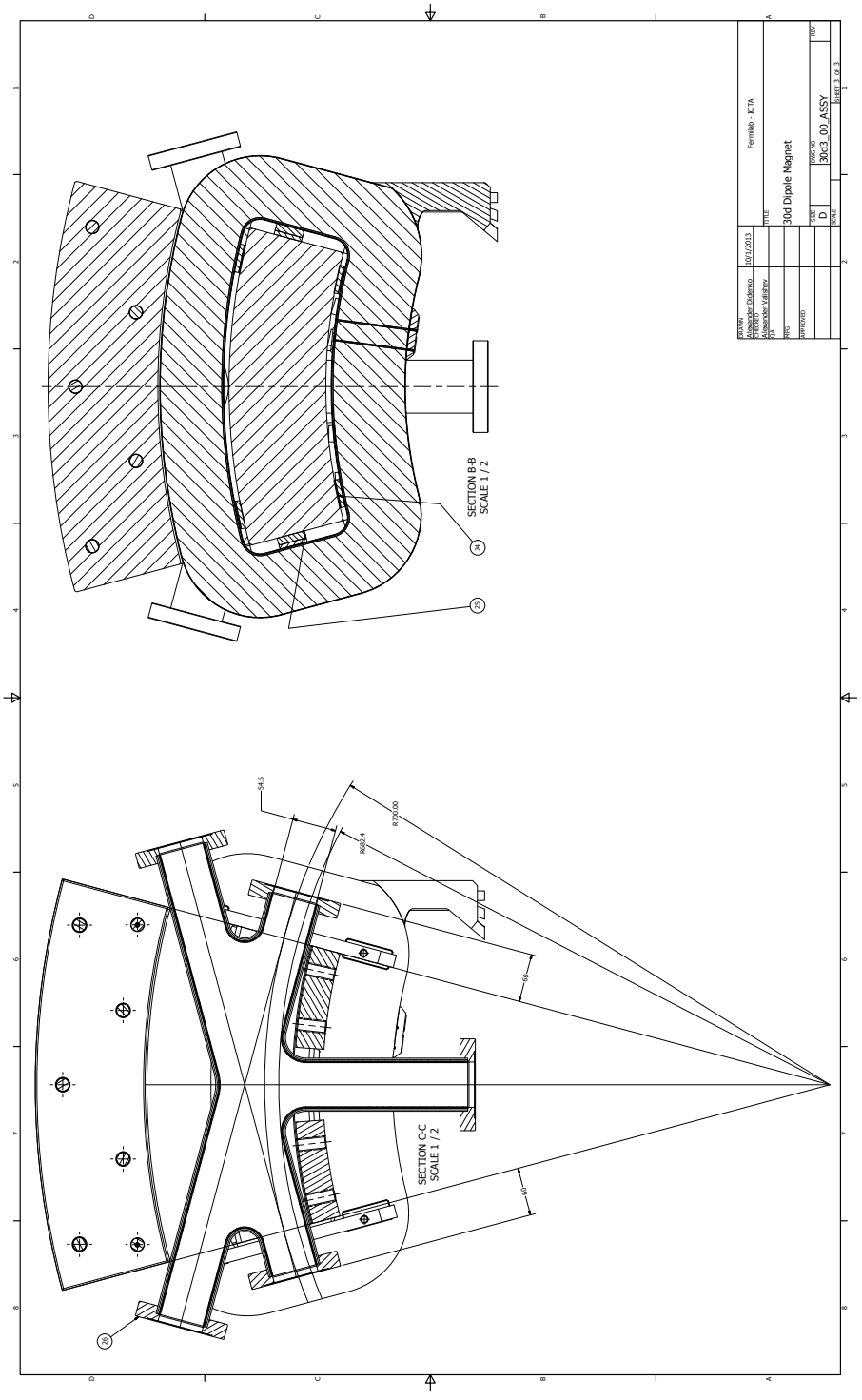

Fig. A.2 30° dipole inner view.

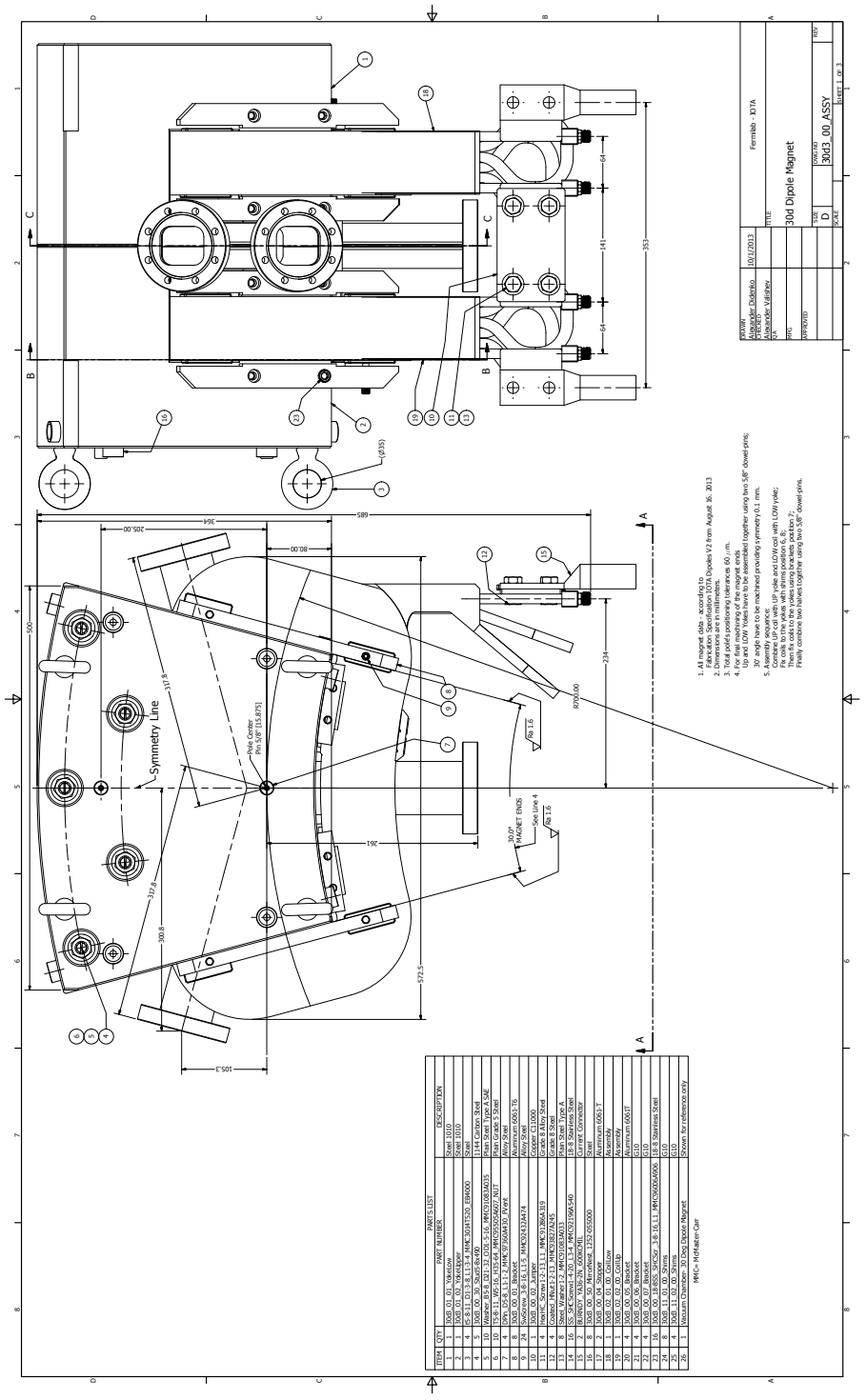

Fig. A.3 30° dipole up and side view.

Appendix B

Scripts

In Chapter 5, we give a brief overview on the logic behind the self-adjustment algorithms and we display their logic. However, a glimpse of the main scripts composing the program is needed for better understanding their implementation.

Both algorithms are written in Java and are part of a more complex software, *BPMCommunication*, which manages the connection between *BPMSeverCommon* and ACNET. In this appendix we will highlight only the codes related to the focusing and centring algorithms and how they are interfaced with the rest of the software.

Java works differently compared to other popular languages. In fact, a Java program is built as a series of blocks called classes, and each class can contain one or more methods. Methods are just a set of instructions and they can have and argument and a return value (as for functions and subroutines in C++). One may call classes and methods within other classes or methods. In Java, a class may be promoted to Thread. In computer science, a Thread is a small set of instructions, which can be executed in parallel to the main software. For our software, we created a program based on two Threads: the fist is the main program, which executes all the components of the Graphical User Interface (GUI), the centring and focusing instructions. The second, is a class called `newControl`, which handles the connection to the Server and receives the shots from the camera.

When the program is running, a simple window (Figure B.1) allows selecting a beam monitor as well as some operations to perform. The users can choose the monitor by typing its name in text field (1). The text fields and the buttons within box (2) allows to control the positioners one by one and to set a custom number of step for each of them. The positioners are sorted by name and number: ISMM1 and ISMM2 control the mirrors, while ISMM3 moves the stage. The steps selected in the text fields are sent directly to ACNET, hence the positioners can be moved even if the program is disconnected from any beam monitor. This obviously must be revised when more beam monitors will be added.

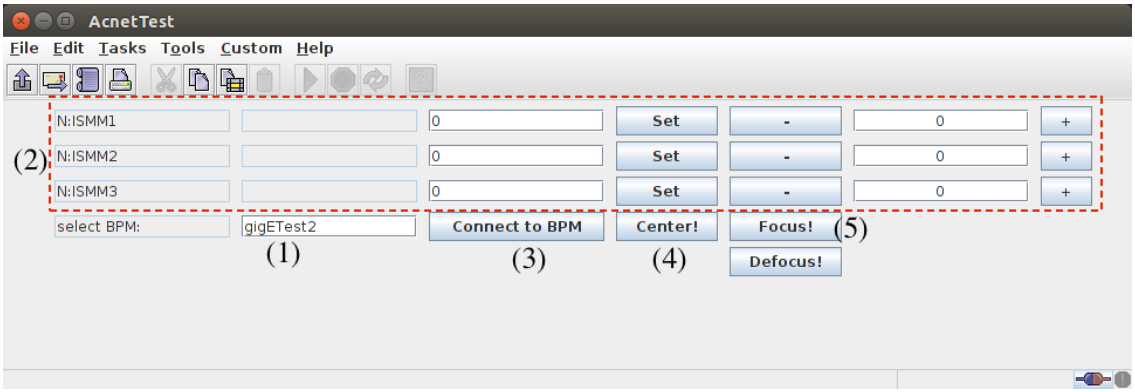

Fig. B.1 The *BPMCommunication* Graphic User Interface.

Three more buttons handles three different aspect of the program: *Connect to BPM* (3), as suggested by the name, handles the connections with the Server and the shot received; *Center* (4) stats the centring procedure for the selected monitor, while *Focus* (5) carries on the focusing operations. A detailed description of the operations triggered by the three buttons is given in the following sections.

B.1 Connection manager

The button *Connect to BPM* runs the Thread `newControl`, which contains the method `connection()`. This is probably the more complicate part of the program: `connection()` talks to the Server through the *Server listeners*, specific Java classes, designed to wait for an input from the Server before performing any operation. The communication between the Server and *BPM-Communication* is established using the protocol TCP/IP. The *Server listeners* are included as methods of the `CommonBPMServerCommunicator` class (not described here). The lines below show the `newControl()` Thread.

```
public void newControl(){
    start();
}
@Override
public void run() {
    connection();
}
public void connection(){
    try{
        CommonBPMServerCommunicator.getInstance().addCommonBPMServerListener(this);
        CommonBPMServerCommunicator.getInstance().getAvailableBPMs();
```

```
        }catch (IOException e){
            e.printStackTrace();
        }
    }
```

The *Server listeners* are three: `messageFromServerReceived`, `shotFromServerReceived` and `connectionStatusChanged`. The former receive the list of the available beam monitors and store them into a list called `realNames`:

```
    @Override
    public void messageFromServerReceived(String message) {

        realNames = new LinkedList<String>();
        String m = message;
        String[] mPartArr;
        m = message.substring(1, message.length()-1);

        String[] sArr = m.split(";");

        for(String s:sArr){

            mPartArr = s.split(":");

            if(mPartArr[0].equals("AvailableBPMs")){
                for (int i=1; i<mPartArr.length; i++) {

                    realNames.add(mPartArr[i]);
                }
            }
        }
        requestFrames(setBPM(new MainPanel().getName()));
    }
```

The code is rather complicate, since it has to format the string received from the message and sort the beam monitors names into the list. The latter method, `requestFrames(setBPM(new MainPanel().getName()))`, requests frames for a single beam monitor, selected by comparing the names in `realNames` with the name written in the GUI textfield (1).

As soon as the frame query is sent to the server, the incoming informations are handled by the second *Server listener*: `shotFromServerReceived`.

```
private LinkedBlockingQueue<BPMShotInfo> = shotBuffer;
shotBuffer = new LinkedBlockingQueue<>();
```

```
@Override
public void shotFromServerReceived(BPMShotInfo shotInfo) {

       if (!isSleep) {
          shotBuffer.add(shotInfo);
       } else {
          //Dump shot
       }
}
```

The data from the Server come into the variable `shotInfo`. If the boolean variable `isSleep` is not true, `shotInfo` is dumped, otherwise `shotInfo` is added to `shotBuffer`, a special list where data are stored waiting for a call by any method.

The third *Server listener* handles any connection status changes. At this stage, it does not perform any action. A safe disconnection system from the Beam Monitor or from the Server must be implemented

B.2 Centring

When the button centring is pressed, a centring algorithm is started:

```
public void centering(){
  isStop = false;
  while(!isStop) {
        isSleep = false;
        try {
            centerX(shotBuffer.take().getXInCM());
            centerY(shotBuffer.take().getYInCM());
       } catch (InterruptedException e) {
             e.printStackTrace();
       }
       centeringStop(isXCentered, isYCentered);
  }
}
public void centerX(float x){
    int step = (int) (3000*x*x);
    if(step <1000){step = 1000;}
    if(x>0.05){
        MyACNETControl.getInstance().setChanel("N_ISMM1", step);
    }
    if(x<-0.05){
```

```
            MyACNETControl.getInstance().setChanel("N_ISMM1", -step);
        }else{
            isXCentered = true;
        }
        isSleep = true;
        try {
            Thread.sleep(step+1000);
        } catch (InterruptedException e) {
            e.printStackTrace();
        }
        isSleep = false;
        shotBuffer.clear();
    }
    public void centerY(float y){
        int step = (int) (3000*y*y);
        if(step <1000){step = 1000;}
        if(y>0.05){
            MyACNETControl.getInstance().setChanel("N_ISMM2", +step);
        }
        if(y<-0.05){
            MyACNETControl.getInstance().setChanel("N_ISMM2", -step);
        }else{isYCentered = true;}
        isSleep = true;
        try {
            Thread.sleep(step+1000);
        } catch (InterruptedException e) {
            e.printStackTrace();
        }
        isSleep = false;
        shotBuffer.clear();
    }
    public void centeringStop(boolean isXCentered, boolean isYCentered) {
        if(isXCentered == true && isYCentered == true)
        isStop = true;
        System.out.println("Centered!");
    }
```

Fist of all `isSleep` is set to true, in this way data are stored into `shotBuffer`. `centering()` read the x and y position from the `shotBuffer` and set them as argument for the functions `centerX()` and `centerY()`. These two functions decide if the position is lower than 0.5 mm and if not they set for picomotors a number of steps equal to $3000 \cdot x^2$ or $3000 \cdot y^2$. For efficiency issues, the minimum number of step is limited to 1000. The steps are sent to the picomotor through the class `MyACNETControl`: this class converts the java instructions

into ACNET instructions. `MyACNETControl` was made by Fermilab Accelerator Controls Department and it was simply added to the software, with little modifications. While a picomotor is moving, the main Thread is stopped for an amount of time proportional to the number of steps performed; `isSleep` is temporary set back true in order to dump the shots. The software is "blind" while the picomotors are moving.

The action of `centerX()` and `centerY()` is iterated until the centring condition is fulfilled. At this point the flag variables `isXCentered` and `isYCentered` are set true and the function `centeringStop` puts an end to `centering()`

B.3 Focusing

Pressing *Focus* starts the autofocusing algorithm.

```
public void focusing() {
    int step = 50000;
    int time = 30000;
    double data1;
    double data2;
    isStop = false;

    while (!isStop) {
        isSleep = false;
        data1 = takingData(shotBuffer);
        movePicomotor(step);
        data2 = takingData(shotBuffer);
        if (data1 > data2) {
            step = -step;
        }
        System.out.println("end of startingBlock");

        while (!isFocused) {
            if (step > 0) {
                data1 = takingData(shotBuffer);
                movePicomotor(step);
                data2 = takingData(shotBuffer);
                if (data2 < data1) {
                    step = step - 10000;
                    step = -step;
                } else {
                    isFocused = false;
                }
```

```
            }
            if (step < 0) {
                data1 = takingData(shotBuffer);
                movePicomotor(step);
                data2 = takingData(shotBuffer);
                if (data2 > data1) {
                    step = step + 10000;
                    step = -step;
                } else {
                    isFocused = false;
                }
            }
            if (step == 0) {
                isFocused = true;
            }
        }
        focusingStop(isFocused);
    }
}
```

In the first part the program attempts to understand the position of the camera to the focal point: it measures the amplitude in two different points 50000 steps distant one from the other using the function `takingData`, which read ten amplitudes from `shotBuffer` and return the mean of them. The code is almost self-explanatory.

```
public double takingData(LinkedBlockingQueue<BPMShotInfo> shotBuffer){
    int step = 50000;
    int time = 30000;
    shotBuffer.clear();
    for(int j=0; j<10; j++) {
        try {
            statsAmplitude.addValue(shotBuffer.take().getMaxAmplitude());
        } catch (InterruptedException e) {
            e.printStackTrace();
        }
    }
    double Amplitude = statsAmplitude.getMean();
    statsAmplitude.clear();
    shotBuffer.clear();
    return Amplitude;
}
```

The sign of the difference between the two data taken determines the position: assuming no fluctuations, if the sing is positive, then the focal point is in front to the camera. According

to this first analysis the direction of the movement is then set. Positive steps moves the camera forward, while negative steps moves it backward. While the picomotors are running, theThread is sleeping and the shots received are dumped. The function `movePicomotor` handles this.

```
public void movePicomotor(int step){
    int time = 30000;
    MyACNETControl.getInstance().setChanel("N_ISMM3", step);
    try {
        isSleep = true;
        Thread.sleep(time);
        isSleep = false;
        shotBuffer.clear();
    } catch (InterruptedException e) {
        e.printStackTrace();
    }
}
```

After the initial block, the real algorithm begins. Two more amplitudes are measured at 5,000 steps of distance one from the other, and the sign of their difference is calculated. While the sign remains the same, the direction of the motion does not chance; however, when the sign is found to be opposite of the previous, the direction is reversed and the number of steps is diminished of 10,000. When the number of steps is equal to 0, the method `focusingStop` stops the algorithm, setting true the variable `isStop`.

References

[1] High Energy Physics Advisory Panel (HEPAP). http://science.energy.gov/hep/hepap/reports/, 2013.

[2] R. Acciarri, M. A. Acero, and M. Adamowski et al. (741 additional authors not shown). Long-Baseline Neutrino Facility (LBNF) and Deep Underground Neutrino Experiment (DUNE) Conceptual Design Report Volume 1: The LBNF and DUNE Projects. 01 2016. URL https://arxiv.org/abs/1601.05471.

[3] J. Grange et al. Muon (g-2) Technical Design Report. 2015.

[4] L. Morescalchi. The Mu2e Experiment at Fermilab. 2016. URL http://inspirehep.net/record/1485570/files/arXiv:1609.02021.pdf.

[5] S. Holmes et al. PIP-II STATUS AND STRATEGY. In *Proceedings, 6th International Particle Accelerator Conference (IPAC 2015): Richmond, Virginia, USA, May 3-8, 2015*, page THPF116, 2015".

[6] M. Church et al. Proposal for an Accelerator R&D User Facility at Fermilab's Advanced Superconducting Test Accelerator (ASTA). 2013.

[7] P. Piot et al. The Advanced Superconducting Test Accelerator (ASTA) at Fermilab: A User-Driven Facility Dedicated to Accelerator Science & Technology. In *Proceedings, Community Summer Study 2013: Snowmass on the Mississippi (CSS2013): Minneapolis, MN, USA, July 29-August 6, 2013*, 2013.

[8] A. Valishev. IOTA - A brief parametric profile. In *Focused Workshop on Scientific Opportunities in IOTA*, April 2015.

[9] E.D. Courant and H. S. Snyder. Theory of the alternating-gradient synchrotron. *Annals of Physics*, (3):1–48, 1950.

[10] G. Kafka. Lattice Design of the Integrable Optics Test Accelerator and Optical Stochastic Cooling experimentat Fermilab. Master's thesis, Illinois Institute of Technology, 2015.

[11] Concepts Rookie Book. Accelerators Control Division: http://beamdocs.fnal.gov/AD/DocDB/0044/004444/002/concepts.pdf, December 2013.

[12] A. Hoffman. *The Physics of Synchtrotron Radiation*. Cambridge University Press, 2004.

[13] *An Introduction to Stochastic Cooling*, volume 153, N.Y. 1987. Amer. Inst of Phys. (AIP).

[14] E. McMillan. A problem in the stabiliy of periodic sytems. In *Topics in Modern Physics (A Tribute to E.U. Condon)*, page 219. Colorado Assoc. University press, 1971.

[15] V. Danilov and S. Nagaitsev. Nonlinear accelerator lattices with one and two analytic invariants. *Phys. Rev. ST Accel. Beams*, 13:084002, 2010.

[16] S. Nagaitsev, A. Valishev, V.V. Danilov, and D.N. Shatilov. Beam Physics of Integrable Optics Test Accelerator at Fermilab. 01 2013. URL https://arxiv.org/abs/1301.6671.

[17] A. Valishev, S. Nagaitsev, V. Kashikhin, and V. Danilov. Ring for test of nonlinear integrable optics. *Conf. Proc.*, C110328:1606–1608, 2011.

[18] V. Shiltsev. *Electron Lenses for Super-Colliders*. Springer, 2015.

[19] G. Stancari, K. Carlson, M. W. McGee, L. E. Nobrega, A. L. Romanov, J. Ruan, A. Valishev, and D. Noll. Electron Lenses for Experiments on Nonlinear Dynamics with Wide Stable Tune Spreads in the Fermilab Integrable Optics Test Accelerator. In *Proceedings, 6th International Particle Accelerator Conference (IPAC 2015): Richmond, Virginia, USA, May 3-8, 2015*, page MOBC3, 2015. URL http://lss.fnal.gov/archive/2015/conf/fermilab-conf-15-136-ad-apc.pdf.

[20] V. A. Lebedev. Test of Optical Stochastic Cooling in the IOTA ring. In *1st North American Particle Accelerator Conference 2013*, 2013.

[21] Aleshaev A. et al. A Study of influence of synchrotron radiation quantum fluctuations on the synchrotron oscillations of a single electron using undulator radiation. *Nucl. Instrum. Meth.*, A359:80, 1995.

[22] Pinaev I. et al. Experiments with undulator radiation of a single electron. *BUDKER-INP-1993-73*, 1993.

[23] R. Dixon. Transfigured electron double slit experiment. https://indico.fnal.gov/getFile.py/access?contribId=23&resId=0&materialId=slides&confId=11852, June 2016.

[24] W. Wei et al. Study of exotic ions in superfluid helium and the possible fission of the electron wave function. *J Low Temp Phys*, 78(178):117, 2015.

[25] A. Romanov et al. Lattice correction modeling for Fermilab IOTA ring. In *Proceedings, 5th International Particle Accelerator Conference (IPAC 2014): Dresden, Germany, June 15-20, 2014*, page TUPRO058, 2014.

[26] D. Ivanenko and I. Pomeranchuk. On the maximal energy obtainable in a betatron. *Physical Review*, 65:343, May 1944.

[27] F.R. Elder et al. Radiation from electrons in a synchrotron. *Physical Review*, 71(11): 829–830, May 1947.

[28] J. Schwinger. On the classical radiation of accelerated electron. *Physical Review*, 75 (12):1912–1925, June 1949.

[29] Lightsources around the world. lightsources.org :http://www.lightsources.org/regions, 2016.

[30] H. Koziol. Beam diagnostics for accelerators. *CERN Accelerator School: Basic course on accelerator physics*, page pp. 151, October 2005.

[31] R. Thurman-Keup et al. Synchrotron radiation based beam diagnostics at the Fermilab Tevatron. *JINST*, 6:T09003, 2011.

[32] R. Maccaferri et al. The 5T superconducting undulator for the LHC synchrotorn radiation profile monitor. *Proceedings of EPAC, Lucerne, Switzerland*, 2004.

[33] H. Wiedemann. *Particle Accelerator physics*. Springer, 2007.

[34] S.Y. Lee. *Accelerator physics*. World scientific, 1999.

[35] R.P. Walker. Synchrotron radiation. *CAS - CERN Accelerator School: 5th General accelerator physics course, CERN 94-01, Vol.1*, 1, 1994.

[36] A. Hoffman. Characteristics of synchrotron radiation. *Nucl. Instr. and Meth.*, (203): 483, 1982.

[37] J.D. Jackson. *Classical Electrodynamics*. Wiley, 1962.

[38] R. Coisson. Angular-spectral distribution and polarisation of synchtrotron radiation from a "short" magnet. *Physical Review*, 20(2):524–528, August 1979.

[39] R. Bossart et al. Observation of visible synchrotron radiation emitted by an high energy proton beam at the edge of a magnetic field. *Nucl. Instr. and Meth.*, (164):375–380, 1979.

[40] A. Wolski. Low-emittance storage rings. In *CAS - CERN Accelerator School: Advanced Accelerator Physics Course: Trondheim, Norway, August 18-29, 2013*, pages 245–294, 2014.

[41] A. Hoffman and F. Meot. Optical resolution of beam cross section measurements by means of synchrotron radiation. *Nucl. Instr. and Meth.*, (203):483–493, 1982.

[42] A. Andersson and J. Tagger. Beam profile measurements at MAX. *Nucl. Instr. and Meth.*, (364):4–12, 1995.

[43] S.T. Wang, D.L. Rubin, J. Conway, M. Palmer, D. Hartill, R. Campbell, and R. Holtzapple. Visible-light beam size monitors using synchrotron radiation at CESR. *Nucl. Instrum. Meth.*, A703:80, 05 2013. URL https://arxiv.org/abs/1405.7402.

[44] M. Born and E. Wolf. *Principles of Optics*. Pergamon, New York, 1985.

[45] Optikops Corp. How to measure MTF and other Properties of lenses. http://www.optikos.com/wp-content/uploads/2013/11/How-to-Measure-MTF.pdf, July 1990.

[46] G.K. Green. Spectra and optics of synchrotron radiation. *BNL 50522*, 1976.

[47] USArmy. *MIL-STD-150A, section 5.11.7, Resolving Pover Target*.

[48] Newport. *Intelligent Picomotor Control Modules - User's Guide*, 2003.

[49] Sony. Sensors imx249llj/imx249lqj. http://www.sony.net/Products/SC-HP/sensor/img/product/cmos/.

[50] *Color Camera Sensor Review*. Point Grey, 2016.

[51] *BFLY-PGE-Technical-Reference*. Point Grey, version 13.1 edition, February 2016.

[52] Yu. A. Rogovsky and others. Beam measurement with visible sychrotron light on VEPP-2000 collider. In *Proceedings of RuPAC, Protvino, Russia*, 2010.

[53] H. E. Rusty. *Java Network Programming*. O'Reilly Media, 2004.

[54] J. Patrick. The Fermilab accelerator control system. *Proceedings of ICAP, Chamonix, France*, page WEA2IS03, 2006.

[55] CERN. Root, a cern data analysis framework. https://root.cern.ch/.

[56] Mark Levoy. Autofocus: contrast detection. https://graphics.stanford.edu/courses/cs178/applets/autofocusCD.html, February 2012.

[57] C.E Shannon. A mathematical theory of communication. *Bell System Technical Journal*, (27):379–423, 1948.

[58] NIST Engineering Handbook. Autocorrelation. http://www.itl.nist.gov/div898/handbook/eda/section3/eda35c.htm.